

## Part 2

# Tectonic evolution of the Central European Basin System: constraints from numerical modelling

## 2.1 The Central European Basin System (CEBS): main geological structures and its tectonic evolution

The Central European Basin System (CEBS) covers a large area extending from the southern North Sea across Denmark, the Netherlands and northern Germany to Poland, see Figure 17 for its location and main geological features. It is composed of different crustal domains with Precambrian to Variscan consolidation ages. The main structures include the Norwegian-Danish Basin, the North German Basin and the Polish Trough. This set of sedimentary (sub)basins developed in the Baltica and Variscan domains on the continental crust south and southeast of the Sorgenfrei-Teisseyre Tornquist Zone (STZ and TTZ in Figure 17) and north of the Variscan domain at its southern border.

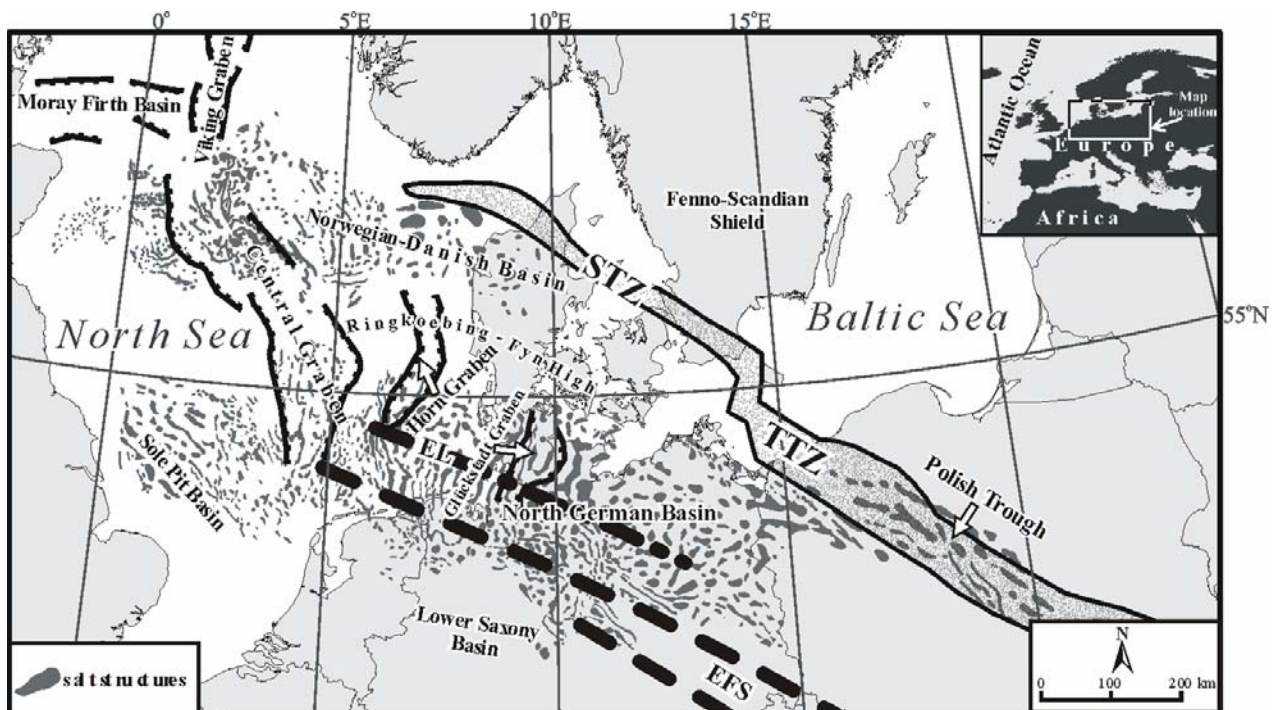


Figure 17. Location of the Central European Basin System and main geological structures, modified after Ziegler (1990), Pharaoh (1999), Bayer et al. (2002), Scheck-Wenderoth et al. (2003), Maystrenko et al. (2006). Abbreviations: **STZ**=Sorgenfrei Tornquist Zone; **TTZ**=Teisseyre Tornquist Zone; **EFS**=Elbe Fault System; **EL**=Elbe Line.

Two major NW-SE-trending fault systems provide an almost triangular shape for the basin system: (1) the Tornquist Zone (STZ and TTZ) in the north and (2) the Elbe Fault System (EFS) along the southern margin.

The Tornquist Zone consists of two branches: (1) the Sorgenfrei Tornquist Zone (STZ) in northern Denmark, and (2) the Teisseyre Tornquist Zone (TTZ) in Poland.

The Sorgenfrei Tornquist Zone is considered as an intracontinental fault domain within Baltica and most probably represents a natural boundary between the stable part of the Baltic (Fenno-Scandian) Shield from its weaker and more mobile southwestern margin (e.g. Berthelsen, 1998; Guterch et al., 1999; Grad et al., 2002; Scheck-Wenderoth & Lamarche, 2005).

The Teisseyre Tornquist Zone may be regarded as a Palaeozoic boundary separating the old Precambrian crust of the Baltic Shield in the northeast from the relative younger crust affected by the Variscan and Caledonian orogenies to the southwest (e.g. Ziegler, 1990; Berthelsen, 1998; Scheck-Wenderoth & Lamarche, 2005).

The Elbe Fault System represents a WNW-ESE-striking zone consisting of several faults arranged in an “*en-echelon*” pattern along the southern margin of the basin system from the southeastern North Sea to southwestern Poland. It runs almost parallel the Teisseyre Tornquist Zone and exhibits a fan-like structure with a narrower area along its southeastern end that widens to the northwest. It is a weak, stress-sensitive (lower) crustal domain where crustal deformation has taken place repeatedly since Late Carboniferous times with changing kinematic activity in response to variation in the stress regime (e.g. Mattern, 1996; Otto, 2003; Scheck-Wenderoth et al., 2002; Scheck-Wenderoth & Lamarche, 2005). The presence of a weak, stress-sensitive lower crust under this domain is supported by structural studies, seismic and gravimetric data as well as results from rheological models.

Additional NW-SE-striking elements are the Ringkøbing Fyn High and the Elbe Line (EL).

The Ringkøbing Fyn High is a structural basement high which consists of faulted blocks separating the Norwegian-Danish Basin from the North German Basin in the southern North Sea across Denmark to the Baltic Sea. It is characterized by the presence of a relative thin sedimentary cover (~1-2 km thick) with respect to the adjacent basins to the north and to the south where the sediments reach between 3 km up to 15 km of thickness. In terms of crustal structure, the Ringkøbing Fyn High has seismic velocities and thicknesses similar to those of the Fenno-Scandian Shield northeast of the Tornquist Zone (e.g. Eugeno-S Working Group, 1998).

The Elbe Line is regarded as the southernmost border of the Baltic crustal domain. It acts as a significant separation between provinces of differing lower crustal P-wave velocities, densities and crustal thicknesses (e.g. Rabbel et al., 1995; Bayer et al., 2002; Scheck-Wenderoth et al., 2002). Deep refraction and wide angle reflection seismic experiments have constrained a remarkable feature in the lower crust north and south of the Elbe Line (e.g. Eugeno-S Working Group, 1998; BABEL Working Group, 1993; MONA LISA Working Group, 1997; DEKORP-BASIN Research Group, 1997; Guterch et al., 1999). More precisely, north of the Elbe Line, the lower crust is characterized by high P-wave seismic velocities (6.8-7.0  $\text{kms}^{-1}$  at depths of about 29 km). In addition, the seismic lines indicate that a wedge of the East European Craton or Baltica continues to the south below the so called Southern Permian Basin which may resemble a passive continental margin. The observed pattern may indicate an extension of a lower crustal basement of Baltica affinity to the southwest as far as the Elbe Line running under northern Germany, Poland and southern Denmark (e.g. Thybo, 1990; Pharaoh, 1999; Guterch et al., 1999; Bayer et al., 2002). Contrastingly, a comparison of the above described deep seismic data south the Elbe Line, across the Elbe Fault System domain, has revealed that the Elbe Fault System is underlined by a lower crust which presents lower than normal P-wave seismic velocities with respect to the surrounding areas. South the Elbe Line, middle-to-lower crustal P-wave velocities range between 6.2  $\text{kms}^{-1}$  in the southern North Sea up to 6.6  $\text{kms}^{-1}$  in southern Poland. Additionally, 3-D gravity modelling studies (e.g. Scheck-Wenderoth et al., 1999; Bayer et al., 1999; Yegorowa et al., 2007) have shown similar changes in the density of the lower crust north and south the Elbe Line. Densities of the crystalline crust below the Elbe Fault System range between 2700-2800  $\text{kg m}^3$ , whereas they increase to 2900-3100  $\text{kg m}^3$  north of the Elbe Line.

The complex internal structure of the CEBS develops through number of deformation phases which postdate the Variscan orogeny and involve Permo-Carboniferous, Mesozoic and Cenozoic rifting and wrench faulting (e.g. Ziegler, 1990). Table 2.1 provides a chart correlating the main tectonics events that characterized the basin system since its formation.

In a global plate tectonic framework, the evolution of the basin system has been governed by the disintegration of the mega-continent Pangaea during the Permian and by the Africa-Eurasia Alpine collision during the late Mesozoic and Early Cenozoic (e.g. Ziegler, 1990; Scheck-Wenderoth et al., in press). Although the CEBS originated on a set of different crustal domains, the (sub)basins show similarities in both the early subsidence stages and further evolutionary phases (e.g. Ziegler, 1990; Van Wees et al., 2000; Scheck-Wenderoth & Lamarche, 2005).

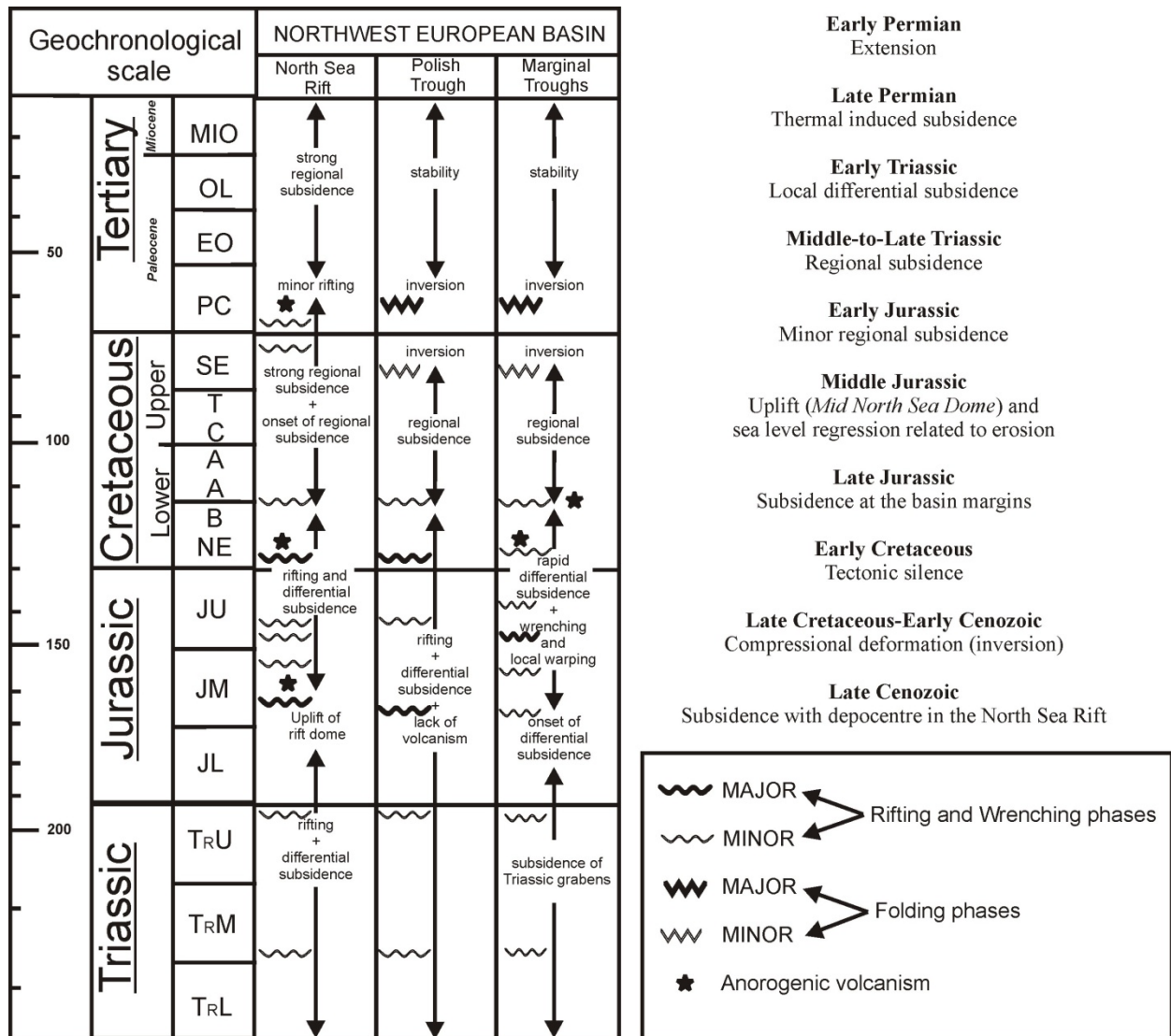


Table 2.1. Correlation chart (left side) and summary (right side) of the main tectonic events in the CEBS.

Basin formation in Latest Carboniferous-Early Permian was accompanied by intense magmatism and thermal destabilization of the lithosphere. This stage was characterized by crustal stretching and strike-slip fault movements along the confining domains of the system, i.e. the Sorgenfrei Tornquist Zone in the north and the Elbe Fault System in the south (e.g. Thybo, 1997; Van Wees et al., 2000). During the Permian the entire area developed as a broad continental depression which was repeatedly flooded during the Zechstein (e.g. Ziegler, 1990) leading to a thick sequence of mobile Zechstein salt (up to 8 km in the deepest areas). Permian thermal relaxation coincided with a phase of relatively slow thermal subsidence throughout the Triassic. A change in the regional stress regime superimposed on a phase of declining thermal subsidence resulted in rifting during late Triassic and Early-to-Middle Jurassic (e.g. Brink et al., 1992). The differential response of the Permian (sub)basins to the new stress regime led to the development of new smaller depocentres as represented by the N-

S-oriented Central Graben, Horn Graben and Glückstadt Graben. During Late Jurassic NW-SE-oriented basins developed along the southern margin of the CEBS. These newly formed structures comprise: the Sole Pit Basin, the Broad Fourteens Basin, the West Netherlands Basin, the Lower Saxony Basin, and the Subhercynian Basin. In latest Cretaceous the basin system was partially inverted in response to far-field compressive stresses structurally related to the Alpine orogenic cycle(s). Inversion was specially localized under the Elbe Fault System, the Sorgenfrei Tornquist Zone, and the Polish Trough. These tectonic phases induced the inception and development of a complex system of sedimentary basin and intervening highs. Further changes in the regional stress regime (e.g. Roth & Fleckenstein, 2001; Reinecker et al., 2005) caused further subsidence during the Cenozoic with N-S-oriented depositional centres in the North Sea and offshore the Netherlands.

The Central European Basin System provides an exceptional example for a complex sedimentary basin and the application of modelling techniques, as almost all currently available basins models have been applied in the past (cf. Part 1). It can be regarded as a complex basin system in terms of (1) having suffered stretching and inversion phases, (2) being located above a highly heterogeneous crust and even mantle derived from the accretion of different terrains during the Palaeozoic, and (3) having a complex upper crust due to repeated activations of salt tectonics. Geophysical data have demonstrated a high level of structuration between the different regional units at deeper crustal and mantle level. Accordingly, the observed differential deformation patterns may be attributed to interactions between regional and/or local variations in lithosphere rheology beneath the different sub-areas and minor changes at the stress boundaries. In the last years, several studies were performed concerning classical basin modelling and simple back-stripping methods including salt redistribution, as discussed in Part 1. However, almost all of these models focused only on the subsidence pattern without regarding the horizontal active stress and strain system. So far, stress and strain models only considered the recent state of the basin system or alternatively focused at relative small domains preventing a unifying description of the basin. In this context, I develop a two dimensional dynamical modelling technique to elucidate the role of the major structural units within the basin system on its evolution through time and their interaction with the regional stress field. The modelling approach is restricted to the well tested thin-sheet model here implemented in the frame of spherical coordinates in order to include regional deformations patterns. The available information concerning the internal structure of the crust and the lithosphere as given by geological/geophysical data are integrated by the construction of a proper three dimensional structural model for the entire

basin system. The structural model integrates the known and observed vertical and lateral heterogeneities which affect the lithosphere of the CEBS. In order to discriminate between the effects provided by the boundary conditions changing slightly within the considered time interval and the thermal and rheological effects inherent to the lithosphere under the basin system, I generate additional and independent three dimensional finite element thermal and rheological numerical codes as described further on in the present chapter. All the codes have been carefully tested and validated before running numerical simulation about the stress and strain system of the basin.

The study aims to supply insights on the contributions of different lithospheric structures together with their temporally and spatially varying rheologies on the stress and strain system. The adopted approach allows considerations about the state of stress within the lithosphere thus providing information about the stress-to-strain relation by means of possible heterogeneities in the internal structure of the lithosphere as well as different loading boundary forces.

In Part 2.2 the results from numerical models concerning the recent, i.e. present day, tectonic setting of the basin system are presented and discussed. The goal is to investigate and quantify the relevance of inherited large-scale lithospheric structures with regard to the recent kinematics and dynamics of the study area.

In Part 2.3 an attempt is presented to develop a reconstruction of the post-Permian evolution of the CEBS. The working philosophy at this stage is to model the first order features as observed during the evolution of the different (sub)basins comprising inversion through time in relation to local variations in the internal structure of the lithosphere and regional variation in the tectonic setting which governed the tectonic evolution of whole Europe during this time span as constrained by the available plate tectonic reconstructions. Accordingly, the modelling results are discussed giving special emphasis on the coupled role played by temporally changing effective (stress) boundary conditions and the internal structure of the lithosphere in controlling and/or even determining the evolution of the geological system.

## **2.2 Stress and strain modelling of present day tectonics in the CEBS**

### **2.2.1 Set up of the integral model: relevant equations and boundary conditions**

The recent deformation and the stress field within the CEBS are estimated by a suitable, spherical, thin-sheet finite-element approach (England & McKenzie, 1982; 1983; Marotta et

al., 2004). Common to all continuity models applied to continental deformation are some assumptions concerning the deformation process. Within the framework of the thin-sheet approach these assumptions may be summarized in the following three points:

1. The lithosphere is regarded as a stratified incompressible viscous fluid of varying thickness and composition flowing over an inviscid asthenosphere. This is a widely adopted assumption in modelling long time-scale geological processes. At the same time, it is a reasonable approximation since the asthenosphere is much weaker than the lithosphere itself. Under this assumption the basal shear stresses at the base of the lithosphere can be neglected, i.e. the base of the lithosphere is considered as a stress free surface.
2. The lithospheric thickness is considered small in relation to the lateral extent of the applied loads.
3. Local isostatic compensation of the lithospheric plate is assumed.

From assumptions (1) and (2) it follows that the vertical gradients of the viscous deviatoric stress ( $\tau_{ij}$ ) and vertical variations of horizontal velocity components can be neglected:

$$(2.1) \quad \frac{\partial \tau_{ij}}{\partial z} \approx 0$$

$$\dot{\epsilon}_{xz} = \dot{\epsilon}_{zx} \approx 0 \approx \dot{\epsilon}_{yz} = \dot{\epsilon}_{zy}$$

In (2.1) (x,y) are the horizontal Cartesian coordinates, z is the vertical pointing downwards,  $\tau_{ij}$  are elements of the deviatoric stress tensor and  $\dot{\epsilon}_{ij}$  are elements of the strain rate tensor which are related to the velocity components ( $u_i$ ) by:

$$(2.2) \quad \dot{\epsilon}_{ij} = \frac{1}{2} \left( \frac{\partial u_i}{\partial x_j} + \frac{\partial u_j}{\partial x_i} \right).$$

The governing equation for describing flow of rocks at geological time scales are the Navier-Stokes equations for a viscous incompressible fluid. After neglecting the inertial term, these equations take the form:

$$(2.3) \quad \frac{\partial \sigma_{ij}}{\partial x_j} = \rho g \bar{a}$$

$$\bar{a} = (0,0,1)$$

The stress tensor  $\sigma_{ij}$  can be written in terms of hydrostatic pressure ( $p$ ) and deviatoric shear stresses ( $\tau_{ij}$ ) as:

$$(2.4) \quad \sigma_{ij} = \tau_{ij} + \frac{1}{3} \delta_{ij} \sigma_{kk} = \tau_{ij} - \delta_{ij} p.$$

In (2.4)  $\delta_{ij}$  is the Kronecker delta function, i.e.  $\begin{cases} \delta_{ij} = 1; & i = j \\ \delta_{ij} = 0; & i \neq j \end{cases}$ , and summation over repeated indexes is assumed.

Inserting (2.4) in (2.3) yields:

$$(2.5) \quad \frac{\partial p}{\partial x_i} = \frac{\partial \tau_{ij}}{\partial x_j} - \rho g a_i.$$

Equation (2.5) is formulated in Cartesian coordinates.

Though some geodynamical problems can be successfully described within the restrictions given by a flat Earth, there exist several other geological/geodynamical problems that cannot be studied making this approximation. It is not only the case of fully three dimensional problems where the vertical (radial) direction enters effectively in the theoretical formulation, i.e. long and deep penetrating subduction zones of transform oceanic faults. As a matter of fact the Earth has a nearly spherical, i.e. geoid, shape. Consequently, many aspects of the geometry and the mechanics on a sphere or a ‘quasi-sphere’ are different from the linear Cartesian equivalent. As shown in Figure 18, the maximum deviation of a curved (spherical) surface from a flat surface,  $\Delta$ , depends on geometrical relationships like: (1) the radius ( $R$ ) given by the average between the equatorial and the polar Earth’s radii, and (2) the wavelength ( $\lambda$ ) of the geological feature under investigation:

$$(2.6) \quad \Delta = R - \sqrt{R^2 - \frac{\lambda^2}{4}}.$$

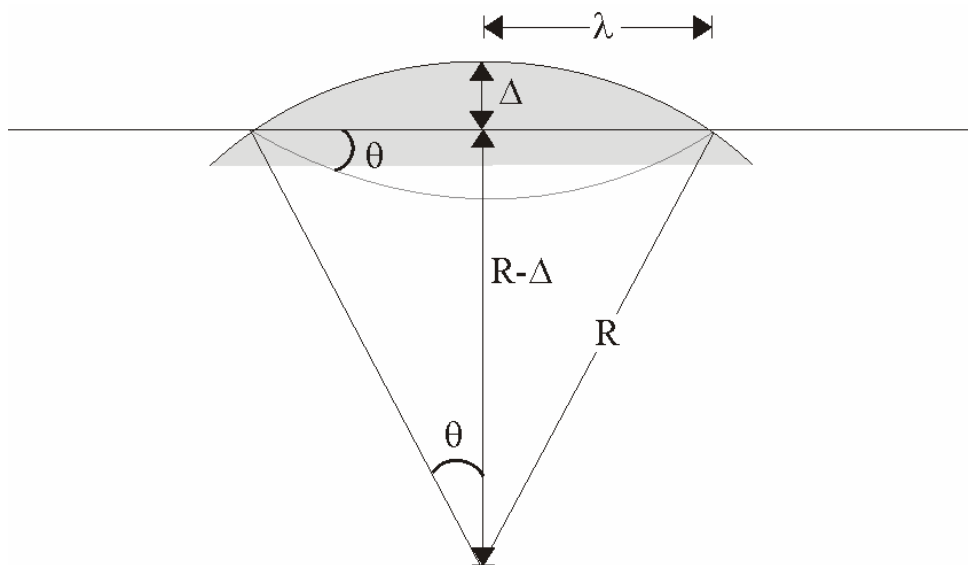


Figure 18. Difference ( $\Delta$ ) between a flat and a curvilinear surface.

From (2.6) it is clear that for geodynamical problems having a length scale of thousands of kilometres, the curvature of the Earth surface plays a relevant role. Since the areal extension of the study domain is of the order of 3000km×1200km, the classical formulation of the thin-sheet approach (e.g. England & McKenzie, 1983) is here implemented in the framework of a spherical system following the work of Marotta et al. (2004) with some modifications in order to include in a realistic way the observed vertical and lateral variations in the lithospheric structure under the basin system.

Spherical coordinates are a system of curvilinear coordinates that are natural for describing positions on a sphere. Define  $\varphi$  to be the azimuthal angle in the (x,y)-plane from the x-axis with  $0 \leq \varphi \leq 2\pi$  (east longitude),  $\vartheta$  to be the polar angle from the z-axis with  $0 \leq \vartheta \leq \pi$  (colatitude equal to  $\vartheta = 90^\circ - \varphi$ ), and r to be the distance (radius) from a point to the origin of the reference system (Earth's centre), see Figure 19.

The spherical coordinates  $(r, \vartheta, \varphi)$  are related to the Cartesian coordinates  $(x, y, z)$  by:

$$(2.7) \quad \begin{aligned} r &= \sqrt{x^2 + y^2 + z^2} \\ \varphi &= \tan^{-1}\left(\frac{y}{x}\right) \\ \vartheta &= \cos^{-1}\left(\frac{z}{r}\right) \end{aligned}$$

Or in terms of Cartesian coordinates:

$$(2.8) \quad \begin{aligned} x &= r \cos \varphi \sin \vartheta \\ y &= r \sin \varphi \sin \vartheta \\ z &= r \cos \vartheta \end{aligned}$$

In both (2.7) and (2.8)  $r \in [0, \infty]$ ,  $\varphi \in [0, 2\pi]$ , and  $\vartheta \in [0, \pi]$  and the inverse tangent ( $\tan^{-1}$ ) must be suitable defined to take the correct two dimensional quadrant of (x, y) into account.

From the above relations, the equations of conservation of mass and momentum (2.5) become:

$$(2.9a) \quad (\hat{r}) \Rightarrow \frac{1}{r} \frac{\partial \sigma_{r\vartheta}}{\partial \vartheta} + \frac{1}{r \sin \vartheta} \frac{\partial \sigma_{r\varphi}}{\partial \varphi} + \frac{\partial \sigma_{rr}}{\partial r} + \frac{1}{r} (2\sigma_{rr} - \sigma_{\vartheta\vartheta} - \sigma_{\varphi\varphi} + \sigma_{r\vartheta} \cot \vartheta) + f_r = 0.$$

$$(2.9b) \quad (\hat{\vartheta}) \Rightarrow \frac{1}{r} \frac{\partial \sigma_{\vartheta\vartheta}}{\partial \vartheta} + \frac{1}{r \sin \vartheta} \frac{\partial \sigma_{\vartheta\varphi}}{\partial \varphi} + \frac{\partial \sigma_{r\vartheta}}{\partial r} + \frac{1}{r} [(\sigma_{\vartheta\vartheta} - \sigma_{\varphi\varphi}) \cot \vartheta + 3\sigma_{r\vartheta}] = 0.$$

$$(2.9c) \quad (\hat{\varphi}) \Rightarrow \frac{1}{r} \frac{\partial \sigma_{\vartheta\varphi}}{\partial \vartheta} + \frac{1}{r \sin \vartheta} \frac{\partial \sigma_{\varphi\varphi}}{\partial \varphi} + \frac{\partial \sigma_{r\varphi}}{\partial r} + \frac{1}{r} (3\sigma_{r\varphi} + 2\sigma_{\vartheta\varphi} \cot \vartheta) = 0.$$

In (2.9a) the term  $f_r = -\rho g$  denotes the gravitational body force, and  $(\hat{r}, \hat{\vartheta}, \hat{\varphi})$  are the unity directional vectors in spherical coordinates.

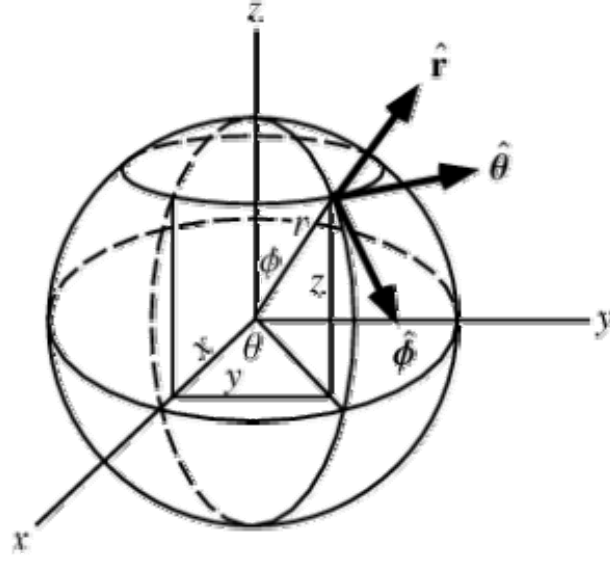


Figure 19. Spherical coordinates and their geometrical relation with the Cartesian coordinates.

Introducing (2.5) in the three equations above (2.9a,b,c) yields:

$$(2.10a) \quad -\frac{\partial p}{\partial r} + \frac{1}{r} \frac{\partial \tau_{r\vartheta}}{\partial \vartheta} + \frac{1}{r \sin \vartheta} \frac{\partial \tau_{r\varphi}}{\partial \varphi} + \frac{\partial \tau_{rr}}{\partial r} + \frac{1}{r} (2\tau_{rr} - \tau_{\vartheta\vartheta} - \tau_{\varphi\varphi} + \tau_{r\vartheta} \cot \vartheta) + f_r = 0.$$

$$(2.10b) \quad -\frac{\partial p}{\partial \vartheta} + \frac{\partial \tau_{\vartheta\vartheta}}{\partial \vartheta} + \frac{1}{\sin \vartheta} \frac{\partial \tau_{\vartheta\varphi}}{\partial \varphi} + r \frac{\partial \tau_{r\vartheta}}{\partial r} + (\tau_{\vartheta\vartheta} - \tau_{\varphi\varphi}) \cot \vartheta + 3\tau_{r\vartheta} = 0.$$

$$(2.10c) \quad -\frac{1}{\sin \vartheta} \frac{\partial p}{\partial \varphi} + \frac{\partial \tau_{\vartheta\varphi}}{\partial \vartheta} + \frac{1}{\sin \vartheta} \frac{\partial \tau_{\varphi\varphi}}{\partial \varphi} + r \frac{\partial \tau_{r\varphi}}{\partial r} + 3\tau_{r\varphi} + 2\tau_{\vartheta\varphi} \cot \vartheta = 0.$$

The independence of depth of the horizontal components of velocity (2.1), gives:

$$(2.11) \quad \dot{\epsilon}_{r\vartheta} \equiv \dot{\epsilon}_{\vartheta r} \approx 0 \approx \dot{\epsilon}_{r\varphi} \equiv \dot{\epsilon}_{\varphi r}.$$

The incompressibility of the fluid requires:

$$(2.12) \quad \dot{\epsilon}_{rr} = -(\dot{\epsilon}_{\vartheta\vartheta} + \dot{\epsilon}_{\varphi\varphi}).$$

From (2.11) and (2.12) it follows that the rate at which the lithosphere deforms in response to a given stress is governed by the rheology of the strongest portion(s) of the plate. Consequently, it is possible to describe continental deformation within a formulation which depends on vertically averaged rheologies of the continental lithosphere. The corresponding equations of (2.10b,c), vertically averaged over the entire lithospheric thickness  $L$ , take the form:

$$(2.13a) \quad -\frac{\partial \bar{p}}{\partial \vartheta} + \frac{\partial \bar{\tau}_{\vartheta\vartheta}}{\partial \vartheta} + \frac{1}{\sin \vartheta} \frac{\partial \bar{\tau}_{\vartheta\varphi}}{\partial \varphi} + (\bar{\tau}_{\vartheta\vartheta} - \bar{\tau}_{\varphi\varphi}) \cot \vartheta = 0.$$

$$(2.13b) \quad -\frac{1}{\sin \vartheta} \frac{\partial \bar{p}}{\partial \varphi} + \frac{\partial \bar{\tau}_{\vartheta\varphi}}{\partial \vartheta} + \frac{1}{\sin \vartheta} \frac{\partial \bar{\tau}_{\varphi\varphi}}{\partial \varphi} + 2\bar{\tau}_{\vartheta\varphi} \cot \vartheta = 0.$$

In both (2.13a,b) all quantities are radially integrated over the entire lithospheric thickness  $L$ .

The radial component of the momentum equation, (2.10a) becomes:

$$(2.14) \quad \frac{\partial \sigma_{rr}}{\partial r} = -f_r = \rho g .$$

Integration of (2.14) over the entire lithospheric thickness (L) yields:

$$(2.15) \quad \sigma_{rr} = g \int_{r_0}^r \rho(r) dr + f(\vartheta, \varphi)$$

In (2.15)  $r_0 = 0$  defines the base surface of the lithosphere, while  $f(\vartheta, \varphi)$  represents an integration constant to be determined. Assuming isostatic compensation for the crust (assumption 3), the radial stress component has no horizontal gradients below the depth of compensation. This condition provides for the integration constant,  $f(\vartheta, \varphi)$ :

$$(2.16) \quad f(\vartheta, \varphi) = -p_0 .$$

In (2.16)  $p_0$  refers to the lithostatic pressure at the base of the lithosphere.

Equation (2.15) now becomes:

$$(2.17) \quad \sigma_{rr} = g \int_0^r \rho(r) dr - p_0 .$$

Following (2.4), equation (2.17) can be rewritten in terms of pressure as:

$$(2.18) \quad p(r) = \tau_{rr} - g \int_0^r \rho(r) dr + p_0 .$$

The average pressure of (2.13a,b) is simply given by the depth integral of (2.18) over the entire lithospheric thickness, L:

$$(2.19) \quad \bar{p} = \frac{1}{L+h} \int_0^{L+h} p(r) dr = \bar{\tau}_{rr} + p_0 - \frac{g}{L+h} \int_0^{L+h} \left( \int_0^{r'} \rho(r') dr' \right) dr .$$

In (2.19)  $h = h_c \left( 1 - \frac{\rho_c}{\rho_m} \right)$  represents the topographic altitude, L the lithospheric thickness,  $h_c$  the thickness of the crust, and  $\rho_c$  and  $\rho_m$  the density of the crust and mantle respectively.

After some algebra, integration of (2.19) yields:

$$(2.20) \quad \bar{p} = \bar{\tau}_{rr} + \frac{g \rho_c s^2}{2L} \left( 1 - \frac{\rho_c}{\rho_m} \right) + \frac{g \rho_m L}{2} .$$

In spherical coordinates the deviatoric components of the stress tensor are related to the velocity components ( $u_\vartheta, u_\varphi, u_r$ ) by:

$$\begin{aligned}
\tau_{\vartheta\vartheta} &= \frac{2\eta}{r} \left( \frac{\partial u_{\vartheta}}{\partial \vartheta} + u_r \right) \\
\tau_{\varphi\varphi} &= \frac{2\eta}{r} \left( \frac{1}{\sin \vartheta} \frac{\partial u_{\varphi}}{\partial \varphi} + u_{\vartheta} \cot \vartheta \right) + u_r \\
\tau_{rr} &= 2\eta \frac{\partial u_r}{\partial r} \\
(2.21) \quad \tau_{\vartheta\varphi} &\equiv \tau_{\varphi\vartheta} = \frac{\eta}{r} \left( \frac{1}{\sin \vartheta} \frac{\partial u_{\vartheta}}{\partial \varphi} + \frac{\partial u_{\varphi}}{\partial \vartheta} - u_{\varphi} \cot \vartheta \right) \\
\tau_{r\vartheta} &\equiv \tau_{\vartheta r} = \frac{\eta}{r} \left( r \frac{\partial u_{\vartheta}}{\partial r} + \frac{\partial u_r}{\partial \vartheta} - u_{\vartheta} \right) \\
\tau_{r\varphi} &\equiv \tau_{\varphi r} = \frac{\eta}{r} \left( r \frac{\partial u_{\varphi}}{\partial r} + \frac{1}{\sin \theta} \frac{\partial u_r}{\partial \varphi} - u_{\varphi} \right)
\end{aligned}$$

In (2.21)  $\eta$  denotes the viscosity.

Using (2.21) and (2.20) in (2.13a,b), yields the result:

$$(2.22a) \quad \frac{\partial}{\partial \vartheta} \left[ 2\bar{\eta} \left( \frac{\partial u_{\vartheta}}{\partial \vartheta} + u_r \right) \right] + \frac{1}{\sin \vartheta} \frac{\partial}{\partial \varphi} \left[ \bar{\eta} \left( \frac{1}{\sin \vartheta} \frac{\partial u_{\vartheta}}{\partial \varphi} + \frac{\partial u_{\varphi}}{\partial \vartheta} - u_{\varphi} \cot \vartheta \right) \right] + \left[ 2\bar{\eta} \left( \frac{\partial u_{\vartheta}}{\partial \vartheta} - \frac{1}{\sin \vartheta} \frac{\partial u_{\varphi}}{\partial \varphi} - u_{\vartheta} \cot \vartheta \right) \right] \cot \vartheta = \frac{g\rho_c R}{2L} \left( 1 - \frac{\rho_c}{\rho_m} \right) \frac{\partial h_c^2}{\partial \vartheta}$$

$$(2.22b) \quad \frac{\partial}{\partial \vartheta} \left[ \bar{\eta} \left( \frac{1}{\sin \vartheta} \frac{\partial u_{\vartheta}}{\partial \varphi} + \frac{\partial u_{\varphi}}{\partial \vartheta} - u_{\varphi} \cot \vartheta \right) \right] + \frac{1}{\sin \vartheta} \frac{\partial}{\partial \varphi} \left[ 2\bar{\eta} \left( \frac{1}{\sin \vartheta} \frac{\partial u_{\varphi}}{\partial \varphi} + u_{\vartheta} \cot \vartheta + u_r \right) \right] + \left[ 2\bar{\eta} \left( \frac{\partial u_{\varphi}}{\partial \vartheta} + \frac{1}{\sin \vartheta} \frac{\partial u_{\vartheta}}{\partial \varphi} - u_{\varphi} \cot \vartheta \right) \right] \cot \vartheta = \frac{g\rho_c R}{2L} \left( 1 - \frac{\rho_c}{\rho_m} \right) \frac{\partial h_c^2}{\partial \varphi}$$

In (2.2a,b)  $\bar{\eta}$  is the vertically averaged viscosity along the entire lithospheric thickness ( $L$ ),  $h_c$  is the crustal thickness,  $L$  is the thickness of the lithosphere,  $\rho_c$  is the density of the crust,  $\rho_m$  is the density of the mantle,  $g$  is the gravity acceleration,  $R$  is the radius of the Earth and  $(u_r, u_{\vartheta}, u_{\varphi})$  are the three (unknown) components of the deformation velocity field.

In order to reduce the dimensions of the problem and to obtain the numerical solution, the radial component of the velocity field may be rewritten in terms of the horizontal components. Invoking the condition of incompressibility (2.12) and neglecting the radial component of the strain rate (i.e.  $\frac{\partial u_r}{\partial r} \approx 0$ ),  $u_r$  can be rewritten as:

$$(2.23) \quad u_r = -\frac{1}{2} \left( \frac{\partial u_{\vartheta}}{\partial \vartheta} + \frac{1}{\sin \vartheta} \frac{\partial u_{\varphi}}{\partial \varphi} + u_{\vartheta} \cot \vartheta \right).$$

Once the crustal thickness  $h_c$  and the boundary conditions are specified, the numerical integration of equations (2.22a,b) yields the stationary tectonic deformation field.

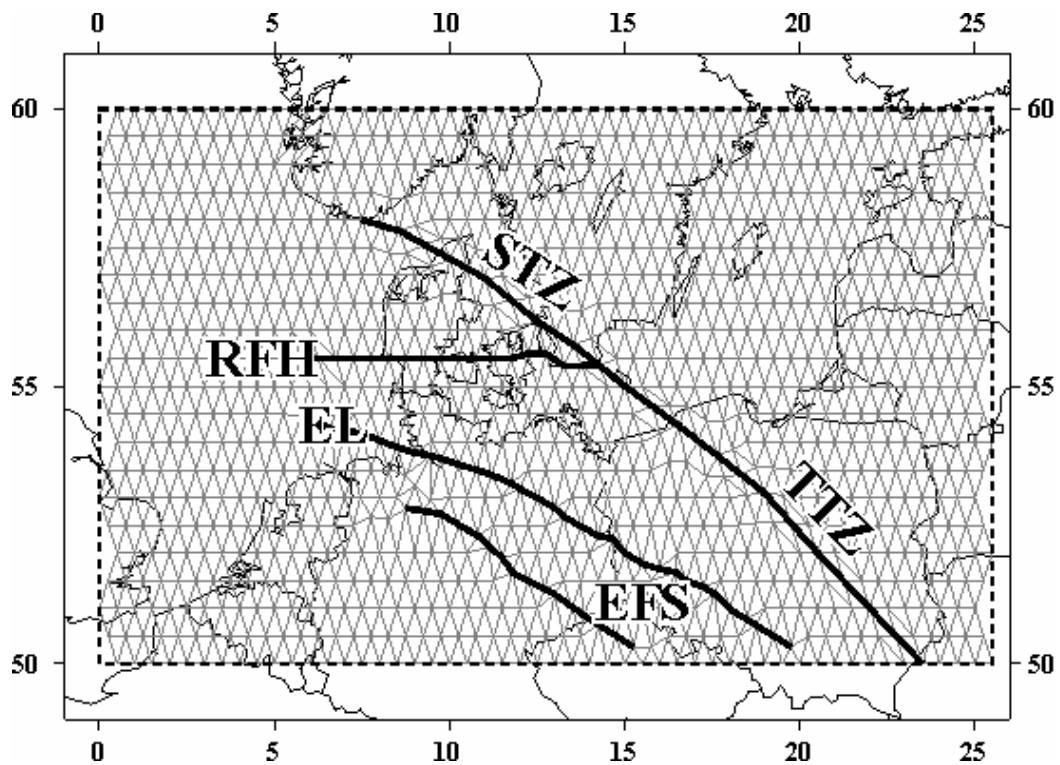


Figure 20. Finite 2-D integral mesh. Thick continuous black lines enlighten those elements whose disposition has been manually adjusted to match the major observed geological structures. Abbreviations: **EFS**=Elbe Fault System; **EL**=Elbe Line; **RFH**=Ringkøbing Fyn High; **STZ**=Sorgenfrei-Tornquist Zone; **TTZ**=Teisseyre-Tornquist Zone.

To perform numerical integration of (2.22a,b) the entire domain of the study area is discretized by the use of a two dimensional mesh made up of 2000 triangular (equilateral) elements with a horizontal grid resolution of a quarter of degree, see Figure 20. The use of triangular finite elements rather than any other boundary shapes is preferred since they warrant the convergence of the numerical solution within the minimum number of nodal connections, i.e. minimum number of degrees of freedom for the numerical problem. The initial symmetrical disposition of the elements inside the grid is adjusted manually to match the position of the major structural lineaments as shown by thick black lines in Figure 20.

Within each element the continuum velocity field is approximated by linear polynomial interpolating functions. With numerical integration used to substitute the exact analytical integration, an additional error is introduced into the calculation. In the framework of the finite element technique, this additional error is related to the shape and dimension ( $h$ ) of the finite element used as well as to the order ( $p$ ) of the numerical integration, i.e. number of points used in the polynomial interpolation within each element. Specifically, if  $h$  represents the ‘size’ of the triangular (equilateral) element and  $p$  is the complete polynomial in the

expansion, the order of error,  $R$ , due to the approximation to the unknown function is  $O(h^{p+1})$ . To minimize this error maintaining reasonable CPU computational times, a *subparametric* element configuration is adopted in the present study, i.e. number of nodes used to define the geometry of the element less than number of nodes used in the numerical integration, see Figure 21,a.

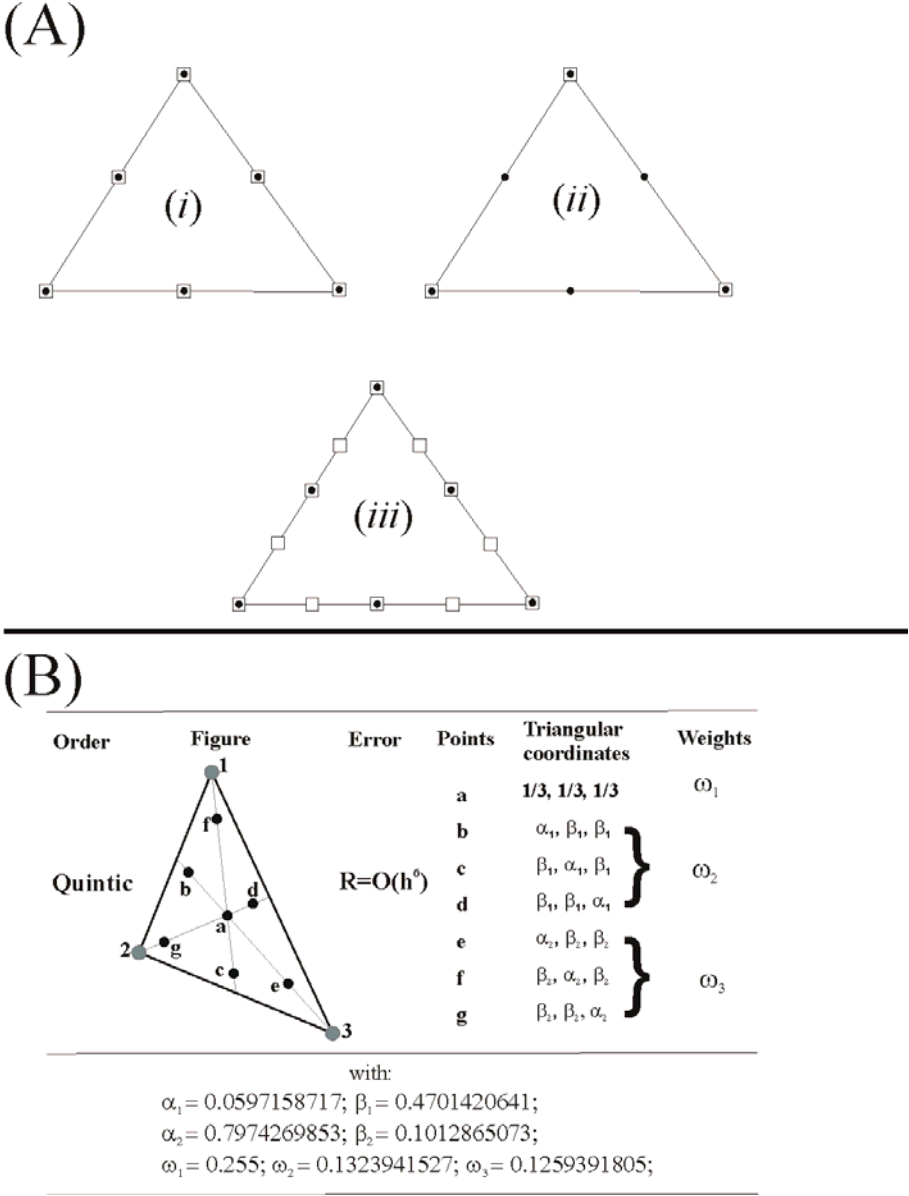


Figure 21. (A) Various finite element specifications. Black dots indicate points at which the geometrical coordinates of the elements are specified, white squares indicate points at which the function integral parameters are specified. (i) Isoparametric, (ii) superparametric, and (iii) subparametric element configuration. (B) Numerical integration formulas for triangular finite elements, after Zenkiewicz (1977). The positions of the (seven) integration points (a, b, c, d, e, f, g) together with their weight coefficients ( $\omega_i, i=1,2,3$ ) for the numerical integration are shown. Grey dots indicate the nodal connections used to describe the geometry of the element.

Seven integration points (=quintic order of integration) are used for each element thus giving an approximation  $R=O(h^6)$  as shown in Figure 21,b. Gauss quadrature within the frame of the Galerkin-residual method is used to numerically solve the differential equations (2.22a,b), since it provides unconditional stability of the solution, e.g. Zenkiewicz (1977).

### **Crustal thickness variations**

To perform the numerical integration of (2.22a,b) and to finally obtain the stationary horizontal deformation field it is necessary to specify the initial crustal thickness,  $h_c$  in equations (2.22a,b). Previous thin sheet approaches frequently adopted constant thickness of the crust. This approach was based on the fact that model outcomes depend more on the rheological parameters adopted for the structural crustal layer in the study rather than on the crustal thickness variations. However, in a multi-layered lithosphere, the depth to the Moho exerts a primary control on the total lithospheric strength. The depth level of the crust-to-mantle boundary is of particular significance for the specification of thermophysical properties which determine the lithospheric thermal structure. Changes, even small, in crustal thickness lead to quite significant temperatures changes at a lithospheric scale. Considering the more recent Moho map of Central and Western Europe published by Ziegler & Dèzes (2005), it is evident that the CEBS is characterized by variable crustal thicknesses ranging from currently believed 25-30 km in its central part down to 48-50 km in the eastern domain of the Baltic Shield and East European Craton. The small wavelength of lateral crustal thickness gradients prevents attempts to find a representative averaged value for the depth of the Moho for the entire basin system. Therefore, a realistic base map for the Moho discontinuity is adopted here.

Figure 22 shows crustal thickness within the Central European Basin System. It is adapted to the size of the study area and to the nodal positions of our integral 2-D mesh from the latest compilation of the European Moho base map published by Ziegler & Dèzes (2005).

There are two main structural domains in terms of crustal configuration: (1) a stable domain under the Fennoscandian-East European Craton in the east characterized by a Precambrian thick crust with Moho depths up to 48-52 km; and (2) a more mobile domain under Phanerozoic Europe where Moho depths range between 24 km to about 36 km. A linear steep depth gradient along the Tornquist Zone separates the deep Moho beneath the Precambrian crust from the shallower Moho to the southwest. Under this domain the Moho is in average 30-32 km deep.

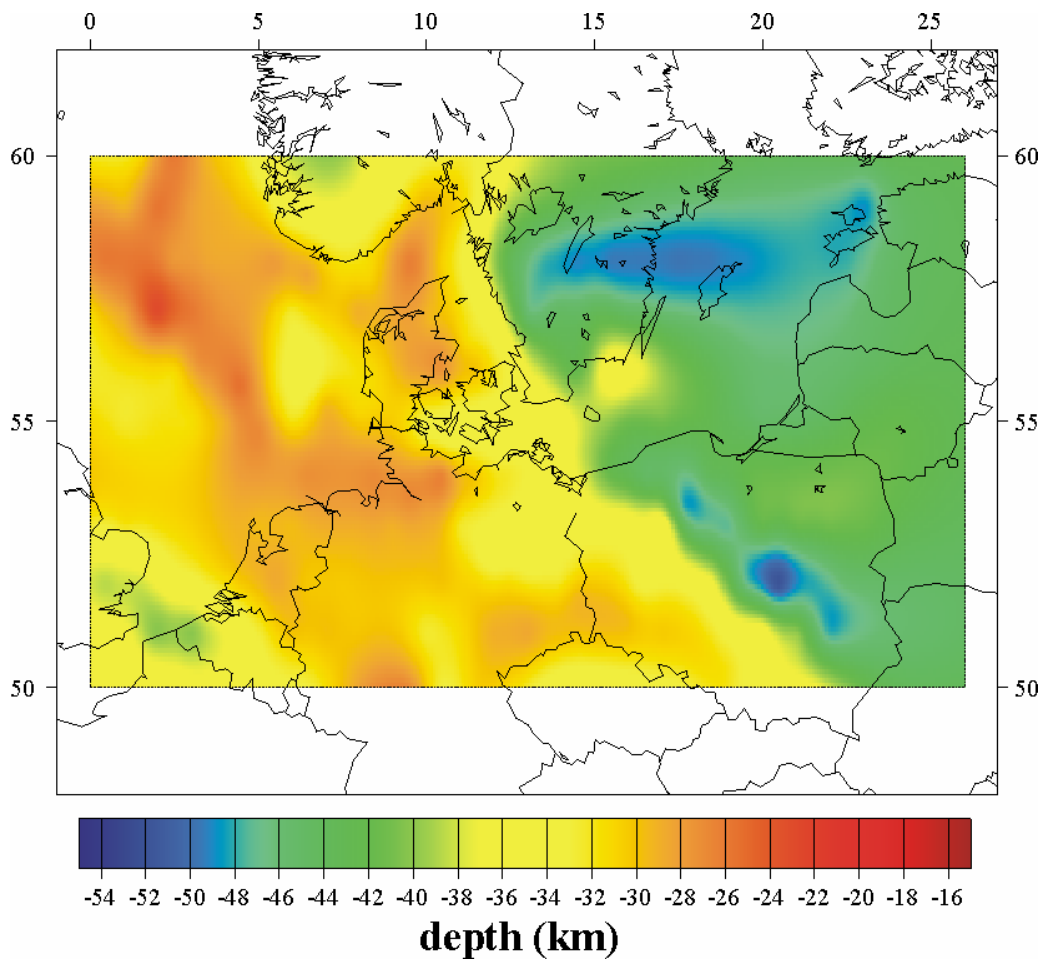


Figure 22. Base map (km) for the Moho discontinuity. Digitized adapting to the study area and to the nodal points of the 2-D dimensional mesh (Figure 20) the European Moho base map published by Ziegler & Dezes (2005).

This almost uniform Moho depth is structured by local lows occurring under the Ringkøbing Fyn High where the crust-to-mantle boundary deepens to 36 km and under the Polish Basin with Moho depths up to 50 km. Some prominent Moho highs are also present. The most striking Moho high is located in the North Sea domain where the Moho is located at about 24 km of depth. Further Moho highs are in northern Denmark as well as in the north-western part of Germany with Moho depths of about 26 km.

Within the study region, there is still some uncertainty concerning the Moho topography. This is related to contrasting features between published Moho maps and results from recent deep seismic refraction and reflection studies as well as gravity data. Specifically, more recent seismic studies concerning the southern segment of the Tornquist Zone below the Polish Basin have revealed the presence of a transition domain located beneath the Teisseyre-Tornquist Zone between a 30-32 km thick two-layered Phanerozoic crust under Western Europe and a 40-42 km thick Precambrian crust below the East European Craton and the

Baltic domain (e.g. Babel Working Group, 1993; Guterch et al., 1999; Grad et al., 1999, 2002; Thybo et al., 1999, 2002).

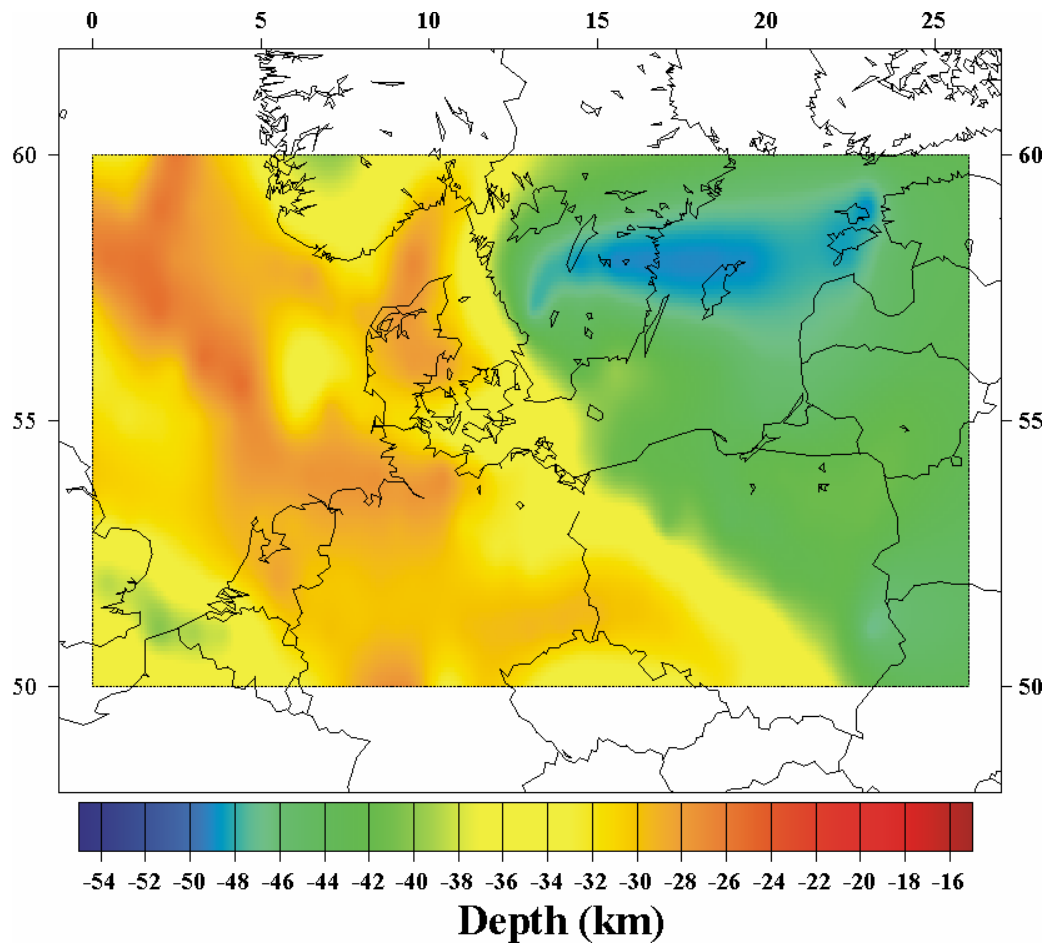


Figure 23. Final base map (km) adopted in the model calculation to represent the crust-to-mantle discontinuity.

Therefore, recent deep seismic refraction studies do not confirm the strong Moho deepening below the Polish part of the Teysserie-Tornquist Zone as shown in Figure 22. In order to diminish the possible effects of these uncertainties, the above described seismic results are incorporated into the Moho map published by Ziegler & Dézes (2005) as shown in Figure 23. The updated Moho map images the Teisseyre-Tornquist Zone as a gradient domain with Moho depths between 38 km and 42 km. An additional local Moho deepening, up to 44 km, is located to the east of the Teisseyre-Tornquist Zone.

### **Boundary conditions**

Results of previous numerical studies, e.g. Marotta et al. (2004), have already demonstrated that amplitudes and directions of predicted horizontal velocities at sites located well away

from natural plate boundaries are more sensitive to the parameters used in the models rather than to slightly variable boundary conditions. In order to better constrain the role of contrasting lithospheric structures and their effect on the present-day deformation and stress regime, all the integral calculations for the recent tectonic state are performed relative to a common and fixed set of *velocity boundary conditions*.

The choice of velocity boundary conditions rather than stress boundary conditions is here adopted since: (1) velocity boundary conditions have been proven to be more appropriated than stress boundary conditions in similar tectonic settings (e.g. India-to-Asia collision), and (2) it is not always possible to determine the basic factor(s), whether it is basal traction (i.e. shear stress), lateral normal stress or a combination of the principal forces driving plate tectonic.

To determine the suitable set of boundary conditions for the recent state for the CEBS, the tectonic scheme presented by Marotta et al. (2004) for the European platform is adopted.

The applied boundary forces are modelled relative to a fixed European plate and comprise, see Figure 24:

1. *Ridge push forces across the North and Middle Atlantic Ridge.* These forces are parameterized in terms of velocity boundary conditions applied along the same ridge. Horizontal velocities simulate the line forces acting along the plate boundary, thick grey arrows of Figure 24. The line force normal to the ridge axis is calculated from the eigenvalues of the stress tensor within the elements used to define the ridge following the procedure described in Richardson et al. (1979). Velocities at the boundaries range between a minimum of about 1 mm/yr to a maximum value of 5 mm/yr. Accordingly, the range of predicted push forces along the westernmost part of the Atlantic Ridge varies from about  $10^{12}$  N/m for an imposed velocity of about 1 mm/yr to a maximum of about  $10^{13}$  N/m for an imposed velocity of 5 mm/yr. The imposed velocities are not considered as constant along the entire ridge but rather are scaled with respect to the spreading velocities deduced from NUVEL-1A (e.g. DeMets et al., 1994). Therefore, imposed velocities of 1 mm/yr and 5 mm/yr are respectively of the order of  $1/20^{\text{th}}$  and  $1/4^{\text{th}}$  of the full spreading rate ( $\sim 2$  cm/yr) according to NUVEL-1A.
2. *Africa-Eurasia collisional forces.* The velocity of the African plate with respect the European plate (thin black arrows along the southwestern border) is constrained by data derived from NUVEL-1A whose patterns resemble a counter-clockwise rotation

of Africa with respect to Europe superimposed on a continental convergence between the two plates of the order of 1 cm/yr.

3. *Subduction forces along the Aegean trench.* Velocity values at six sites are the same as geodetically determined by McClusky et al. (2000). They are applied to an equal number of nodes in their proximity (thin white arrows) and range between 25 mm/yr up to 33 mm/yr. These velocities reflect trench subduction forces along the Aegean microplate boundary and represent the velocity of these geodetic sites with respect to Eurasia.

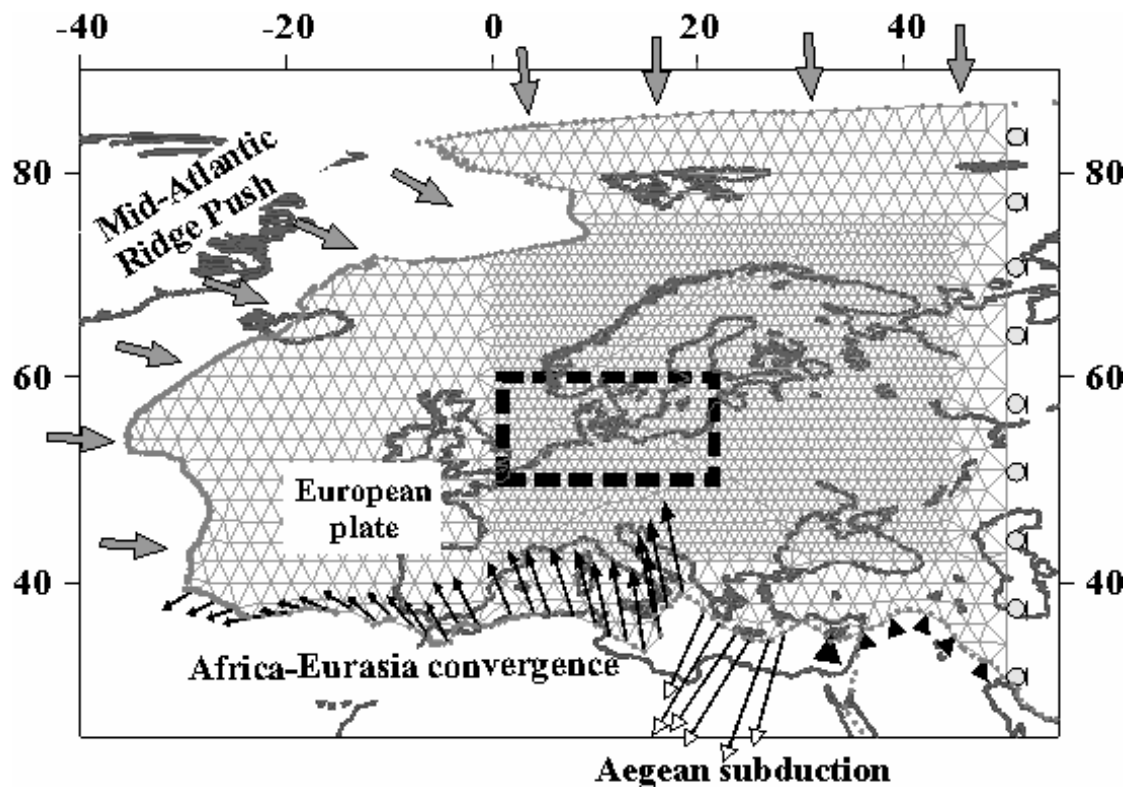


Figure 24. Modelled boundary forces acting along the boundaries of the European plate to derive the horizontal deformation velocities along the borders of the area under investigation, black dashed frame. See text for explanation.

The eastern boundary of the model domain is fixed. To avoid large effects from artificial stress accumulation, a shear stress free boundary condition is imposed at this location (light grey dots along the right boundary). This condition is consistent with a possible decoupling between the western and eastern domains of the Eurasian plate. It is used to focus all the intraplate deformation of the Eurasian plate driven by the modelled tectonic forces within the model domain. The plate contact between the East European Platform and the Arabian region

is held fixed (black triangles). Although NUVEL-1A indicates a north directed velocity at this boundary, previous models (e.g. Jimenez-Munt et al., 2003; Marotta et al., 2004) have demonstrated that the local stiffness of the lithosphere superimposed on the presence of a transcurrent fault at the northern boundary of the Arabian Plate produce little long-wavelength deformation to the north.

The modelled velocity field does not account for any rigid rotation of the European plate with respect to a global-scale reference frame. Indeed, these motions represent velocities (i.e. intraplate horizontal deformation) superimposed on any rigid plate motions.

In choosing the set of velocity boundary conditions, a velocity equal to 1 mm/yr is imposed to simulate the effects related to the Middle Atlantic spreading. This choice is based on the fact that (1) this type of boundary setting has already provided the best fit in the reference model of Marotta et al. (2004), and (2) the present-day deformation pattern of the CEBS is mainly affected by plate convergent-induced compressive stresses (e.g. Zoback, 1992; Reinecker et al., 2005). In order to define the set of velocity boundary conditions the velocity vectors calculated from the large-plate reference model are scaled to match the locations of the boundary nodes framing the 2-D integral mesh of Figure 20.

Apart from suitable boundary conditions and from the specification of the initial crustal thickness, the numerical integration of (2.22a,b) requires to specify another model parameter: the vertically-averaged *effective viscosity* of the lithosphere,  $\bar{\eta}$ . This parameter is given by:

$$(2.24) \quad \bar{\eta} = \frac{1}{2} B \dot{\epsilon}^{\left(\frac{1}{n}-1\right)}$$

$$B = \dot{\epsilon}_0^{-\frac{1}{n}} (\sqrt{2})^{\left(\frac{1}{n}-1\right)} \int e^{\left(\frac{E}{nRT}\right)} dz$$

In (2.24)  $T$  (unit=K) is the temperature,  $R$  is the Boltzman's constant ( $R=8.314510 \text{ JK}^{-1}\text{mol}^{-1}$ ),  $\dot{\epsilon}$  (units= $\text{s}^{-1}$ ) is the effective strain rate given by the second invariant of the symmetric part of the strain rate tensor,  $\dot{\epsilon}_{ij}$  (i.e.  $\dot{\epsilon} \equiv \sqrt{\dot{\epsilon}_{ij}\dot{\epsilon}_{ij}}$ ),  $\dot{\epsilon}_0$  (units= $\text{Pa}^{-n}\text{s}^{-1}$ ), the *activation energy*  $E$  (units= $\text{Jmol}^{-1}$ ) and the *exponential coefficient*  $n$  (adimensional) are creep parameters that depend on the material. Integration of (2.24) is limited to the ductile domain(s) in the lithosphere. The effective viscosity,  $\bar{\eta}$ , is structurally connected to the adopted rheology, the local thermal state, and the effective strain rate adopted in the model.

### 2.2.2 Rheological model

To calculate the distribution of stresses with depth for a given strain rate regime, the lithosphere is approximated by a finite number of lithological units of uniform structural composition. In relation to the thermal state and the local strain rate, for each structural layer the set of possible deformation regimes comprise brittle failure according to Byerlee's law and ductile failure by steady-state power law creep or Dorn's law (for olivine). Each type of deformation mechanism has a different meaning and corresponds to a specific constitutive equation which relates stress to strain.

Among brittle processes, two different modes of brittle deformation may be distinguished: fracturing or friction along (pre)existing fractures. Although some localized diffuse deformation, i.e. pressure solution transfer, may occur at relatively low temperature conditions, in the brittle domain rock failure is commonly described by the *Mohr-Coulomb criterion*. It describes the critical state of stress at which brittle failure will set up within the lithosphere. In the present study, brittle failure is modelled by plastic behaviour, therefore all properties depend on pressure but not on temperature or rock type (Byerlee, 1978; Cloetingh & Burov, 1996). Due to the thin sheet assumption of plain stress, it follows that one of the principal stresses coincides with the vertical stress. This condition is usually referred to as "*Andersonian stress regime*". As already demonstrated by Lynch & Morgan (1987) under this condition the brittle yield strength,  $\sigma_B$ , follows Byerlee's Law and may be simply written as:

$$(2.25) \quad \sigma_B = (\sigma_H - \sigma_V)_B = \beta \cdot z .$$

In (2.25)  $\sigma_H$  and  $\sigma_V$  represent the maximum and the minimum principal stress respectively,  $z$  is the depth while  $\beta$  is the brittle failure coefficient depending on the type of fault, the angle of fracture and the pore pressure. Following the study by Lynch & Morgan (1987) its value amounts  $16 \text{ MPa}\cdot\text{km}^{-1}$  for extensional tectonic settings and  $40 \text{ MPa}\cdot\text{km}^{-1}$  for compressional tectonic settings.

At high temperatures deformation within the lithosphere is dominated by creep mechanisms. Laboratory studies have demonstrated that the ductile yield strength is a power function of the strain rate and depends strongly on temperature and rock type (e.g. Goetze & Evans, 1979; Ranalli, 1995). Before reaching the condition of steady-state creep (constant strain rate under constant stress and temperature conditions), ductile flow is governed by instantaneous elastic deformation and transient creep (decreasing strain rate with time). However, with the exception of few geodynamical processes, e.g. post glacial rebound, the elastic and transient strains are negligible with regard to steady-state strains in tectonic deformation.

Consequently, ductile flow laws for rocks are formulated as the relationship between differential stress  $(\sigma_H - \sigma_V)_D$  and longitudinal effective strain rate  $\dot{\epsilon}$  taking the form of a typical steady-state power law, e.g. Turcotte & Schubert (2002):

$$(2.26) \quad \sigma_D = (\sigma_1 - \sigma_3)_D = \left( \frac{\dot{\epsilon}}{\dot{\epsilon}_0} \right)^{\left( \frac{1}{n} \right)} e^{\left( \frac{E}{nRT} \right)}.$$

All parameters in (2.26) have the same physical meaning as shown in (2.24). Equation (2.26) indicates that critical differential stresses are strongly dependent on temperature, strain rate and material constants, but are completely independent of the confining pressure. Specifically, critical stresses exponentially increase with decreasing temperature.

Laboratory experiments as well as analogue models have demonstrated that above a critical stress ( $\sim >200$  MPa) the power law creep breaks down into the so-called low-temperature plasticity, which is characterized by an almost linear increase of stress with increasing temperature. Low-temperature plasticity parameters are available only for olivine. Following Goetze & Evans (1979) a better description of the behaviour of olivine for applied stresses higher than 200 MPa is given by the relationship:

$$(2.27) \quad \sigma_D = (\sigma_1 - \sigma_3)_D = \sigma_0 \left( 1 - \sqrt{\frac{RT}{Q_D} \ln \left( \frac{\dot{\epsilon}}{A_D} \right)} \right).$$

In (2.27)  $\sigma_0$  (units=Pa),  $Q_D$  (units=Jmol<sup>-1</sup>) and  $A_D$  (units=s<sup>-1</sup>) are flow parameters depending on rock type.

For a given tectonic setting, depth, flow properties, temperature and strain rate, the first order rheological behaviour (brittle or ductile) is determined by the relative magnitude of frictional and creep strength. If the critical strength for frictional sliding is less than the one required for ductile behaviour, failure by frictional sliding will occur. In the opposite case, ductile flow will dominate deformation. The so-called *brittle-to-ductile* transition corresponds with the depth level associated to the equality of frictional and creep strength for a given strain rate value. The depth-dependence of the rheological structure is addressed by the construction of strength envelopes, i.e. rheological profiles, as extrapolated from rock mechanical data and additional constraints like seismicity, gravity and petrology. The concept of strength envelopes for the continental lithosphere was firstly developed by Goetze & Evans (1979) (the so-called ‘*jelly sandwich model*’) and is nowadays well established. Strength envelopes allow to identify brittle and ductile layers and the estimation of lithospheric strength. Essentially, they consist of two different types of curves, see Figure 25. Combining the rheological laws describing the different modes of continental deformation it is possible to

describe a piece-wise continuous contour function, i.e. the strength envelope, given by the minimum value defined by brittle and ductile deformation:

$$(2.28) \quad \Delta\sigma = \pm \min(|\sigma_B| ; |\sigma_D|)$$

Equation (2.28) is positive for extension and negative for compression.

The total strength of a multilayered lithosphere with a depth-varying temperature-dependent rheological structure is obtained by integrating the yield stress envelope over the entire lithospheric thickness (L):

$$(2.29) \quad \sigma_L = \int_0^L \Delta\sigma dz$$

In (2.29)  $\sigma_L$  represents the vertical integrated strength of the lithosphere and L is the thickness of the mechanically strong lithosphere.

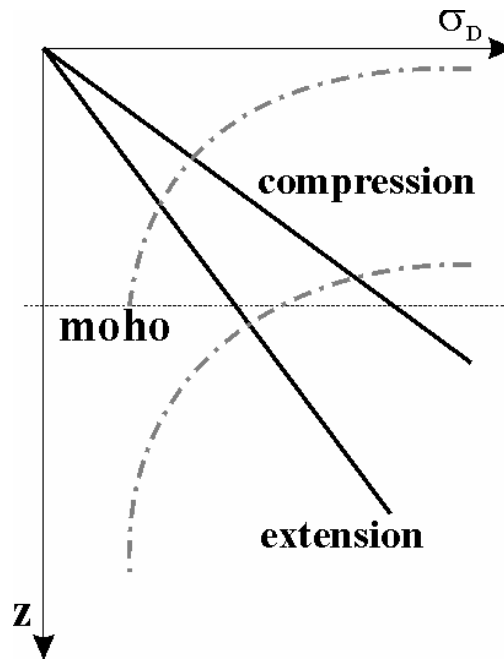


Figure 25. Changes with depths and deformation regime (compression and extension) in the mechanical strength of a typical two layered lithosphere (crust plus mantle). The straight black lines represent brittle failure. Following Byerlee's law they show increasing rock strength with increasing depth as described by (2.3). The dashed and dotted grey lines stand for ductile deformation. The strength described by these curves decreases exponentially with depth due to the fact that the temperature increases almost linearly with depth and viscosity for any given mineral as described by (2.4).

Typical strain rate ( $\dot{\epsilon}$ ) magnitudes, corresponding to the observed deformation rates, range between  $10^{-16} \text{ s}^{-1}$  and  $10^{-14} \text{ s}^{-1}$  for both compressional and extensional tectonic settings (e.g. Molnar & Tapponier, 1981; Van den Beukel, 1990; Cloetingh & Burov, 1996). In general higher strain rates lead to higher strength values at a given depth in relation to lower strain

rates. However the results from the strength model are not strongly affected by changes in strain rate values since strain rates within one order of magnitude provide changes less than 10% in the strength results. Therefore, in the following all calculations are performed imposing an effective strain rate  $\dot{\epsilon} = 10^{-15} s^{-1}$ .

From equation (2.24), a strong dependence follows connecting the effective viscosity and the thermal structure of the lithosphere. To consider the temperature-related effects I generated a 3-D finite-element model to solve for the steady state heat transfer equation as described below.

### 2.2.3 Thermal model

There are three fundamental processes that produce and redistribute heat in the continental lithosphere: heat conduction, heat advection (or convection) and heat production. With the exception of few anomalous areas where magmatic and/or hydrothermal processes play a significant role, heat is transported primarily by conduction in the lithosphere.

In order to solve for the heat diffusion equation including heat production, a steady thermal state is adopted in the present study. Following this assumption, the full 3-D description of the thermal energy balance in the lithosphere takes the form:

$$(2.30) \quad \vec{\nabla} \cdot (k \cdot \nabla T) + H = 0.$$

The parameter  $k$  on the right-side of (2.30) is the thermal conductivity. It is a property of materials that expresses the heat flux ( $q$ ) that will flow through the material if a certain temperature gradient ( $\nabla T$ ) exists. It is not constant, but varies with rock type, temperature and pressure conditions. Changes of thermal conductivity as a function of pressure and temperature are negligible at geologically relevant temperatures in the lithosphere. However, some important variations in thermal conductivity are mainly associated with variations in composition and mineralogy. In general, thermal conductivity varies by a factor 2 or 3 between different rock types. Fortunately, adequate experimental data obtained by both steady-state and non-steady-state experimental techniques, exist to provide guidance on the orders of magnitude and parameter ranges of thermal conductivities for all common rock types.

The last parameter in (2.30),  $H$ , is the volumetric heat production in the lithosphere which may have mechanical, chemical or radioactive contributions. At lithospheric scale, heat production associated with natural radioactive decay is dominating. Therefore, it is generally assumed as the effective source of heat in continental lithosphere,  $H \sim H_{\text{rad}}$ . Both magnitudes

and distributions with depth of radioactive heat production are important controlling factors for the thermal budget of the crust and the lithosphere. Averaged volumetric heat production measurements range between  $0\text{--}0.02 \mu\text{W m}^{-3}$  for mantle rocks,  $0.1\text{--}1 \mu\text{W m}^{-3}$  for lower crustal rocks, and  $1\text{--}4 \mu\text{W m}^{-3}$  for upper crustal rocks.

To numerical solve Eq. (2.30), a finite-element based numerical code has been generated. To perform numerical simulation of the thermal energy equation (2.30), the study domain is discretized through a three dimensional mesh consisting of 32000 finite integral elements. Three dimensional finite elements have the shape of triangular prisms belonging to the ‘*serendipity*’ family, i.e. polynomial functions only dependent on nodal values placed on the element boundary. Figure 26 illustrates the 3-D mesh and the geometrical representation of the finite element used in the numerical integration. Triangular prisms finite elements require fewer degrees of freedom than other element representations (e.g. quadratic elements). Moreover the boundary faces of the three dimensional elements used in the thermal model coincide with the finite elements of the 2-D integral mesh of Figure 20. Accordingly, the temperature can be obtained for each lattice node of the 2-D integral mesh without introducing additional errors due to nodal interpolation.

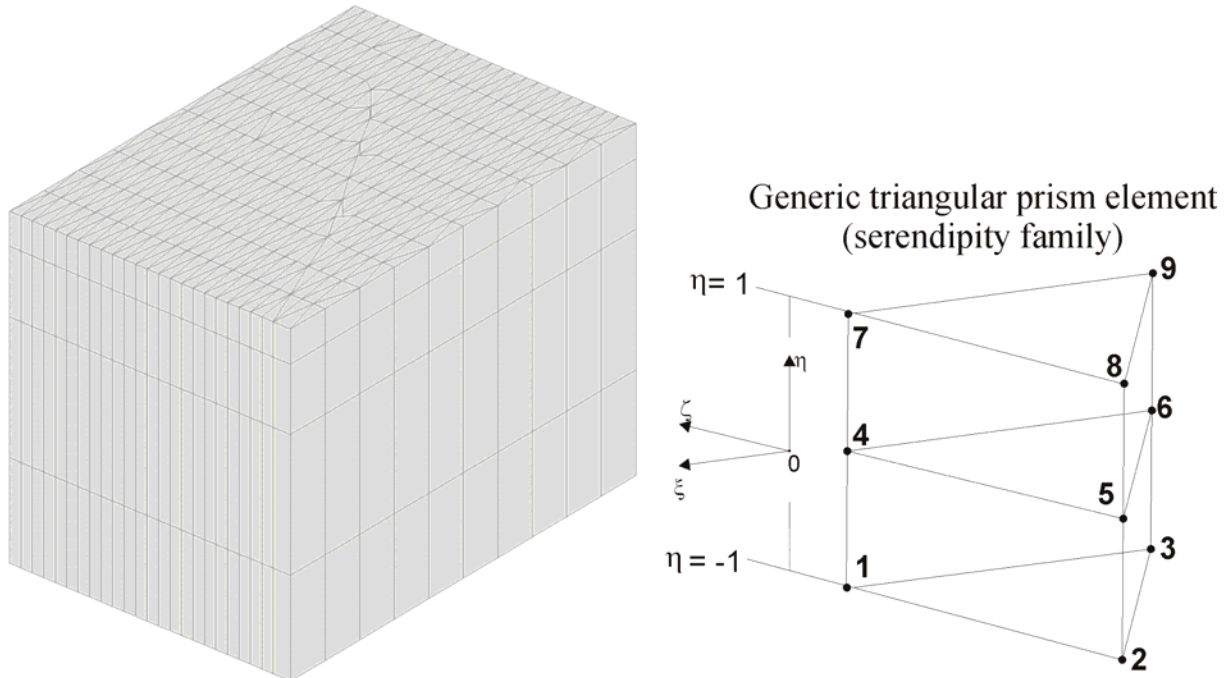


Figure 26. 3-D integral mesh used for the thermal model (left panel) and corresponding finite element in local coordinates  $(\xi, \zeta, \eta)$  (right panel).

Once having defined the proper boundary conditions and having specified the correct thermal parameters, the numerical solution of the steady state heat transfer equation is obtained by the

*Gauss-Galerkin quadrature* method with twenty-six integration points within each finite element (i.e. cubic order of integration).

Equation (2.30) represents a second order differential equation, so that two different boundary conditions are needed to solve for it.

Top boundary condition:

In the present study, the top boundary condition chosen is a constant surface temperature of  $T_{\text{top}}=300$  K.

Generally, near-surface terrestrial heat flow is assumed to reflect the long-term thermal state of continental lithosphere. However, derived near-surface heat flow values are ‘biased’ by the presence of a transient component (e.g. climatic variation and/or erosion and sedimentation) or are highly disturbed by other surface processes (e.g. hydrologic flow, conductivity contrasts, variations of electrical fields gradients) which cannot be fully accounted for. Consequently, in deep thermal geodynamic modelling (i.e. lithospheric scale) a ‘Dirichlet boundary condition’ is usually preferable for the top surface boundary rather than a ‘Neumann boundary condition’.

Bottom boundary condition:

A fixed temperature of  $T_{\text{bottom}}=1600$  K across the asthenosphere-lithosphere transition is chosen as the corresponding bottom boundary condition.

This type of boundary condition allows to describe the variations of temperature throughout the entire lithosphere as well as to investigate the influence of crustal and mantle thickness variations on the lithospheric strength.

The lateral boundaries of the model are assumed no-flow boundaries.

After having obtained the numerical solution of (2.30), strength envelopes are calculated at each node of the 2-dimensional grid of Figure 20 by the use of a specific rheological numerical model to simulate the suitable rheological flow laws described above (Eq. 2.25, Eq. 2.26, Eq. 2.27) adopting as input parameters the obtained geotherms. Integration over the entire lithospheric thickness of the derived strength envelopes yields the corresponding lithospheric strength,  $\sigma_L$  which is then used to determine the effective viscosity (Eq. 2.29) for each nodal point of the integral mesh. Inserting the obtained values of  $\bar{\eta}$  in the corresponding differential equations for the deformation velocity field, the numerical integration of (2.22a,b) gives the horizontal stationary deformation field.

#### 2.2.4. Model results

To test the relative influence of variations of compositional and thermal parameters on the setting of the regional deformation pattern in the CEBS a step-wise trial-and-error approach is followed. The consistency of the model results is constrained by direct comparison between model predictions and two different types of observable data sets.

##### **Horizontal deformation velocity field and strain rates**

The first reference data set is given by the present-day horizontal deformation velocity field and strain rates as geodetically observed in Central and Western Europe, see Figure 27. This data set is based on the last ten years of GPS observations which were used to define the ITRF2000 velocity solution database (Altamini et al., 2002). The ITRF2000 velocity database is chosen since it provides the most extensive and accurate frame nowadays available. It contains 800 stations located at about 500 sites thus assuring a better distribution over the globe compared to past ITRF versions with even more site concentration in Western Europe. Within the ITRF2000 database, about 50% of station positions are determined to better than 1 cm, and about 100 sites have their velocity estimated to or better than 1 mm/yr.

In order to compare the modelling results with geodetic data, the deformation is represented by horizontal eigenvectors of the strain rate tensor. As already observed by Marotta (2005), the comparison between the geodetic and the model eigenvalues allows to quantify the quality of the model. Figure 27 shows the horizontal strain rate eigenvectors derived from the ITRF2000 solutions in Central Europe (blue colours indicate extension and red colours compression) computed for triangular domains following the approach of Devoti et al. (2002). According to this procedure, the horizontal strain rate eigenvalues, i.e.  $\dot{\epsilon}_1$  and  $\dot{\epsilon}_2$ , together with their respective azimuth values are directly computed from the horizontal velocity components as geodetically observed at the vertices of the triangular areas delimited by GPS stations, assuming a linear variation of the horizontal velocity components with respect to their distance. The symmetric component of the velocity gradient tensor yields the eigenvalues and associated eigenvectors of the strain rates.

The main features shown in Figure 27 are: (1) a general SW-NE direction of compression in opposition to a SE-NW directed extension, (2) a dominance of extension over compression at high latitudes, and (3) a general isotropic deformation style at middle latitudes.

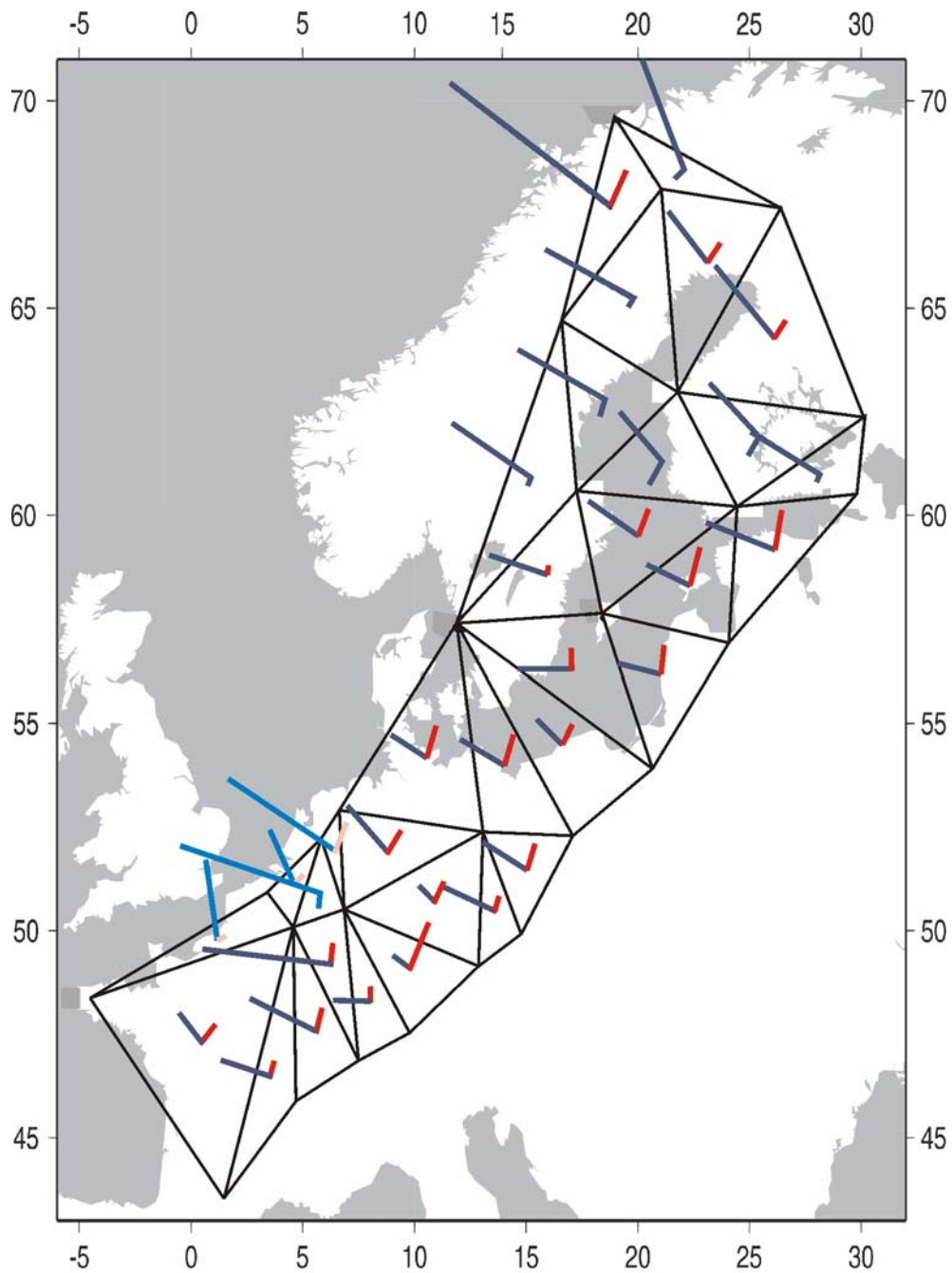


Figure 27. Triangular strain rate eigenvectors derived from the ITRF2000 database in Central Europe (blue indicates extension, and red compression). Thinner light blue and red coloured lines in the left angle indicate non-significant strain rates, modified after Marotta (2005).

### **Stress Field pattern**

The second data set used to test the quality of the results is represented by the stress field as obtained from the “World Stress Map Project” (WSMP, Reinecker et al., 2005). This database provides the direction of the maximum horizontal stress and related stress regime as derived from several sources, such as earthquake focal mechanisms, young geological indicators and

borehole breakouts. These data can be compared to the maximum horizontal component of the stress tensor derived from the model. As usually assumed in any continuum approach of continental deformation, the lithosphere is regarded as an isotropic medium. This assumption is reflected by a rheological formulation which explicitly links strain rates with stress components. Thus, after having obtained the horizontal deformation field, the largest component of the stress tensor,  $S_{Hmax}$ , is easily estimated from the horizontal gradients of the velocity field and from the nodal values of the effective viscosity implemented in the thin-sheet calculations (Ranalli, 1995; Turcotte & Schubert, 2002).

Figure 28 presents stress direction data for the area of the CEBS as derived from the most recent release in 2005 from the WSMP.

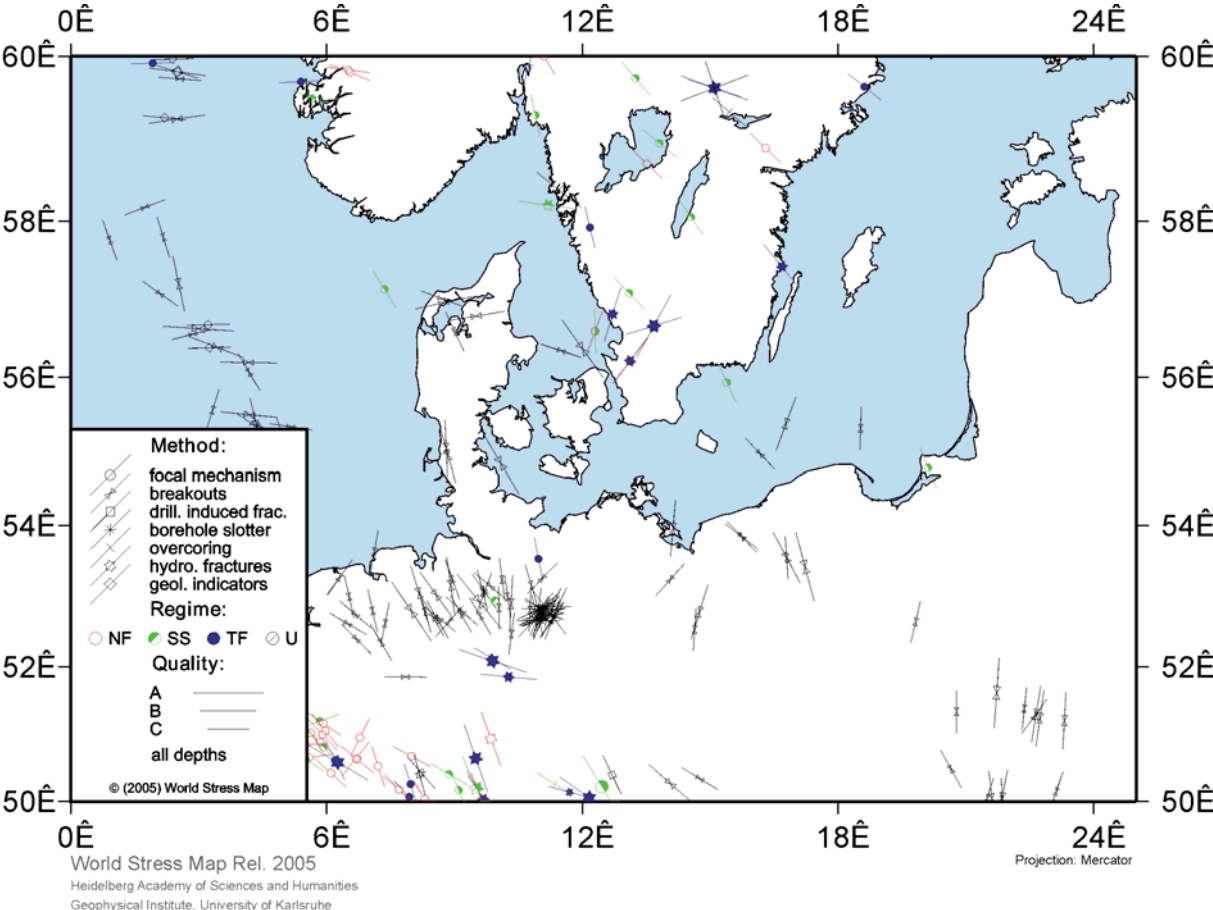


Figure 28. Map showing the direction of the largest horizontal stress for the area under investigation, Reinecker et al. (2005): ‘The release 2005 of the World Stress Map’.

Based on the dominant  $S_{Hmax}$  directions as derived from Figure 28, the regional stress field shows a consistent NW-SE orientation with a mean direction of  $N145^{\circ}E \pm 26^{\circ}$ .

Local deviations in the general stress patterns are found in several areas:

1. GPS measurements demonstrate radial horizontal extension of Fenno-Scandian around the Gulf of Bothnia (e.g. Milne et al., 2001; Jarosinski et al., 2005). In the vicinity of this gulf,  $S_{Hmax}$  directions deviate from the broad scale NW-SE trend and show high scatter in orientations.
2. Breakout measurements from the Polish segment of the Teisseyre-Tornquist Zone show a  $S_{Hmax}$  rotation towards N-S (e.g. Jarosinski et al., 2005).
3. The main deviation in  $S_{Hmax}$  orientations is found under northwestern Poland and northeastern Germany (e.g. Roth & Fleckenstein, 2001; Jarosinski et al., 2005; Reinecker et al., 2005). Under these regions  $S_{Hmax}$  takes a different NNE-SSW to N-S orientation.
4. In the eastern segment of the Polish Carpathians,  $S_{Hmax}$  directions varying between NNE-SSW and ENE-WSW were derived from GPS measurements (Hefty, 1998).

### **Case I: Impact of the sedimentary fill**

The first modelling step evaluates the effects of shallow thermal fluctuations on the strain pattern with special emphasis on the thermal blanketing effect of the sedimentary fill. The relevance of the sedimentary fill in numerical models has been often discussed. There is a widespread consensus that neglecting the sedimentary infill may result in stronger rheological strength envelopes than if the sediments are incorporated.

The internal structure of the CEBS is complicated by a thick sequence of sediments that have been accumulated since the formation of the basin system and throughout its further development under different tectonic and environmental conditions (Ziegler, 1990; Bayer et al., 1999; Krawczyk et al., 2002; Scheck-Wenderoth & Lamarche, 2005; Majdanski et al., 2006).

Figure 29 and Figure 30 show the respective thickness and depth maps for the sedimentary sequences adopted in the present study. These maps have been digitized and adapted to the nodal positions of the integral mesh used in the numerical simulation following a previous work by Scheck-Wenderoth & Lamarche (2005).

Following the work of Scheck-Wenderoth & Lamarche (2005) the sedimentary cover under the CEBS consists of a sequence of five different sedimentary layers of variable thickness. This sequence comprises: (1) Cenozoic clastics, (2) Upper Cretaceous carbonates, (3) Lower Cretaceous clastics-to-Upper Permian (Zechstein) evaporites, (4) Lower Permian (Rotliegend) clastics and (5) Permo-Carboniferous volcanic rocks.

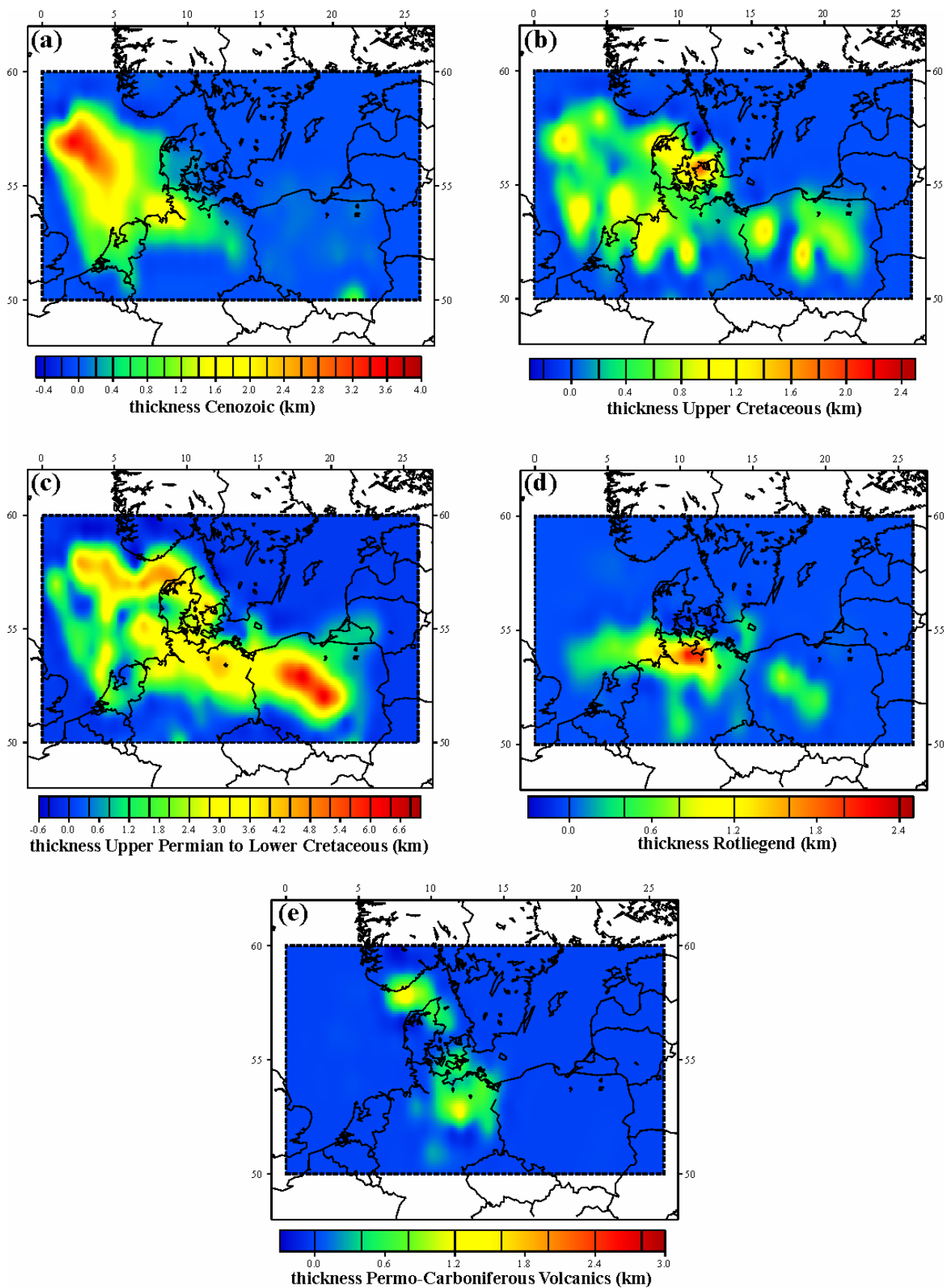


Figure 29. Thickness (km) of the Cenozoic (a), Upper Cretaceous (b), Upper Permian to Lower Cretaceous (c), Rotliegend (d), and Permo-Carboniferous (e) sedimentary layers used in the model calculations. Adapted to the study area from the study of Scheck-Wenderoth & Lamarche (2005).

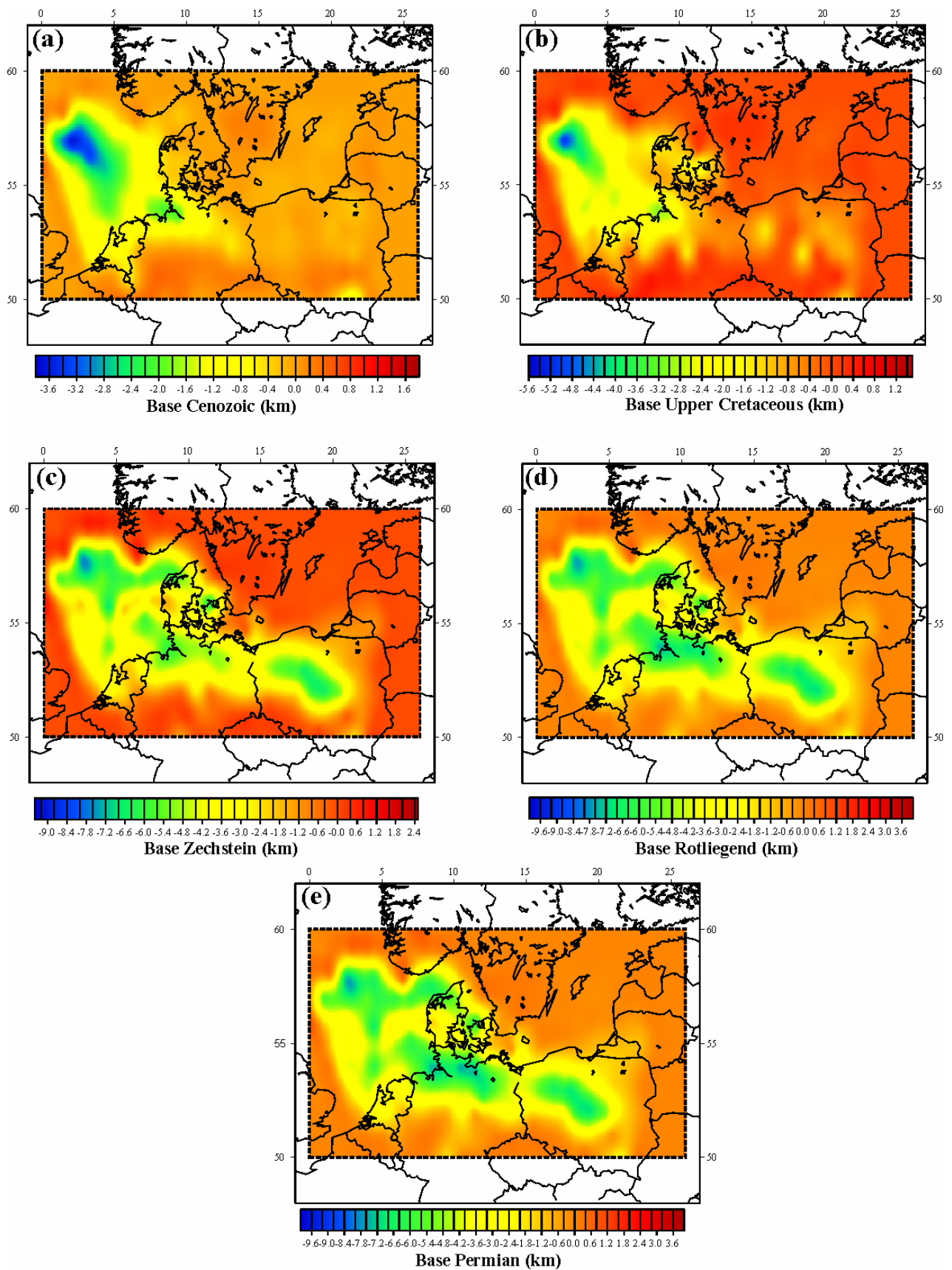


Figure 30. Depth of the base (km) of the Cenozoic (a), Upper Cretaceous (b), Upper Permian to Lower Cretaceous (c), Rotliegend (d), and Permo-Carboniferous (e) sedimentary layers used in the model calculations. Adapted to the study area from Scheck-Wenderoth & Lamarche (2005).

The thickness map of the Cenozoic sediments (Figure 29a) displays a major NNW-SSE trending depocentre in the central North Sea with a maximum of 3.6 km of sedimentary rocks. South of it, this maximum continues into a branch with a N-S-oriented axis offshore the Netherlands. Accordingly, the deepest depressions are oriented NNW-SSE to N-S in the base of Cenozoic surface (Figure 30a).

In the thickness map of the Upper Cretaceous (Figure 29b) the dominant direction of depocentre axes is NW-SE as in the Cenozoic thickness map. However, the Upper Cretaceous shows a more differentiated picture than the Cenozoic. The main depocentre is still located in the central part of the North Sea domain (with maxima up to 5 km of depth) striking NNW-SSE. An additional minor NW-SE-oriented local depocentre is visible in the north-western part of the North German Basin. The corresponding depth map of the Upper Cretaceous (Figure 30b) depicts NW-SE-oriented highs which are clearly visible along the Teisseyre-Tornquist Zone in Poland, along the Sorgenfrei-Tornquist Zone offshore Denmark, along the Ringkøbing-Fyn High and across the Elbe Fault System in the southern part of the basin system.

The cumulative thickness of the Zechstein to Lower Cretaceous deposits (Figure 29c) represents the thickest sedimentary sequence. It shows a rather complex distribution of lows and highs since it integrates a long period of differential subsidence. The basin system is framed by the Tornquist Zone in the north and the Elbe Fault System in the south. The presence of the Ringkøbing-Fyn High is also represented in the map. In contrast with the previous two described maps, Figure 29c evolves two different directions of depocentre axes: (1) NW-SE-trending with maxima under the major Permian basins (i.e. the Norwegian-Danish Basin, the North German Basin and the Polish Trough), and (2) newly formed N-S-trending structures (i.e. Central, Horn and Glückstadt grabens). Accordingly, the base of the Zechstein to Lower Cretaceous (Figure 30c) images a complex pattern of adjacent lows and highs. The basin is framed by the Tornquist Zone in the north and by the Elbe Fault System in the south with the main axes of depocenters striking NW-SE.

The thickness distribution of Lower Permian (Rotliegend) sediments (Figure 29d) shows close similarities with the Zechstein thickness map. It images again a dominant NW-SE structural orientation. The base Rotliegend surface (Figure 30d) resembles the main features already depicted by the Zechstein base surface with an additional deepening below the North German Basin and the Polish Trough (the so called 'Southern Permian Basin' after Ziegler, 1990).

The last sedimentary layer consists of Permo-Carboniferous volcanic rocks (Figure 29e). It shows a maximum accumulation along NW-SE-trending bands at the Sorgenfrei-Tornquist

Zone in northern Denmark, along a NNE-SSW-oriented domain under the north-eastern part of Germany and along a NW-SE-striking lineament under Poland. At the base Permian surface (Figure 30e) the outlines of the main Permian basins (i.e. the Norwegian-Danish Basin, the North German Basin, and the Polish Trough) are visible. These three main basins are then cut and partially offset by N-S-oriented Mesozoic grabens (i.e. the Central, Horn and Glückstadt grabens).

In the present study case, the other vertical lithospheric structures considered comprise:

- (1) An upper crust at a constant depth of 20 km.
- (2) A lower crust down to the Moho boundary of Figure 23.
- (3) A lithospheric mantle at a constant depth of 100 km.

Figure 31 shows the bottom surface layers as implemented in the thermal and rheological models to enter the lateral variations of the different structures considered in the present study case.

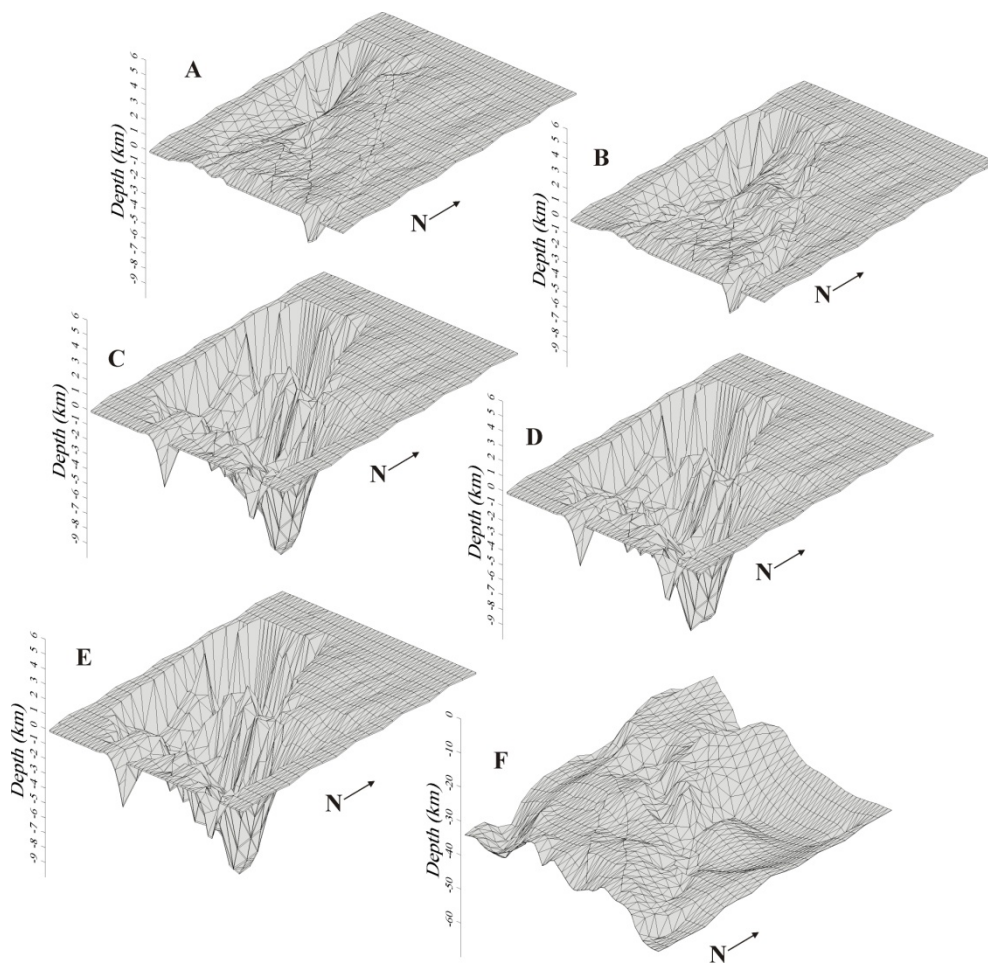


Figure 31. Depth surface maps for the different structural layers (sediments+crust) as integrated in the thermal and rheological models for the Case I. **A:** Cenozoic strata; **B:** Cretaceous; **C:** Rotliegend; **D:** Zechstein; **E:** Permo-Carboniferous volcanics; **F:** Moho.

The complexity of the basin system prevents an exact description of all parameters and processes. Consequently, a *conceptual model* must be constructed that can highlight the main physical properties and boundary and/or initial conditions. In order to perform numerical simulations of the geothermal field and of the strength profiles each structural layer in which the lithosphere is subdivided (sediments, upper and lower crust and lithospheric mantle) is modelled by a basin-scale averaged dominant lithology corresponding to appropriate physical properties. Within each structural unit, lithology and related thermo-mechanical properties are considered constant according to Table 2.2.

Stratigraphic unit	Thermal parameters	Creep parameters			
	Thermal conductivity ( $k$ ) ( $\text{Wm}^{-1}\text{K}^{-1}$ )	Radiogenic heat production ( $H$ ) ( $\text{Wm}^{-3}$ )	$\dot{\epsilon}_0$ ( $\text{MPa}^{-n}\text{s}^{-1}$ )	$E$ ( $\text{KJmol}^{-1}$ )	$N$
Cenozoic	1.5	$3 \cdot 10^{-7}$	$5.4 \cdot 10^{-6}$	184	2.1
Upper Cretaceous	1.9	$3 \cdot 10^{-7}$	$1.35 \cdot 10^{-6}$	130	2.3
Upper Permian- Lower Cretaceous	3.5	$0.9 \cdot 10^{-7}$	$5 \cdot 10^{-6}$	102	5.3
Rotieglend	2.4	$1 \cdot 10^{-6}$	$5.4 \cdot 10^{-6}$	184	2.1
Permo- Carboniferous Volcanics	2.5	$2 \cdot 10^{-6}$	$3.4 \cdot 10^{-6}$	198	1.9
Upper crust (quartzite-dry)	2.5	$1.5 \cdot 10^{-7}$	$6.7 \cdot 10^{-6}$	156	2.4
Lower crust (diabase-dry)	2.8	$1 \cdot 10^{-6}$	$2.0 \times 10^{-4}$	260	3.4
Mantle (olivine-dry)	3.4	0.0	$2.4 \times 10^4$	532	3.5

Flow parameters for the Dorn's law

Petrology	Activation Energy $Q_D$ ( $\text{KJmol}^{-1}$ )	Initial constant $A_D$ ( $\text{s}^{-1}$ )	Dorn's law stress $\sigma_o$ ( $\text{GPa}$ )
Olivine (dry)	535	$5.7 \times 10^{11}$	8.5

Table 2.2. Thermal and creep parameters used to solve the thermal field and the strength calculations, after Goetze & Evans (1979); Carter & Tsenn (1987); Wilks & Carter (1990); Ranalli 1995.

The adopted values for the thermal and rheological parameters for the different sedimentary layers are consistent with previous 3-D thermal modelling studies (e.g. Bayer et al., 1997; Ondrack et al., 1998), investigations on subsidence history of the basin system (e.g. Scheck & Bayer, 1999; Van Wees & Stephenson., 1995), gravity analysis (e.g. Scheck-Wenderoth et al., 1999; Bayer et al., 1999), and interpreted seismic velocities based on wide-angle seismic data (e.g. Bayer et al., 1999). The thermo-mechanical analogues for the upper crust, lower crust and lithospheric mantle are based upon assumptions constrained by experiments and observations. The deeper vertical structures consist of an upper crust of granodiorite/diorite to quartzite composition, a lower crust of high grade metamorphic granulites or mafic dunites, and an ultramafic (olivine/peridotite) lithospheric mantle. In the present study, no lateral discontinuities in rock composition and behaviour are considered.

To account for the observed significant lateral variations in thickness of the sedimentary sequence a relative denser grid in the vertical direction (resolution of about 200 m) is used in both the thermal and strength models. A coarser grid with a vertical resolution of 1 km is adopted for the crustal and mantle domains. The present accuracy of the structural model and the assumptions related to the theoretical formulation of both the thermal and strength models limit the results to a representation of only regional basin-scale trends. Nevertheless, the model results should be regarded as a reasonable first order approximation.

Figure 32 provides maps of the computed temperature distributions at selected depths.

Common to all maps is that the temperature field shows some irregularities in the horizontal direction.

Figure 32a illustrates the temperature variations at a constant depth of 5 km, within the sedimentary fill. The temperature distribution parallels the present-day depth position of the sediments and is a consequence of the interaction of the spatial distribution of thermal conductivities and sedimentary thicknesses. Down to 10 km, Figure 32b, the general trend is almost identical. The distribution of overall sediments thickness and their low thermal conductivities is a sufficient measure for the resulting temperature pattern. Accordingly, low temperatures in Figure 32b correlate with regions of minimum sedimentary thickness and are a consequence of the relative lower thermal conductivities of the sedimentary rocks in comparison to those typical of the crystalline crust.

Figure 32c illustrates the temperature variations at the Moho boundary. The deep temperature field provides a somewhat different scenario. Reasonably, deep lower crustal variations in the geotherm parallel the regional variations in the crust-to-mantle boundary. The deeper the Moho discontinuity, the higher the temperatures are.

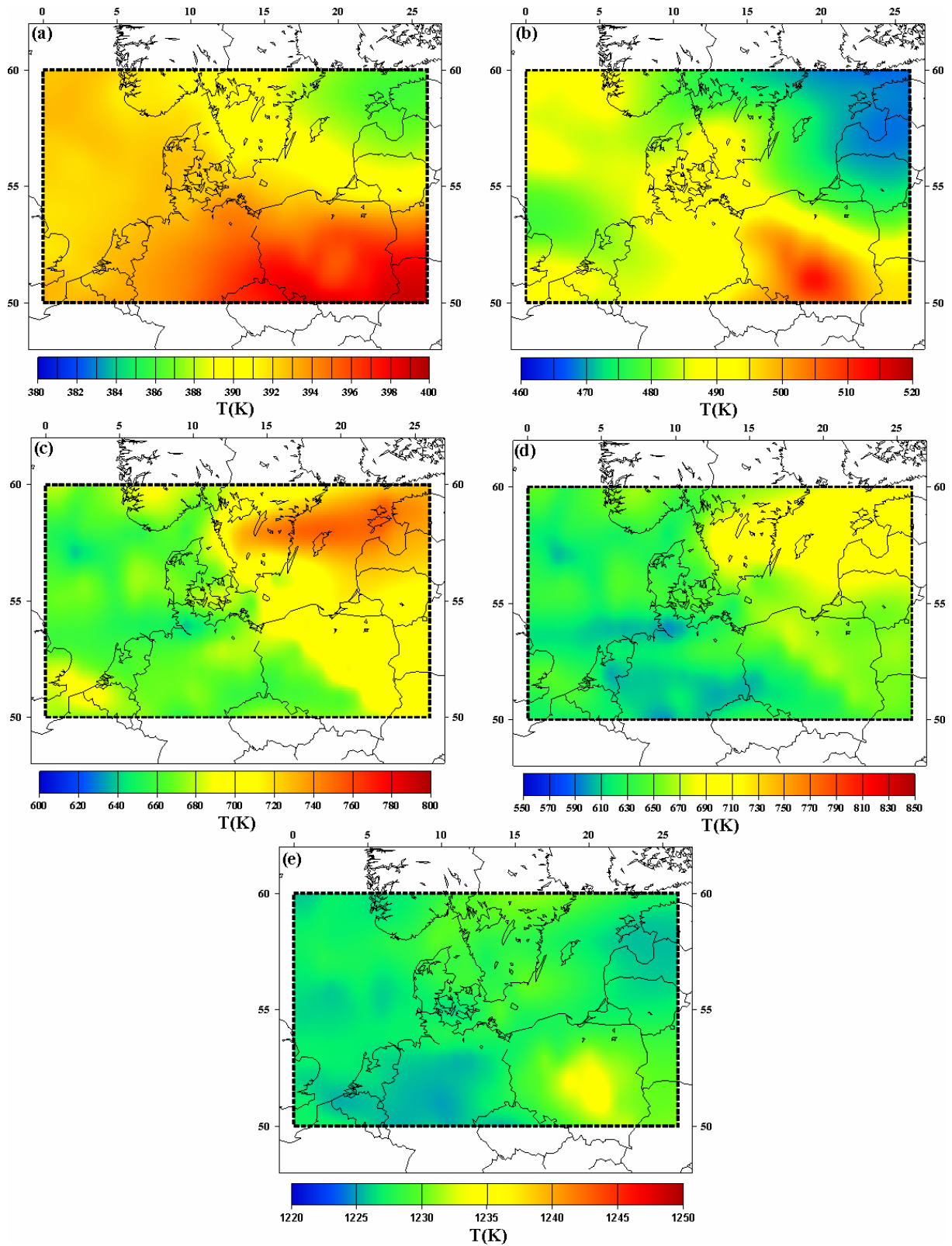


Figure 32. Temperature variations at different depths as derived from three dimensional modelling, Case I.

The influence of the deep crustal layer is still visible, though having minor influence, at greater depths, down to about 60 km, as shown in Figure 32d. Going deeper, the adopted boundary condition at the bottom of the model starts to dominate the geometry of the thermal

field. The presence of an isothermal boundary at a constant depth of 100 km results in small or even in the absence of temperature gradients at greater depths as nicely illustrated by the temperature distribution at a depth of 70 km in Figure 32e.

The thermal structure displayed by Figure 32 is resembled by the vertical cross-section profiles of Figure 34a,b (see Figure 33 for their respective locations).

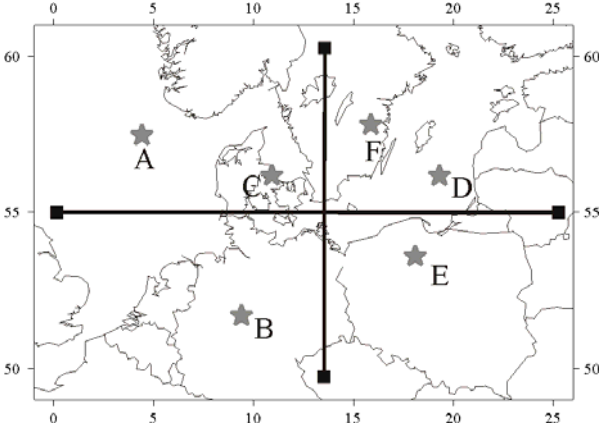


Figure 33. Location of the six strength profiles of Figure 35 (grey stars), and of the two thermal cross sections of Figure 34 (solid lines).

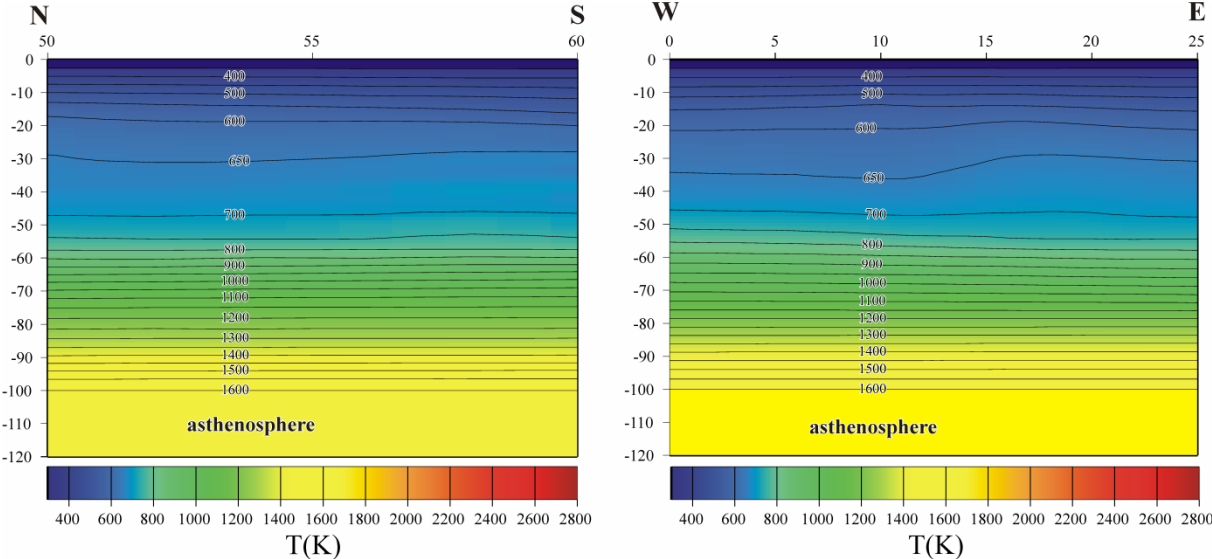


Figure 34. 2-D thermal cross sections for Case I. See Figure 33 for the locations of the respective profiles.

In both cross-sections local variations in the shallow temperature field (down to 20 km of depth) are restricted to regions characterized by a thick sedimentary sequence. The influence of the near-surface thermal field can be projected as deep as the upper crust. In contrast, temperature variations in the deep crust are controlled by the topography of the Moho boundary transition. Reaching greater depths, down to 70 km, the uniform boundary condition

at the model bottom starts to dominate the geothermal field thus resulting in no thermal fluctuations along both profiles.

Figure 35 illustrates examples of lithospheric strength profiles calculated at six different nodal locations. The respective sites (grey stars in the map of Figure 33) are chosen at locations with different values of sedimentary thicknesses and Moho depths in order to resemble different levels of lithospheric strength.

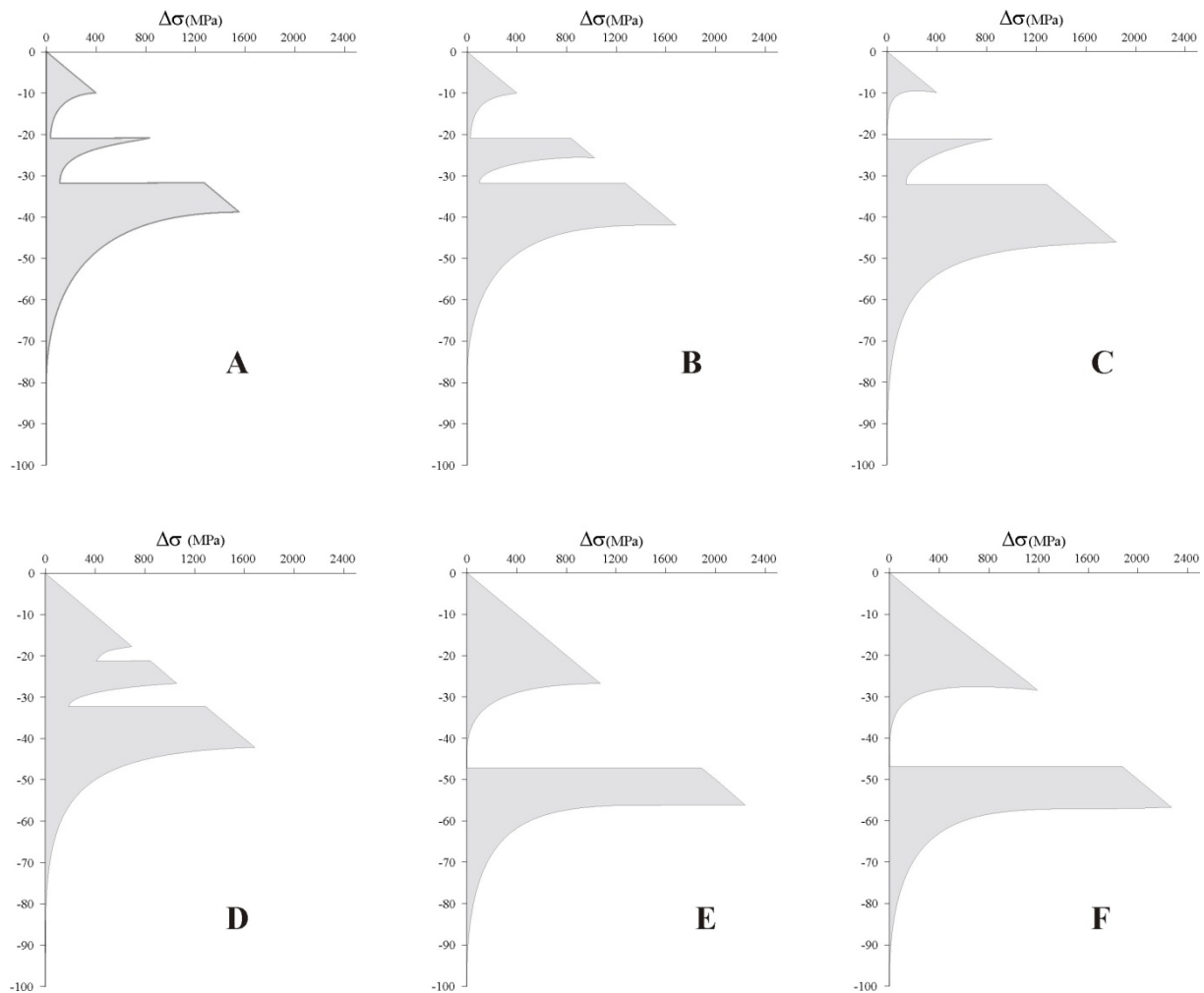


Figure 35. Examples of strength profiles obtained by the rheological modelling at several locations (see Figure 33) with different sedimentary and crustal thickness.

Within the rheological formulation adopted in the study, the ductile contribution to the total strength of the lithosphere strongly depends on the temperature field, equation (2.25) and (2.26). As already discussed above, the presence of an asthenosphere-lithosphere isothermal boundary at a constant depth of 100 km reflects the absence of temperature gradients at depths greater than the Moho discontinuity (Figure 32 and Figure 34). This rather homogeneous thermal structure results in a rheological behaviour which is similar for all the strength

profiles within the mantle portion. The strength envelopes in Figure 35 depict a common clear weakening of the lower portion of the lithosphere. This results in mechanical decoupling of the crustal and upper mantle at the Moho transition. As already indicated by the thermal results in Figure 32 and Figure 34, shallower depth levels of the crust-to-mantle transition are generally characterized by lower temperatures. Due to the inverse relationship between ductile strength and temperature, shallower Moho depths (lower temperatures at constant depths) result in relative shallow brittle-to-ductile transitions and consequent more pronounced brittle domains in the lithospheric mantle with depths (profiles A, B, C). On the contrary locations associated with deeper Moho depth levels (profiles D, E, F) are characterized by a deeper brittle-to-ductile transition and relative less deep extent of the brittle domain in the mantle portion. Therefore, a relative increase in strength of the mantle domains under areas with shallow crust-to-mantle transitions should result. However, comparing the profiles of Figure 35, an increase in the magnitude of the deviatoric stress (from  $\Delta\sigma=1000 \text{ MPa}$  to values  $> 2000\text{MPa}$ ) is evident moving from locations associated with shallower Moho depths (profiles A, B, C) towards those characterized by deeper Moho values (profiles D, E, F). Since the total lithospheric strength is given by the depth integral of the yield stress envelopes, the observed increase in the deviatoric stress for those locations associated with a deeper Moho results in relative greater contributions of the mantle portion to the total integrated lithospheric strength for those areas.

The main differences in the rheological structure are limited to the shallow crustal portion of the lithosphere. Areas with thick sediments are characterized by a more visible mechanical decoupling at depths of about 15-20 km than areas where almost no sediments occur (compare profiles A, B, C with profiles D, E, F). This reflects the weakening effect of the sedimentary layer due to their lower values of thermal conductivities with respect to common crystalline crustal rocks thus inducing higher temperatures in the uppermost parts of the lithosphere under areas of high sedimentation. Moreover, a thick sedimentary sequence superposed on a relative shallow Moho (profiles A, B, C) reduces the crustal contribution to the total lithospheric strength. On the contrary, under areas without sediments, (profiles E, F), or where sediments are accompanied by a deeper Moho (profile D), an almost continuous increase of upper crustal strength occurs.

Relatively small differences in the total lithospheric strength are expected from the rheological profiles of Figure 35. Accordingly to sediment distribution and Moho depth, small strength gradients occur in the map of the total lithospheric strength of Figure 36.

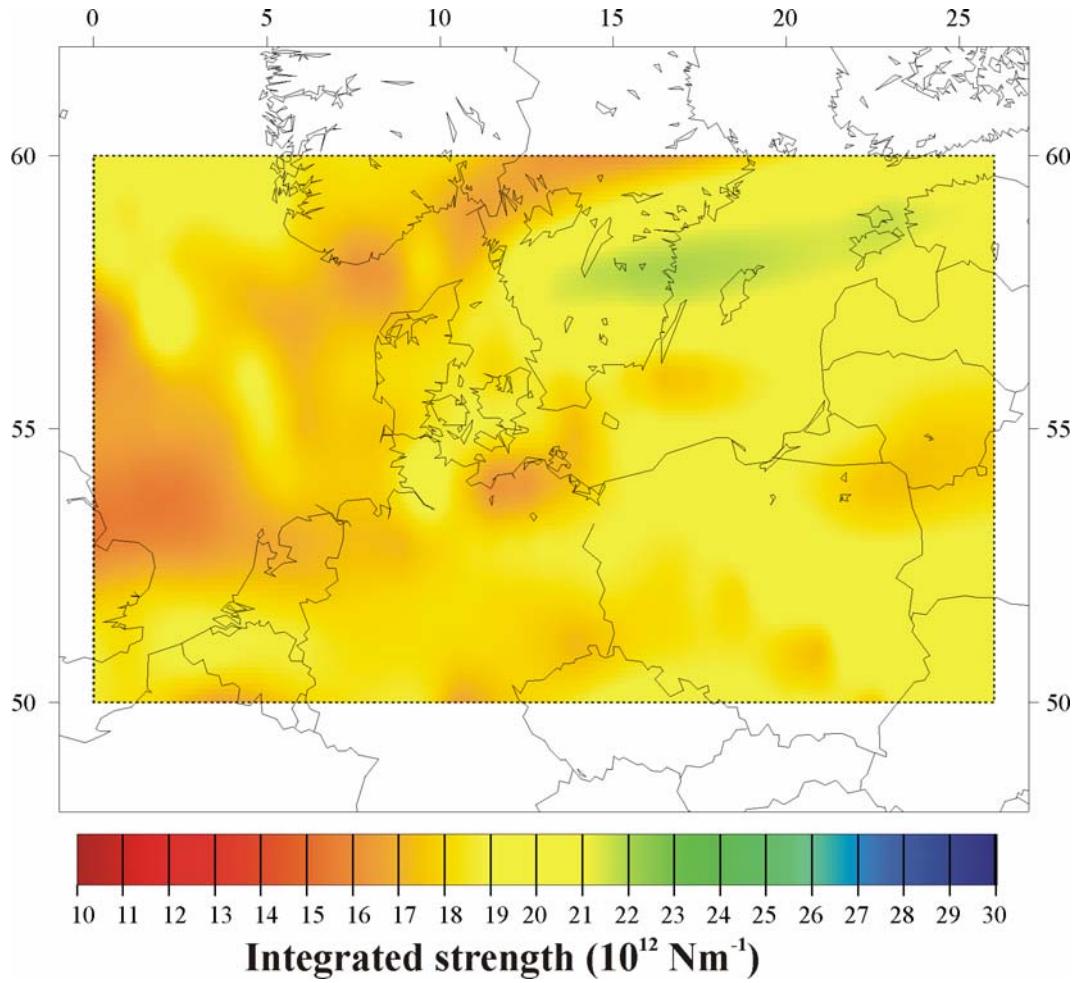


Figure 36. Integrated lithospheric (crustal+mantle contributions) strength map for the CEBS.

Lateral variations in the total strength of the lithosphere are modelled between a relative stiffer domain ( $20 \cdot 10^{12} \text{ Nm}^{-1} \leq \sigma_L \leq 23 \cdot 10^{12} \text{ Nm}^{-1}$ ) in the eastern part of the study area and a more mobile domain in the west ( $15 \cdot 10^{12} \text{ Nm}^{-1} \leq \sigma_L \leq 20 \cdot 10^{12} \text{ Nm}^{-1}$ ). Lowest lithospheric strength values parallel the present-day distribution of the sediments, while relative higher strength values are found under areas of almost no sedimentation or deep Moho levels.

Figure 37 shows the corresponding lateral variations of the effective viscosity as calculated from equations (2.29).

Due to the linear relation between  $\bar{\eta}$  and the total lithospheric strength,  $\sigma_L$ , the results of Figure 37 illustrate a similar trend in variations as those in Figure 36. An almost homogeneous setting is imaged with lateral variations in the effective viscosity within one order of magnitude ( $10^{26}$ - $10^{27} \text{ Pas}^{-1}$ ). Increased viscosity is found in the eastern parts of the study area.

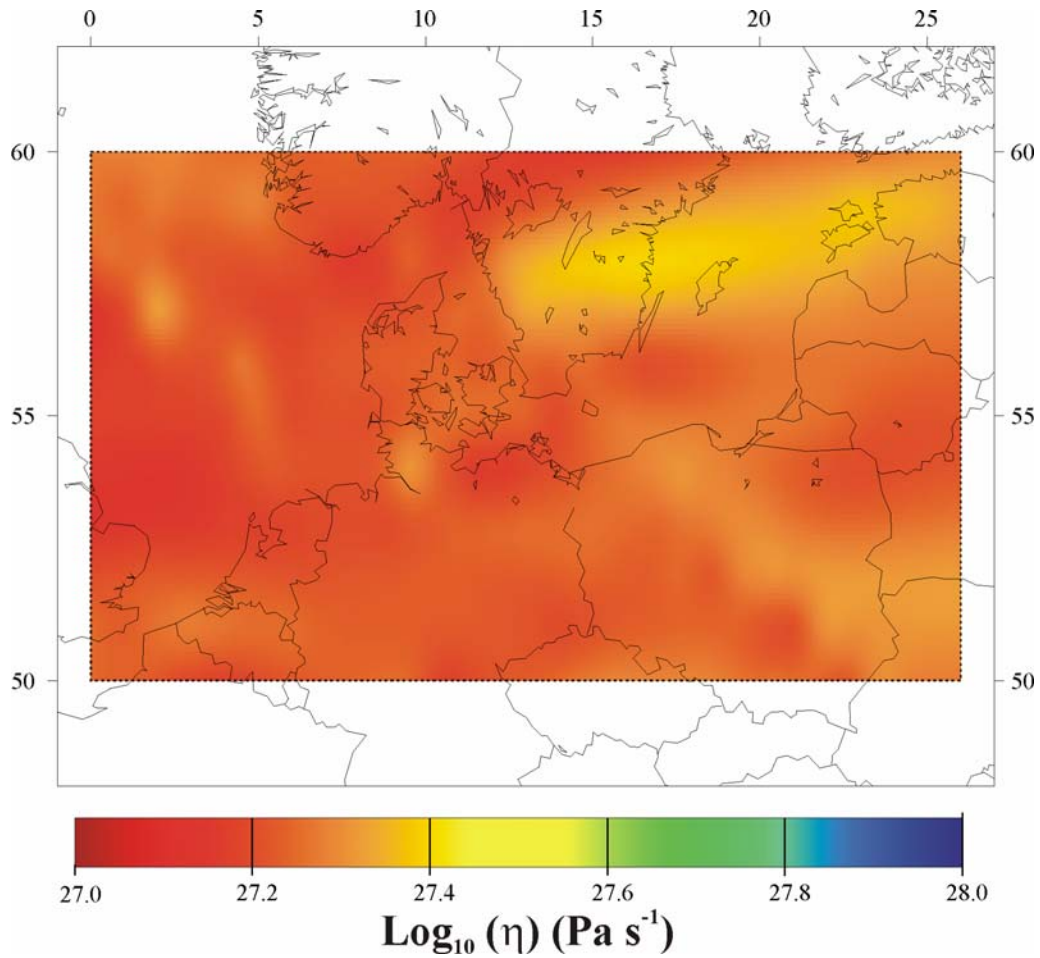


Figure 37. Variations of the effective viscosity  $\bar{\eta}$ . Contour colours refer to a logarithmic scale.

Within the theoretical framework of the thin sheet approach the gradients of viscosity values are too small to induce any detectable variation in the regional and/or local kinematics. Therefore, model results are expected to be almost completely driven by the adopted boundary conditions. This hypothesis is confirmed by the horizontal deformation velocities obtained from numerical integration of (2.22a,b) as shown in Figure 38.

The velocity field is almost totally driven by the geometry of the imposed boundary conditions. In the northern and western areas, the velocity vectors are characterized by a broad-scale south-west orientation. This long wavelength character in direction of horizontal velocities at high latitudes reflects the dominance of push forces related to the Middle Atlantic. An anti clock-wise bending in the horizontal velocity vectors is visible in the central part of the study domain, where the Africa-to-Eurasia collision starts to overpower the Atlantic ridge push forces. As expected, along the southern border of the domain the velocity vectors present a different orientation (southeast-to-northwest) due to the active collision-dominated tectonic setting.

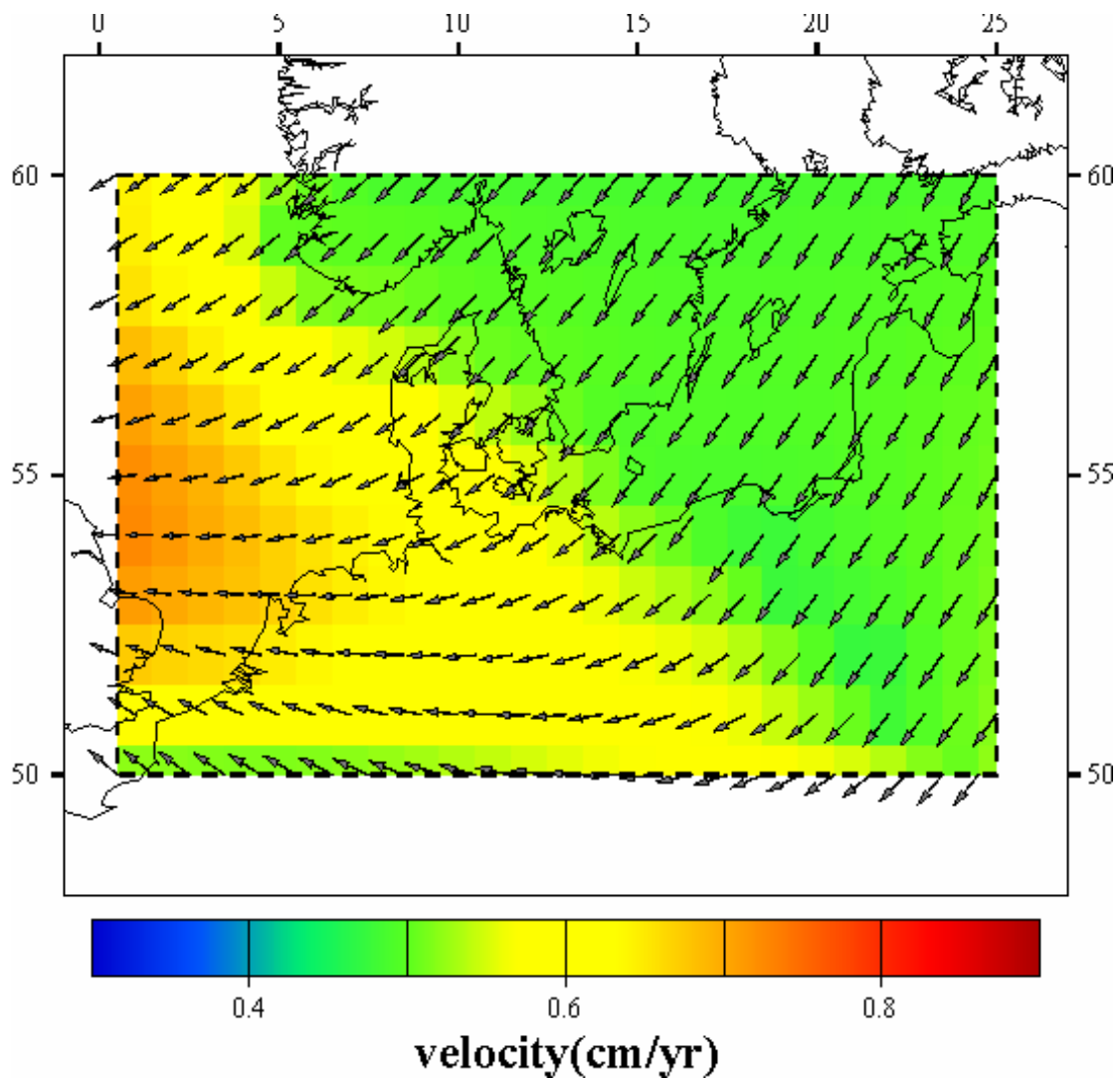


Figure 38. Horizontal deformation velocity vectors as derived from the numerical integral model.

The main effects connected to the inclusion of the sedimentary fill and a variable crustal thickness concerns the amplitude of the velocity vectors. Two distinct areas in terms of amplitudes of velocity vectors evolve. Minor amplitudes of horizontal deformation velocity (green colours of the background colour map) are modelled in the eastern part of the domain, the East European Craton-Baltic Shield. The modelled kinematics may have two concurring causes. Minor magnitudes of deformation velocity vectors within the eastern domain may result from its more distal location with respect to the effective plate-boundary conditions. At the same time, a somewhat stiffer lithosphere due the combined lack of sediments and a thicker crustal body may shield this domain causing the drop in the magnitudes of the velocity field.

On the contrary, relative higher magnitudes of horizontal deformation velocity vectors are modelled under the Variscan crust more to the west. More likely, relative thick sedimentary deposits combined with a shallower Moho discontinuity induce a gradual increase in the amplitudes of the velocity vectors under this area.

Figure 39 illustrates the results obtained in terms of horizontal strain rates.

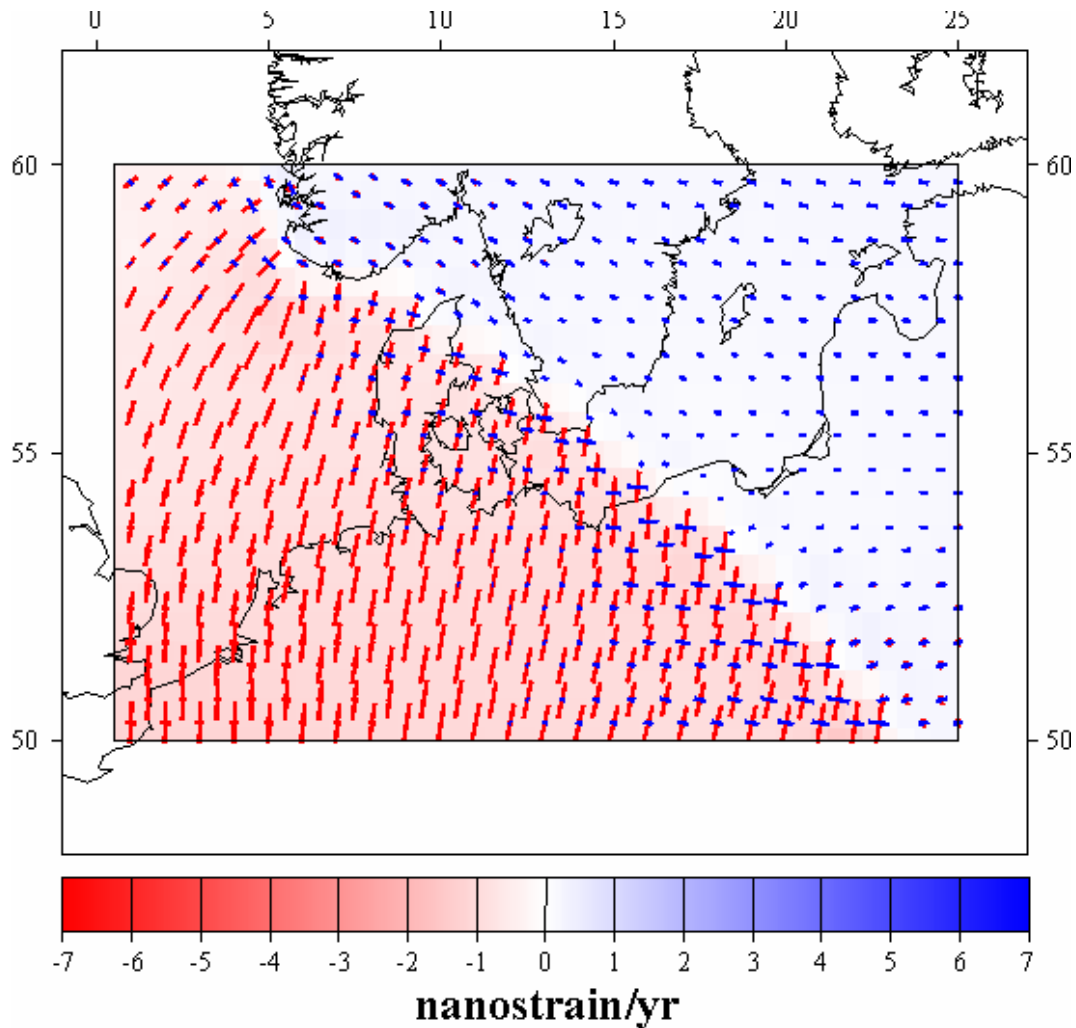


Figure 39. Horizontal strain rate eigenvalues (background colour map) and eigenvectors (hyphens) derived from the velocity field of Figure 38. Variations in the sediments thickness and in the Moho topography provide a general agreement with geodetic observations.

A flat asthenosphere with a somewhat stiffer rheology related to the Moho topography and the sediments fill provides the general trend of horizontal deformation as observed from GPS data (Figure 27) under the given boundary conditions. An overall extensional setting (blue colours) oriented mainly NW-SE characterizes the north-eastern part of the domain where almost no sediments are presented. In agreement with the velocity field of Figure 38, amplitudes of

horizontal strain rate eigenvectors (length of the hyphens) are much lower in the north-eastern domain than under areas more to the south-west. A gradual change in kinematic activity occurs moving toward the western portion of the study area. N-S- to NE-SW-oriented compression (red colours) becomes comparable to extension in the central part of the study area along the lithospheric-scale Tornquist Zone. Compression becomes dominant under the Variscan domain more to the west. The inclusion of the sedimentary fill proves to induce higher strain-rate eigenvalues without affecting the deformation style. This may reflect the observed increase in strain rate values (as represented by the lengths of the hyphens of Figure 39) in the western region where the main sediments accumulation occurred.

Figure 40 shows the modelled  $S_{Hmax}$  orientation as obtained from the horizontal strain rate results of Figure 39.

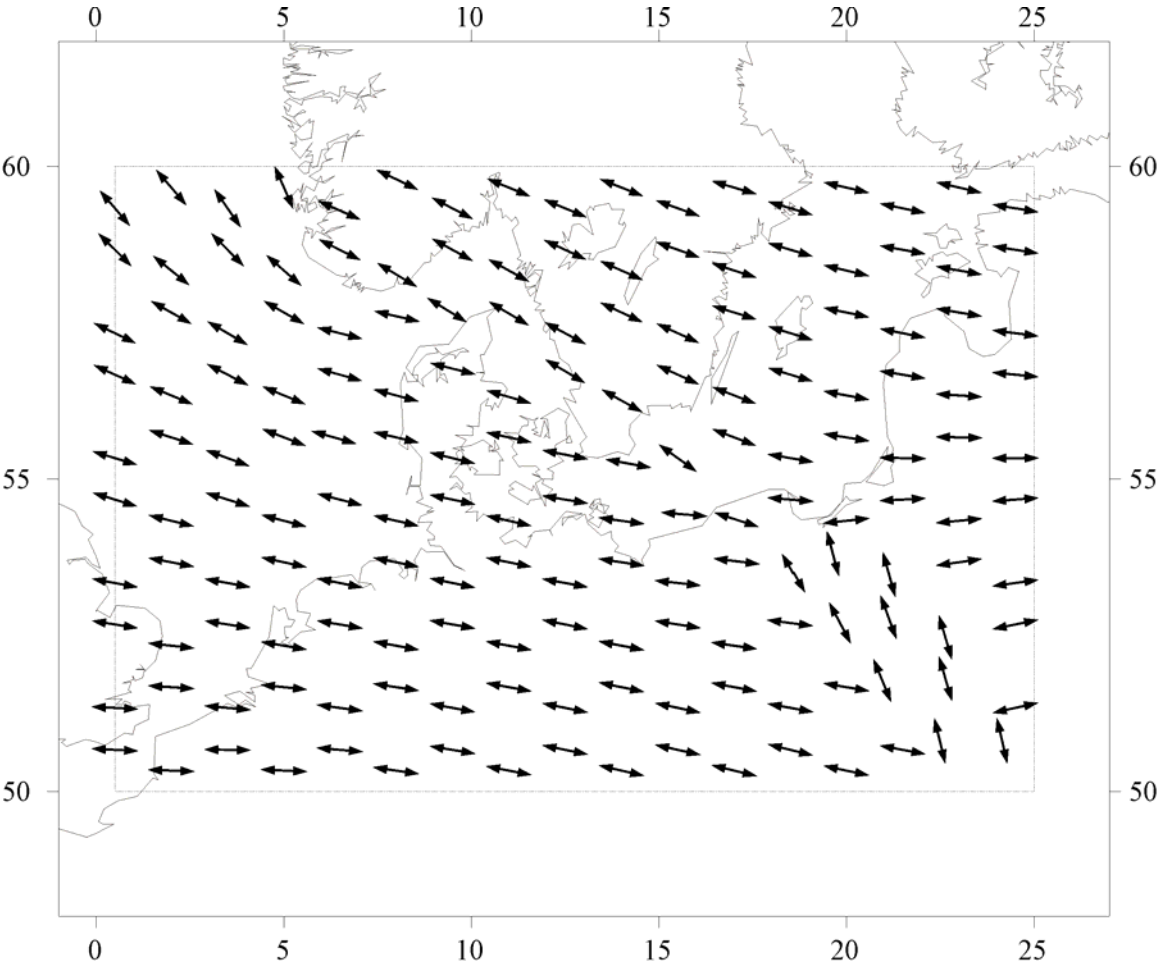


Figure 40.  $S_{Hmax}$  orientation as predicted from the numerical study Case I.

The averaged orientation of maximum compression is explained by the combined effects of push forces along the Atlantic ridge system and collision forces along the southern European border superimposed on a simplified lithospheric structure. The dynamic setting depicted in Figure 40 confirms the long wavelength character of the present-day stress field under north and Central Europe as expected for a typical stress field caused by plate boundary forces alone. Indeed, plate boundary forces are probably one of the main controlling factors for the stress orientation in the CEBS. A dominance of NW-SE orientation of maximum compression is shown with an average direction of  $\sim N150^\circ E$ . The stress results of Figure 40 may be regarded satisfactory concerning regional trends whereas they lack matching the observed local deviations in the  $S_{Hmax}$  orientations.

The simple model does not integrate any heterogeneity in the structure of the lithosphere. Consequently, the model results of Figure 39 and Figure 40 can account only for first order features of observed data under the effective boundary conditions adopted in the model formulation. In the framework of models characterized by a realistic brittle-to-ductile rheology, results are strongly influenced by the chosen rheological and thermal parameters. This motivates the development of more realistic heterogeneous models as described below, Case II and Case III. The comparison between simplified uniform and more complex heterogeneous models, subjected to the same boundary conditions, enables to understand the influence of heterogeneities on the style of continental deformation.

### **Case II: shallow mantle thermal effects**

Local, small-wavelengths variations in heat flow and thermal regime are believed to be closely related to variations in near-surface radiogenic heat production, thermal conductivity contrasts within the sedimentary fill and different lithological compositions in the upper crust. Regional, full lithospheric-scale, increase or decrease in heat flow and/or geotherms is principally caused by gradients in the depth of the asthenosphere-lithosphere isothermal boundary and associated changes in the internal deep structure of the lithosphere. Shallow (deep) depth levels for the lithosphere-to-asthenosphere transition result in increased (decreased) heat flux and temperatures in the upper mantle and in the lower crust.

The thermal lithosphere is found to vary markedly under the CEBS: from about 85-100 km beneath the Permian and Mesozoic basins, to about 150 km in the ‘Tornquist Fan’ sensu Thybo 1990, and about 200-250 km in the central and north-eastern shield areas.

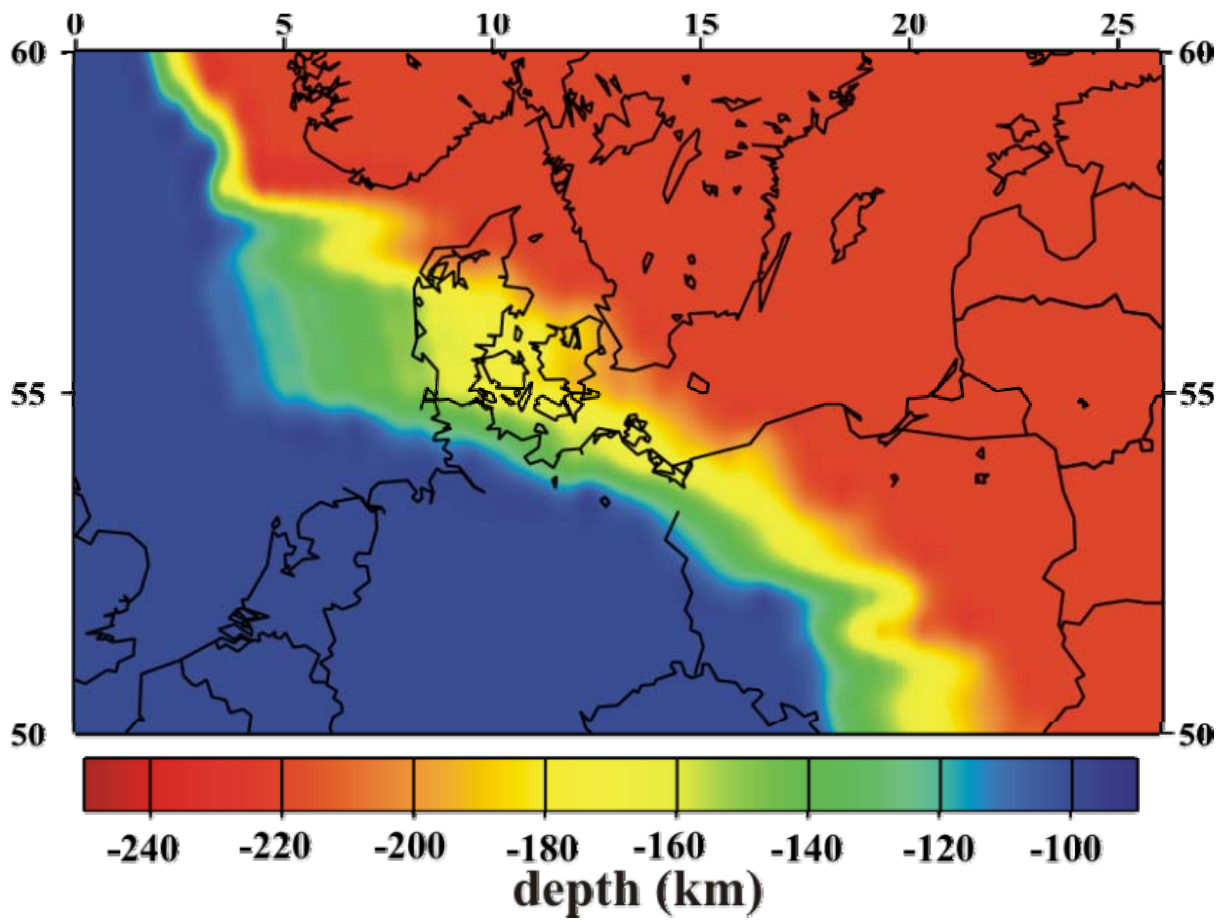


Figure 41. Map showing the lithosphere-asthenosphere isothermal boundary used in the thermal and rheological calculations, Case II. Constrained from the TOR seismic results (e.g. Gregersen & Voss, 2002; Shomali et al., 2006).

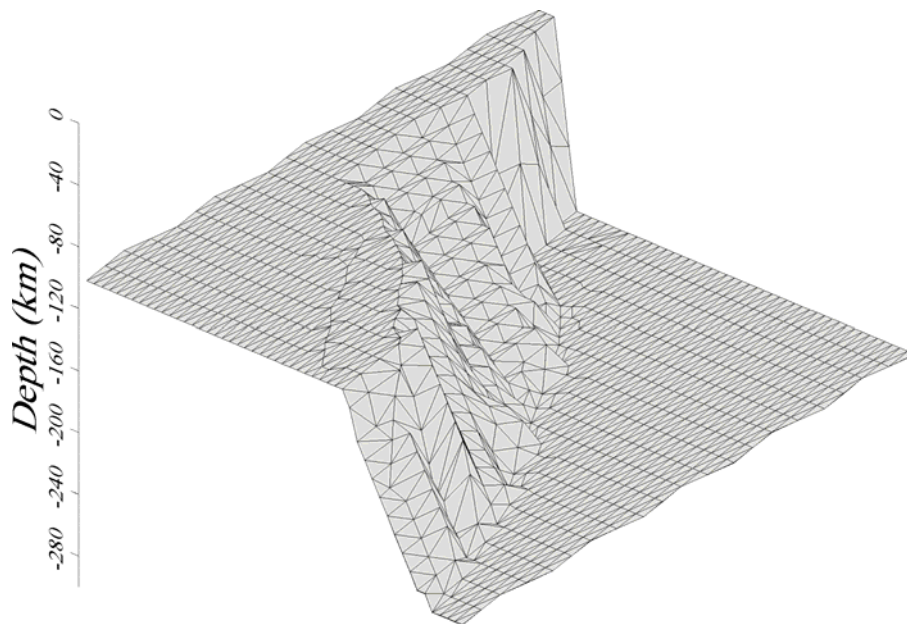


Figure 42. Surface map generated to integrate the asthenosphere-lithosphere isothermal boundary in the thermal and rheological model.

## **Mantle thickness variations**

In a similar fashion as the Moho discontinuity (Figure 23), the asthenosphere-lithosphere boundary shows a heterogeneous pattern with significant lateral fluctuations (e.g. Gregersen & Voss, 2002; Shomali et al., 2006). Large geophysical contrasts have been recognized in the structure of the deep lithosphere under the Central European Basin (e.g. Spackman et al., 1993; Pedersen et al., 1994; Babuska & Plomerova, 2004; Bijward et al., 1998; Voss et al., 2006; Bayer et al., 1999; Krawczyk et al., 2002; Gregersen & Voss, 2002; Shomali et al., 2006). The observed shallow mantle discontinuities are reproduced in the models following the constraints given by the results derived from the project TOR (Teleseismic Tomography across the Tornquist Zone in Germany-Denmark-Sweden). This large scale seismological project operated a seismic array between the Harz Mountains in northern Germany, across Denmark and into the Baltic Shield in Sweden for a period of one year. The TOR project was mainly concentrated on the deep lithosphere and clearly delineates the presence of three different lithospheric structures constrained by P-wave travel time tomography, surface wave dispersion, P- and S-wave anisotropy and P-wave scattering.

Following the TOR results, the transition in lithospheric thickness is considered to be sharp and steep in two places. It goes all the way through the lithosphere at the northern rim of the Tornquist Zone, near the border between southern Sweden and Denmark. Here the lithosphere difference reaches depths of 200-250 km. A smaller lithosphere gradient (from 90-100 km of depth to 120-150 km) is found near the southern edge of the Ringkøbing-Fyn High, just north of the border between southern Denmark and northern Germany. A gradual transition domain is documented across what has been called the ‘Tornquist Fan’, i.e. the area extending across the Tornquist Zone and the Ringkøbing-Fyn High.

Figure 41 illustrates the above described variations in lithospheric thickness extrapolated outside the TOR experiment following the main tectonic boundaries. In Figure 42 the bottom surface map generated to represent the asthenosphere-lithosphere topography in the thermal and rheological models is also shown.

The other vertical structures considered are the same as in the previous study case: sediments, upper crust and lower crust. This is done in order to isolate and quantify the relevance of shallow mantle thermal effects on the recent tectonic setting of the CEBS. Accordingly, thermal and rheological parameters adopted in the simulations are the same as in Case I, summarized in Table 2.2.

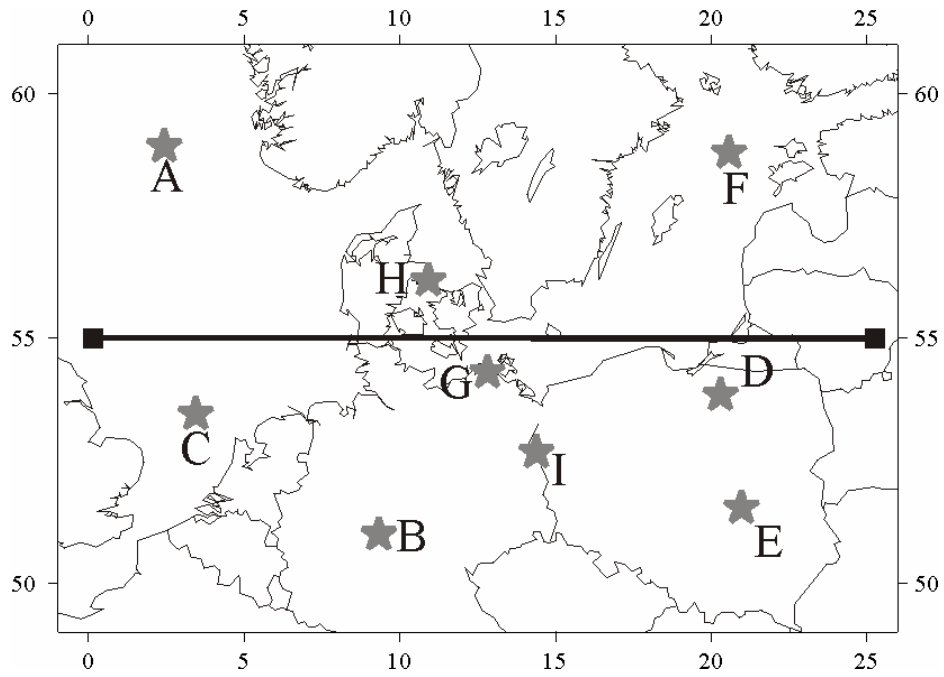


Figure 43. Location of the strength profiles of Figure 45 (grey stars), and of the cross section of Figure 44 (solid line).

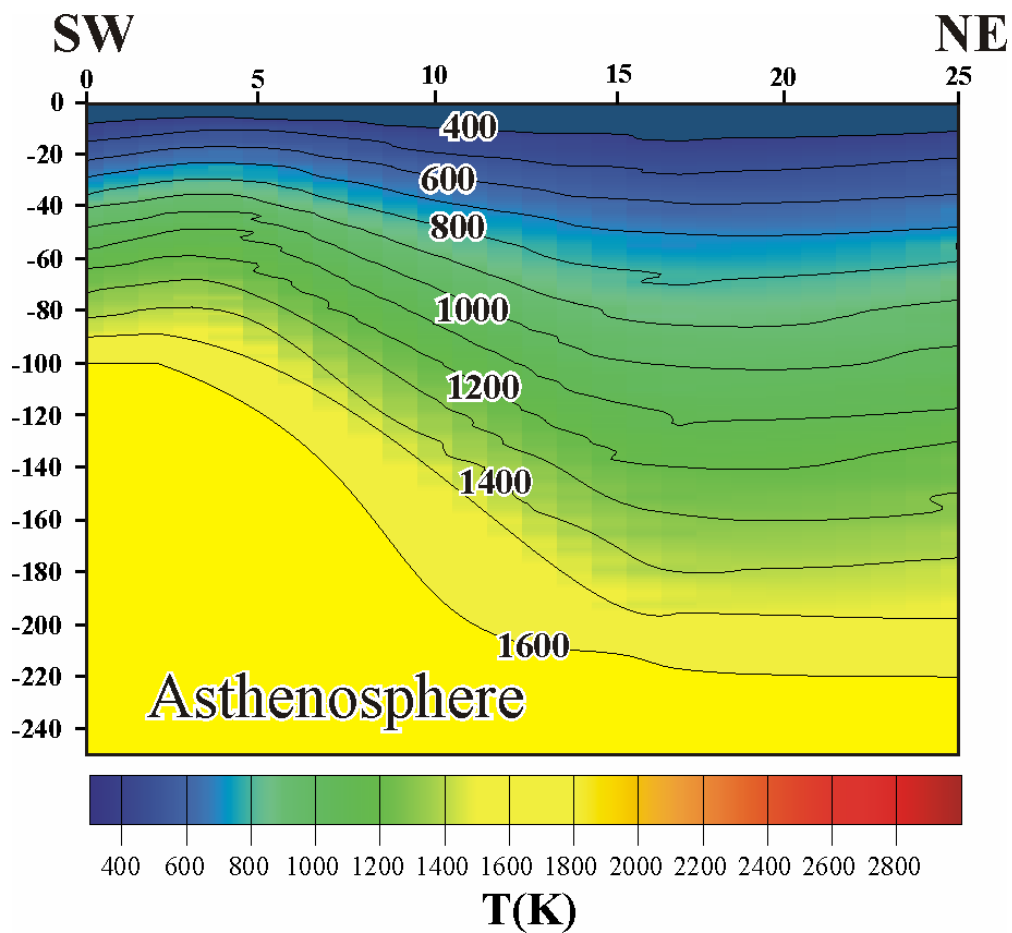


Figure 44. Two-dimensional cross-section for the temperature distribution resulting from a variable asthenosphere-lithosphere boundary, see Figure 43 for its location.

Figure 44 illustrates a west-east cross-section running in the x-z plane as shown by the solid line of Figure 43, cutting the entire basin throughout its length at latitude of 55 °N. This profile may be regarded as a suitable working example for the present study case since it crosses all the main geological and tectonic (sub)domains with different values in thickness of the thermal lithosphere.

The thermal results provide in Figure 44 show clearly how the shape and dimensions of the asthenosphere-lithosphere boundary (Figure 41) govern the geometry of the thermal structure of the lithosphere. A distinct temperature gradient occurs between the cold shield areas in the NE (i.e. East European Craton and Baltic domain) and the warmer regions in the SW (i.e. Variscan domain) of the profile. Between these two distinct regions, a transitional domain with rather smooth lateral temperature variations characterizes the central section of the profile. Temperature gradients related to the bottom model boundary condition loses importance reaching shallower depths thus resulting in a more homogeneous upper crustal thermal structure with respect to the underlying portion of the lithosphere.

Strength predictions are very sensitive to the adopted lithospheric thickness. Therefore, significant variations in lithospheric strength are expected from the variations in mantle temperatures as discussed above. Generally, increased lithospheric thickness results in pronounced increase of lithospheric strength mainly related to a cooler upper mantle below the Moho. Conversely, a reduced lithospheric thickness results in significantly lower integrated strength values due to shallower levels for the isothermal asthenosphere boundary. Consequently, hot regions can be translated into ‘mechanically weak/stress-sensitive’ domains and cold regions into ‘mechanically stiff and stable’. Following the temperature results summarized in Figure 44, it is possible to distinguish three domains in terms of lithospheric strength: (1) a relative weak, continental Variscan domain in the west and south-west part of the study area, (2) a cold, stiff and stable lithospheric domain beneath the East European Craton and the Baltic Shield in the eastern part of the system (east the Tornquist Zone), and (3) a transition domain extending between these two regions between the Elbe Line and the Ringkøbing-Fyn-High.

To test this hypothesis, six strength profiles are shown in Figure 45, see Figure 43 for their locations.

Profiles (A,B,C) are taken within the Variscan domain. They resemble areas characterized by averaged low lithospheric strength values. The strength envelopes depict an overall weakening of the lower crust and a corresponding decoupling of the crustal and mantle parts of the lithosphere at the Moho transition under all three locations. The presence of a shallow

asthenosphere-lithosphere level (~100 km of depth) results in a negligible contribution of the mantle portion to the total lithospheric strength.

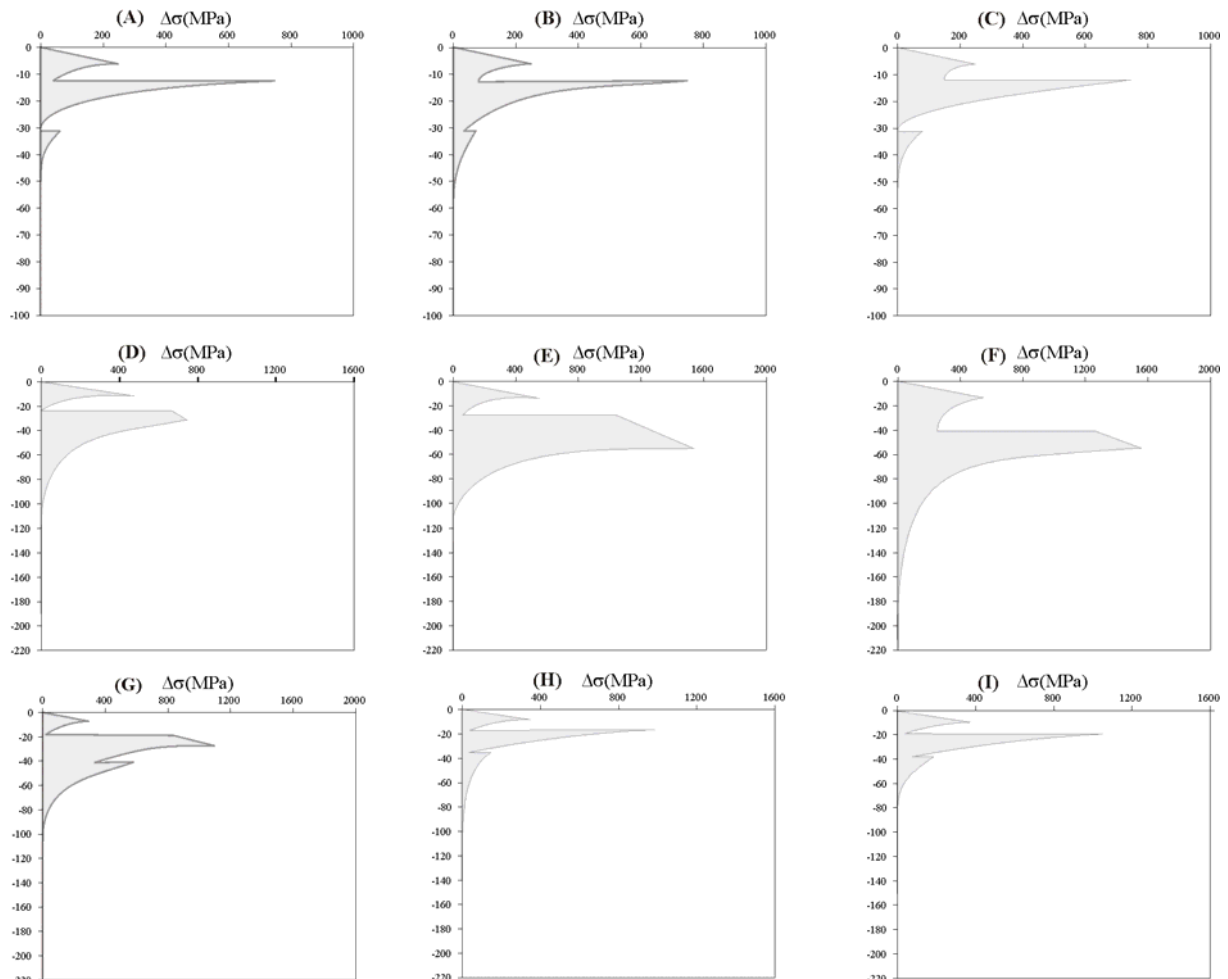


Figure 45. Examples of strength profiles at different locations for the study Case II. See Figure 43 for the respective locations.

Profiles (D,E,F) are taken within the stiff and strong East European Craton. In contrast with the strength envelopes taken within the Variscan domain, an increase in the strength of the mantle is visible. This increase in mantle strength is more pronounced for locations associated with a shallower Moho discontinuity, compare for example strength profile E with strength profile F. Shallower levels of the Moho discontinuity result in extension of the brittle domain at greater depths in the mantle. In the case of very deep crust-to-mantle transitions (strength profile D) no brittle deformation occurs in the mantle domain.

Profiles (G,H,I) refer to the transitional domain. The asthenosphere-lithosphere isothermal boundary varies between 150 km (profile G), 160 km (profile H) and 170 km of depth (profile I). All three profiles are characterized by negligible strength of the mantle domain. Main differences are related to the rheological behaviour of the crust with increased crustal strength

for those profiles characterized by deeper levels of the asthenosphere-lithosphere transition (profile H and profile I).

In general, the strength envelopes of Figure 45 suggest a gradual increase in the total strength of the lithosphere moving from the Variscan domain to the East European Craton region.

The strength envelopes of Figure 45 have been calculated at a number of discrete nodal points within the study domain. Consequently, they provide only limited information on regional lateral variations of lithospheric strength as induced by shallow mantle thermal fluctuations. To overcome this limitation, Figure 46 shows the integrated strength under compression of the entire lithosphere for the study area.

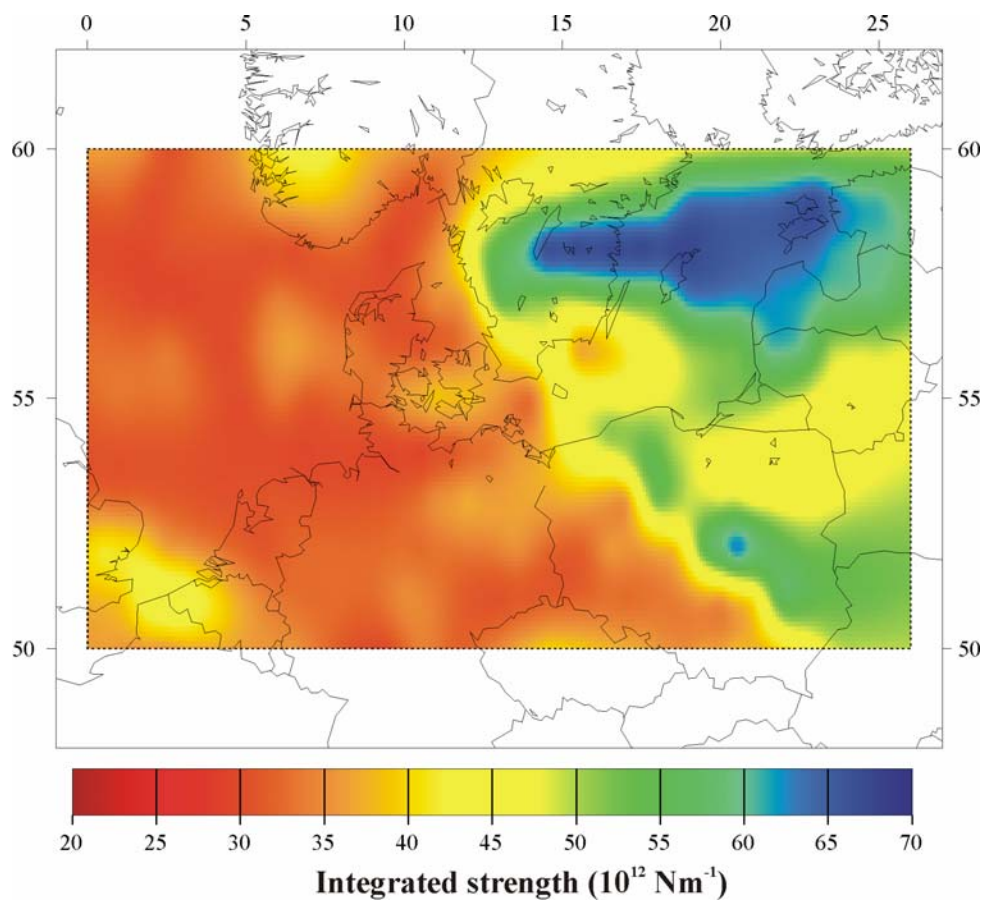


Figure 46. Integrated lithospheric strength map under compression for the CEBS. Due to the topography of the asthenosphere-lithosphere boundary, two regions in terms of lithospheric strength are delineated.

The map of the integrated lithospheric strength images a regional rheological setting in agreement with the outcomes of the strength profiles of Figure 45. Comparing the strength results as shown in Figure 36 (Case I) with those depicted in Figure 46, a general increase in lithospheric strength is visible. At the same time, compared to Figure 36 the differences are more pronounced and structural. The gradual increase in lithospheric strength towards the

eastern part of the domain demonstrates that lateral variations in lithospheric strength strongly reflect the geometry of the thermal lithosphere. Variations in lithospheric strength are primarily related to variations in the thermal structure of the lithosphere which are structurally connected to thermal perturbations of the sub-lithospheric upper mantle. Consequently, the stronger domain occurs in the colder eastern part of the study area where the depth of the asthenosphere-lithosphere reaches its greatest values. Local highs in strength within this area are then associated with shallow Moho transitions. A strong gradient in lithospheric strength occurs along the Tornquist Zone. This reflects the presence a major axis of thermally weakened lithosphere under the areas to the west of the Tornquist Zone.

Within the transitional domain at the asthenosphere-lithosphere level, the lithospheric strength increases ( $\sigma_L \approx 40 \cdot 10^{12} \text{ Nm}^{-1}$ ) under the Ringkøbing Fyn High and in the easternmost part of the North German Basin where the Moho reaches greater depths.

Figure 47 illustrates the corresponding lateral variations of the effective viscosity.

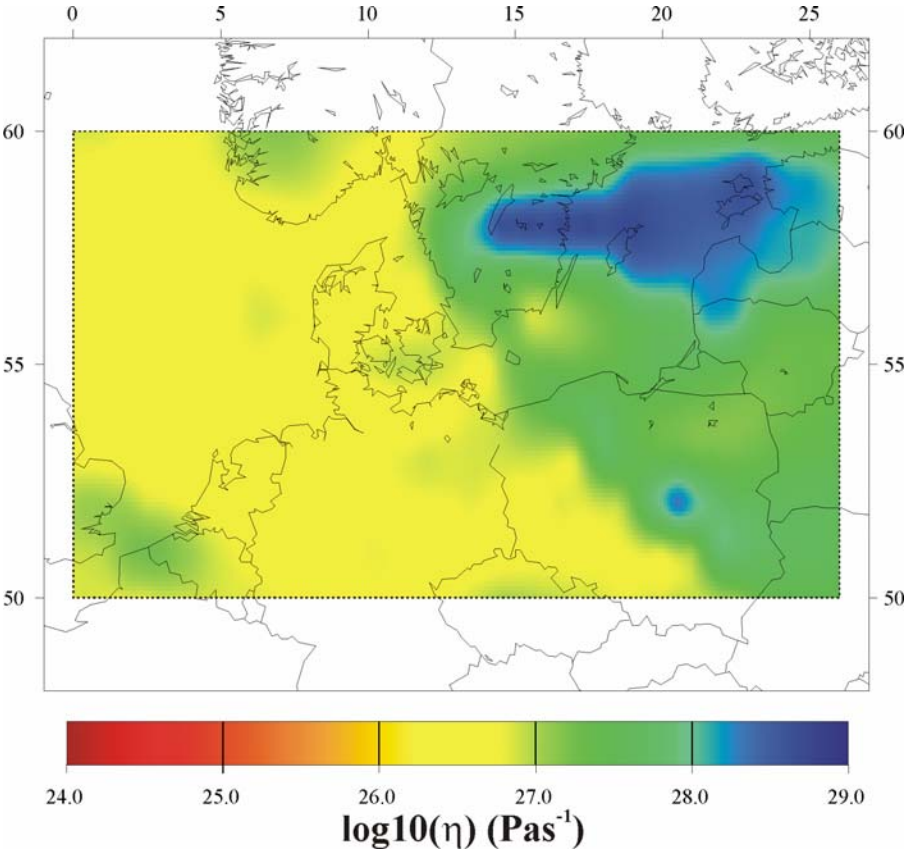


Figure 47. Lateral variations in the effective viscosity ( $\bar{\eta}$ ) for the CEBS obtained modelling lateral variations in the lithosphere thickness.

As expected, the trend of viscosity gradients within the study area parallels the variations in total lithospheric strength of Figure 46. A close relation between the topography of the asthenosphere-lithosphere boundary and lateral variations in the effective viscosity may be inferred from the results of Figure 47. More precisely, two (sub)regions in terms of effective viscosity evolve: an area of very low viscosity values ( $\sim 10^{26} \text{ Pas}^{-1}$ ) west to the Tornquist Zone and a domain of high viscosity values ( $\sim 10^{28-29} \text{ Pas}^{-1}$ ) in the shield areas to the east. To the west of the Tornquist Zone, local high values of viscosity are still visible under the Ringkøbing Fyn High and in the easternmost part of the North German Basin. Viscosity gradients between these two strength domains range within two orders of magnitude, enough to provide significant variations in the deformation pattern under the given boundary conditions.

This suggestion finds a first confirmation by the the horizontal deformation velocity vectors shown in Figure 48.

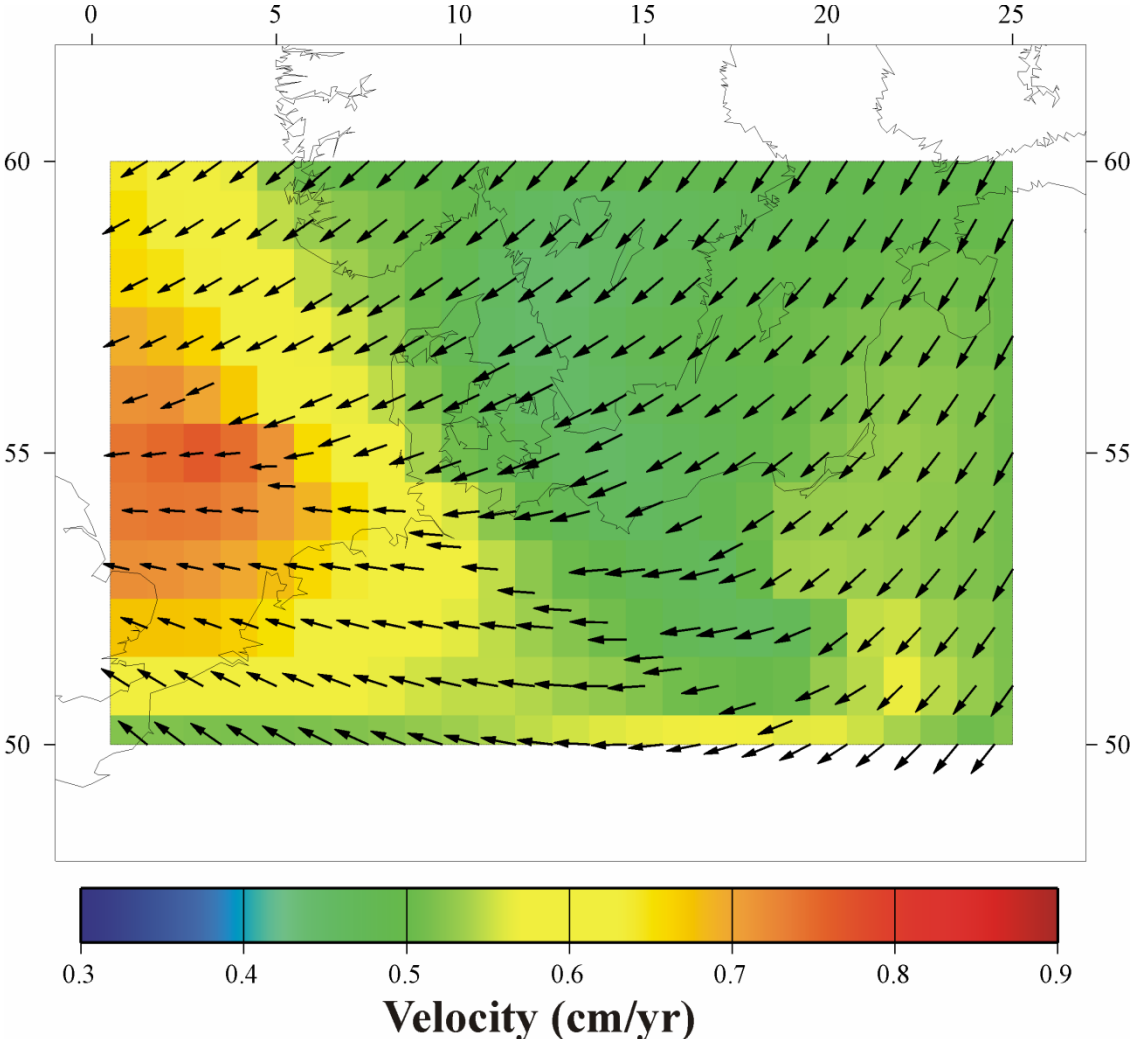


Figure 48. Horizontal deformation velocity field as obtained for Case II.

The horizontal deformation field shows a long-wavelength character in the orientation of velocity vectors in agreement with geodetic observations. Minor magnitudes of velocity vectors (green colours) are modelled under areas associated with deeper lithosphere values. A systematic bending of velocity vectors parallels the geometry of the topography of the asthenosphere-lithosphere boundary in the central part of the study area.

Figure 49 illustrates the results in terms of horizontal strain rate eigenvectors (hyphens) and eigenvalues (background colour map). The regional broad scale deformation style is still observed and fits with geodetically observations. Moreover new features in the present-day kinematics are appearing.

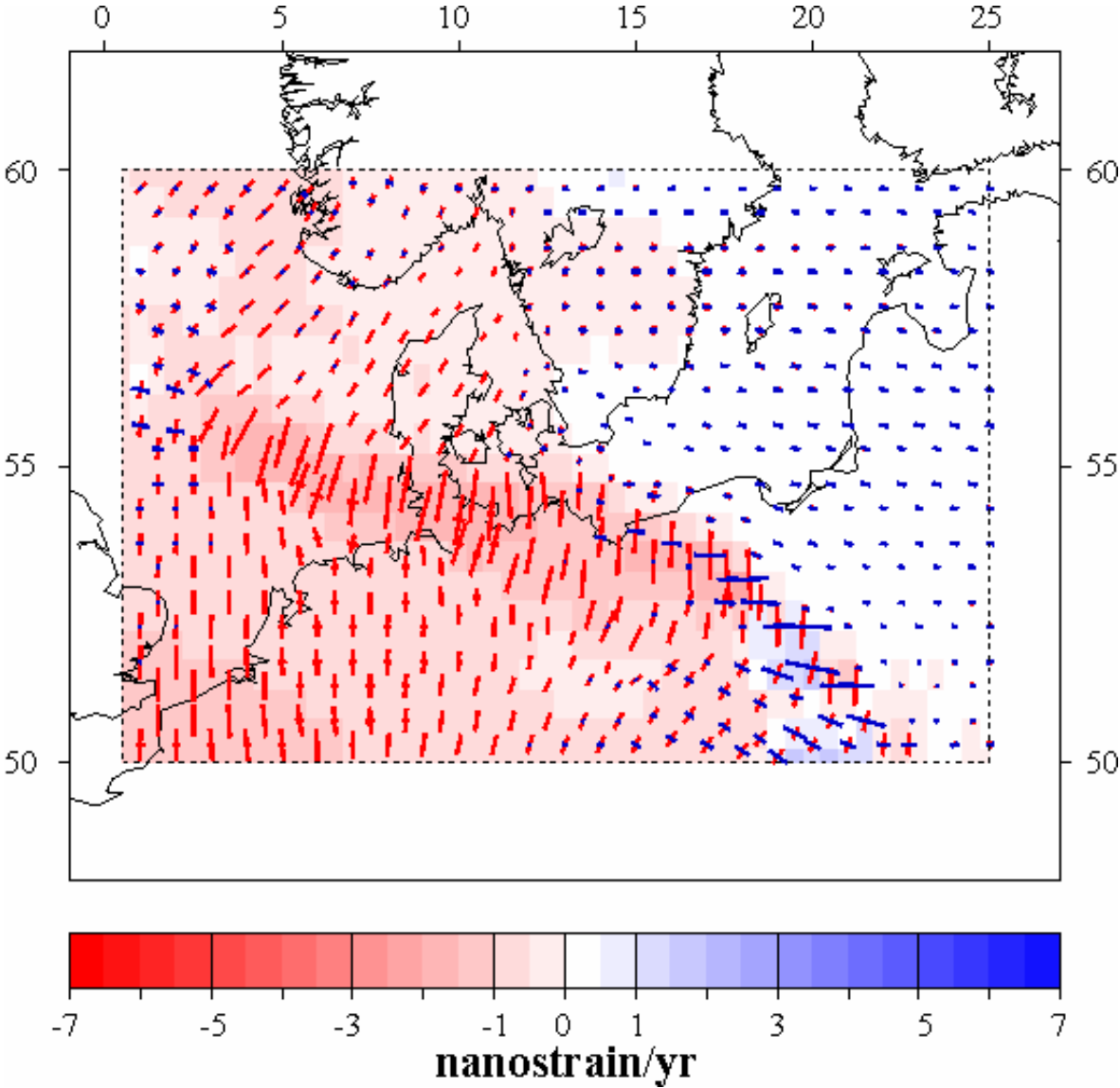


Figure 49. Horizontal strain rate eigenvalues (background colour map) and eigenvectors (hyphens) obtained modelling a variable asthenosphere-lithosphere boundary.

Due to the topography of the asthenosphere-lithosphere boundary the model now generates strain localization concentrated along the Polish Trough and under the region extending between the Sorgenfrei-Tornquist-Zone and the Elbe Line, i.e. under the southern margin of the Ringkøbing Fyn High. The presence of a stiffer lithosphere below the transitional domain along the Ringkøbing Fyn High and in the Polish segment of the Tornquist Zone prevents a release of deformation in the surrounding areas. This results in high strain rate values under these domains and in a sudden drop of strain rate amplitudes under more distal areas. At the same time, the modelled rheological contrast determines variations in the orientation of the strain rate eigenvalues. The reproduced rheological heterogeneities affect the direction of the strain-rate eigenvectors leading to changes in the azimuth of the eigenvectors. Along the southern border of the domain compression is mainly N-S-oriented. Reaching the borders of the transitional domain at the asthenosphere level, a bending in the orientation of the strain rate eigenvectors towards NNE-SSW occurs, providing better agreement with geodetic observations.

Figure 50 illustrates the results in terms of  $S_{Hmax}$  direction as obtained from the strain rate shown in Figure 49. The broad-scale dynamic setting is resembled with a consistent NW-SE orientation of maximum compression, mean  $S_{Hmax}$  orientation is N140°E.

NW-SE  $S_{Hmax}$  orientation becomes progressively less dominant towards the eastern domain of the study area as indicated by the presence of a component of NE-SW-oriented compression (mean orientation about N220°E).

A clock-wise bending in the  $S_{Hmax}$  orientation (toward NE-SW) occurs under northwestern Poland. The region of the observed deviation in the direction of maximum compression is limited by the Teisseyre branch of the Tonquist Zone in the north and northeast. The strong strength gradient along the Teisseyre-Tornquist Zone prevents transfer of stresses within the stronger region of the Baltic Shield. This less efficient transfer of stress within the basin causes the observed rotation in the  $S_{Hmax}$  orientation. Further changes in the  $S_{Hmax}$  orientations occur within the stable lithosphere of the Baltic domain. In agreement with breakout measurements (e.g. Jarosinski, 2005), maximum compression follow a N-S orientation. The modelled changes in the  $S_{Hmax}$  direction north and south the Teisseyre-Tornquist Zone favour strike-slip reactivation of this lithospheric structure under the active plate forces and are consistent with GPS measurements (e.g. Pan et al., 2001) as well as with the seismicity observed in Scania (e.g. Wahlstrom & Grünthal, 1994).

The calculated largest horizontal stress field is able to reproduce the fan-like opening in the  $S_{Hmax}$  orientation within a limited area compared with observations. In northeastern Germany,

under the North East German Basin, the components of the largest horizontal stress are preferentially orientated along a N-S direction without resembling the observed opening in the  $S_{Hmax}$  direction (e.g. Roth & Fleckenstein, 2001; Jarosinski 2005; Reinecker et al., 2005).

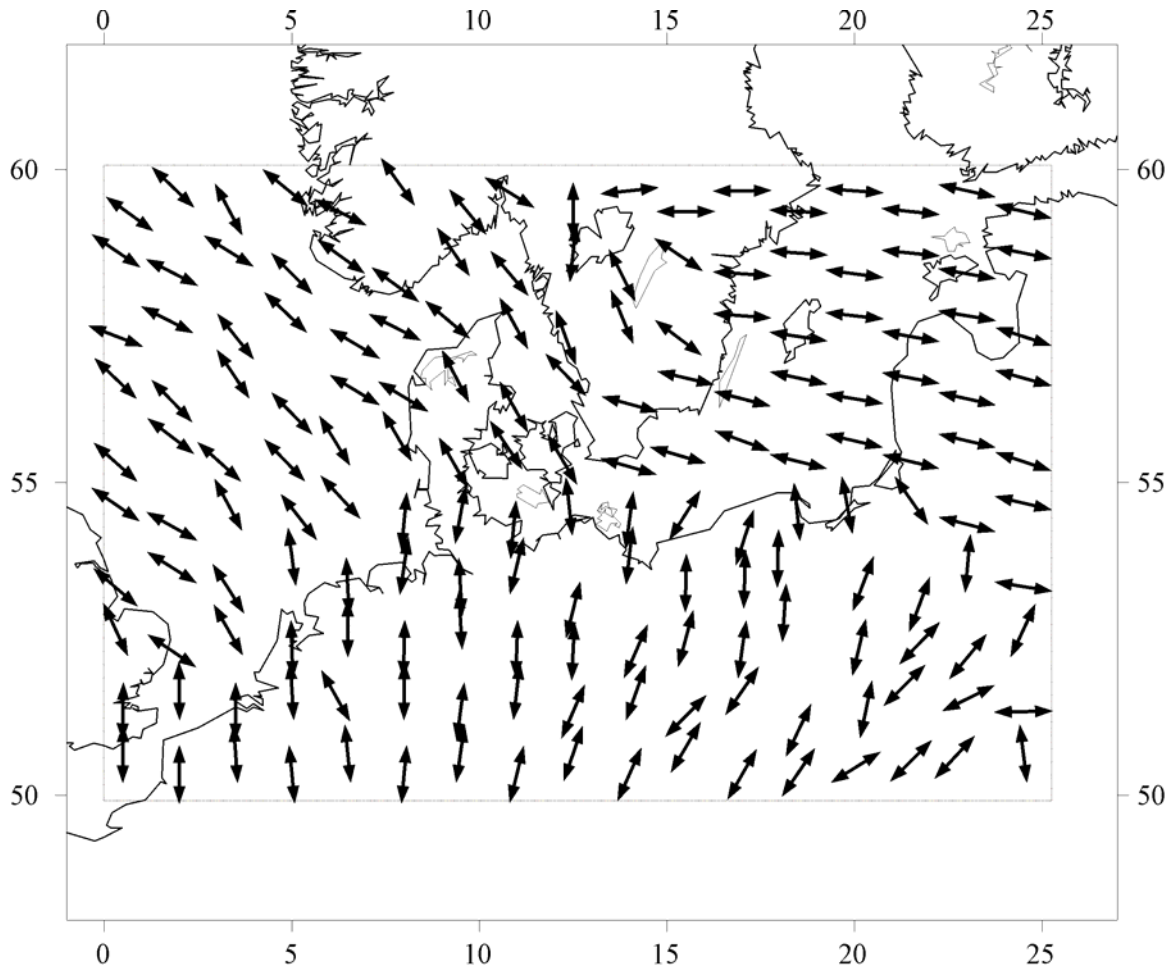


Figure 50.  $S_{Hmax}$  direction obtained from the strain rate eigenvalues as shown in Figure 49.

### Case III: the role of lateral rheological contrasts

Both the tectonic models presented above assume a vertically layered but laterally homogeneous rheological structure of the continental lithosphere under the basin system. As already stated above, (Part 2.1), the CEBS is composed of a variety of adjacent lateral lithospheric domains with different tectonic histories. The observed structuration is likely to cause differences in rheology and consequently also in the geodynamic lithospheric properties. The interplay of intraplate stresses and the above described inherited features may have a strong impact on the deformation pattern and stress setting.

Figure 51 illustrates the domains with different rheologies in the lower crust considered in order to reproduce the most relevant lateral heterogeneities as constrained by geophysical data. The subdivision made is consistent with the constraints given by previous large-scale seismic and gravimetric studies which suggest a possible extension of the passive continental margin of Baltica as far south as the Elbe Line, so that comprising the high density lower crust as depicted in Figure 51.

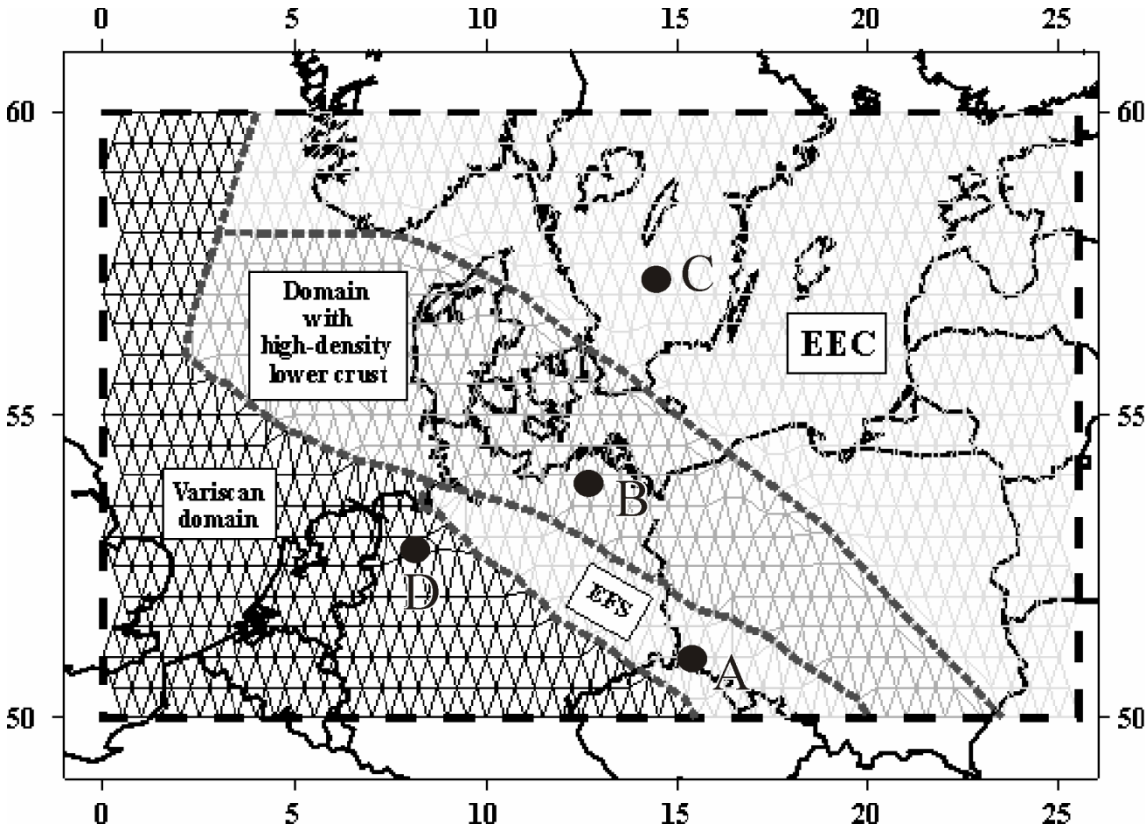


Figure 51. Final 2-D mesh used in the numerical model to investigate the role of inherited lateral structural contrasts under the CEBS. The lateral (sub)domains with different rheological properties in the lower crust are shown. Adopted rheological parameters are given in Table 2.2. Abbreviations: **EFS**=Elbe Fault System; **EEC**=East European Craton. Black dots indicate the locations of the strength profiles shown in Figure 52.

Consequently, the most important boundary in physical properties is modelled along the Elbe Line between a weak and stress sensitive lower crust under the Elbe Fault System (EFS of Figure 51) and a relative denser and stronger lower crust north of the Elbe Line. Thermal and rheological parameters adopted for the different lower crustal domains are summarized in Table 2.3 and Table 2.4.

The range of P-wave lower crustal velocities ( $6.2-6.5 \text{ km s}^{-1}$ ) and densities ( $2700-2800 \text{ kg m}^{-3}$ ) observed in the area along the Elbe Fault System motivate a granitic to a granodioritic composition. The high values for P-wave velocities reaching  $6.9-7.0 \text{ km s}^{-1}$  and the range of

densities (2900-3100 kg m<sup>-3</sup>) in the lower crust north of the Elbe River and below the Sudetes in Poland suggest a lithology typical for gabbros. However, the same area is characterized by a massive presence of granulites. These granulites are mingled with other petrographical rock types (e.g. amphibolites, granites and gabbros) and present relative high metamorphism. Following these observations, this area is modelled with a felsic-granulite composition. To the north this felsic-granulite lower crust is bounded by the Tornquist Zone. For the Baltic region a slightly stronger mafic-granulite rheology is used. For the area southwest of the Elbe Fault System, representing typical Variscan continental crust, a quartzite dominated composition is considered.

<b>Type of rocks</b>	$\dot{\epsilon}_0$ (MPa <sup>-n</sup> s <sup>-1</sup> )	E (KJmol <sup>-1</sup> )	n
Granite (dry)	1.8 10 <sup>-9</sup>	335	3.2
Quartzite (dry)	6.7 10 <sup>-6</sup>	156	2.4
felsic Granulite (dry)	8.0 10 <sup>-3</sup>	243	3.1
mafic Granulite (dry)	1.4 10 <sup>4</sup>	445	4.2

**Table 2.3.** Creep parameters of crustal material used in the modelling study (from compilations by Ranalli, 1995; Chopra & Paterson, 1981; Kirby, 1983; Kirby & Kronenberg, 1987; Ranalli & Murphy, 1987, Ji & Zhao, 1993; Wilks & Carter, 1990).

<b>Layer</b>	<b>Lateral subdivision</b>	<b>Dominant rheologies</b>
sediments	None	See Table 2.1
upper crust	None	Quartzite
lower crust	Variscan domain	Quartzite
	High density body	felsic Granulite
	EFS	Granite
	EEC	mafic Granulite
mantle	None	Olivine

Table 2.4. Rheological properties adopted for each lateral and vertical domain. See **Table 2.2** and **Table 2.1** for the respective creep parameters.

The modelling approach incorporates simultaneously the effects of lateral variations of rheology determined by crustal and mantle thickness variations and associated variations in the thermal regime and the subordinate effects arising from lateral density contrasts in the lower crust. Consequently, it is not possible to discern clearly their relative importance. However, previous models (e.g. Sonder & England, 1989; Cianetti et al., 2001), have demonstrated that buoyancy forces arising from density contrasts have only a secondary effect with respect to the temperature dependence of the rheology.

Figure 52 shows effective strength profiles at four different locations as indicated by the black dots in Figure 51. Profile A is located within the Elbe Fault System, profile B within the high density lower crustal domain north of the Elbe Line, profile C is located within the Baltic domain and profile D in the Variscan domain.

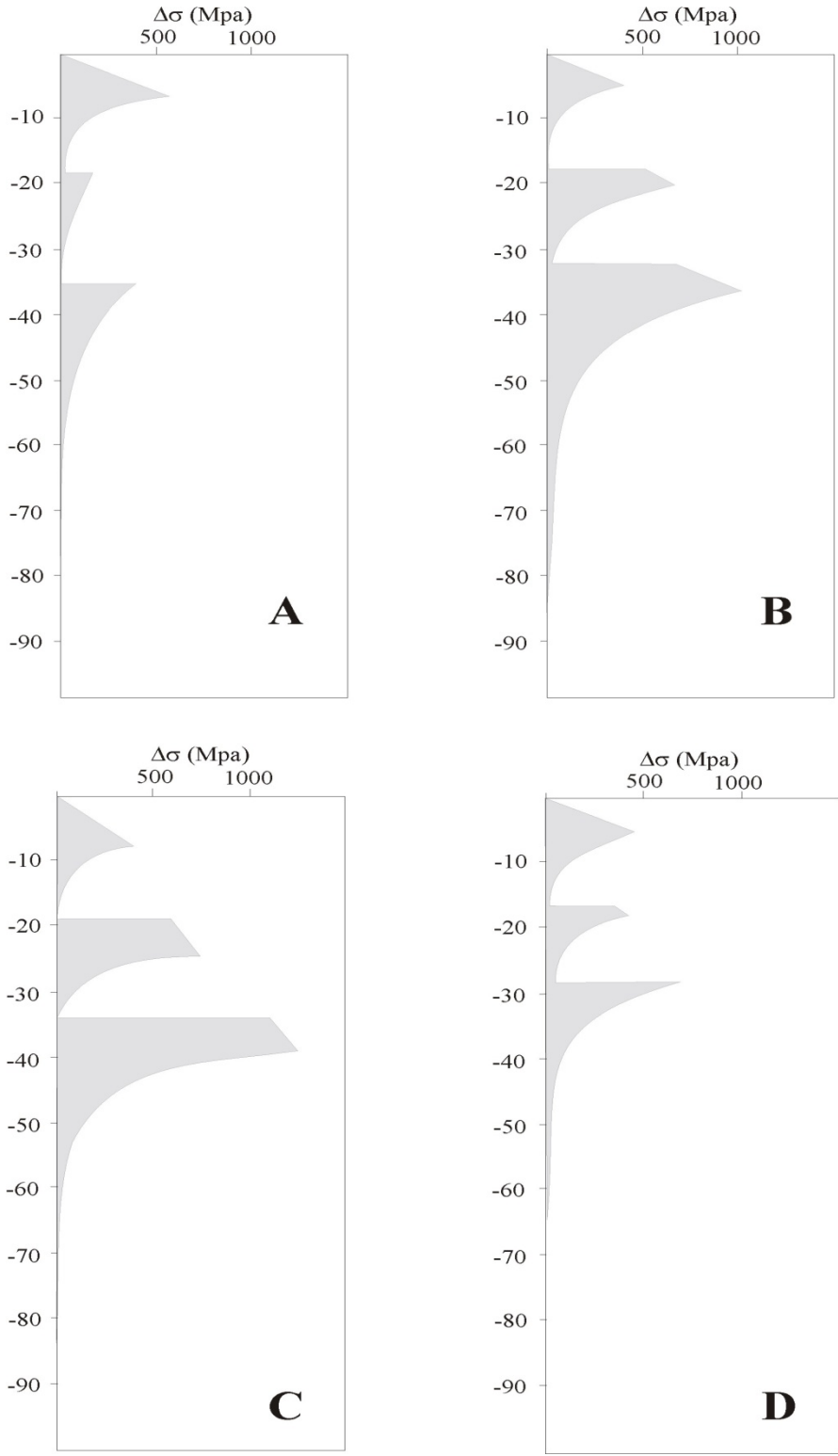


Figure 52. Example of strength profiles at different locations for the Case III.

Characteristic for all profiles is a strength increase with depth at shallow levels, i.e. frictional domain. Reaching deeper levels, the strength decreases due to higher temperatures and stress released caused by viscous deformation. At the upper-to-lower crust transition a strength increase occurs due to the presence of stronger material in the lower crust. Similarly, at the Moho transition a significant strength increase occurs due to the presence of relative stronger mantle material. Comparing the strength profiles shows that the strength of the upper (brittle) portion of the mantle is higher for profiles B and C due to the presence of a deeper asthenosphere-lithosphere level. Increased lower crustal strength in profiles B and C may be directly related to the strong lower crust under these areas. On the contrary, the weak lower crust under the Elbe Fault System reduces crustal strength significantly under this area, see profile A. Figure 53 illustrates the resulting horizontal strain rates. The model results resemble geodetic observations as well as local differences in the deformation pattern.

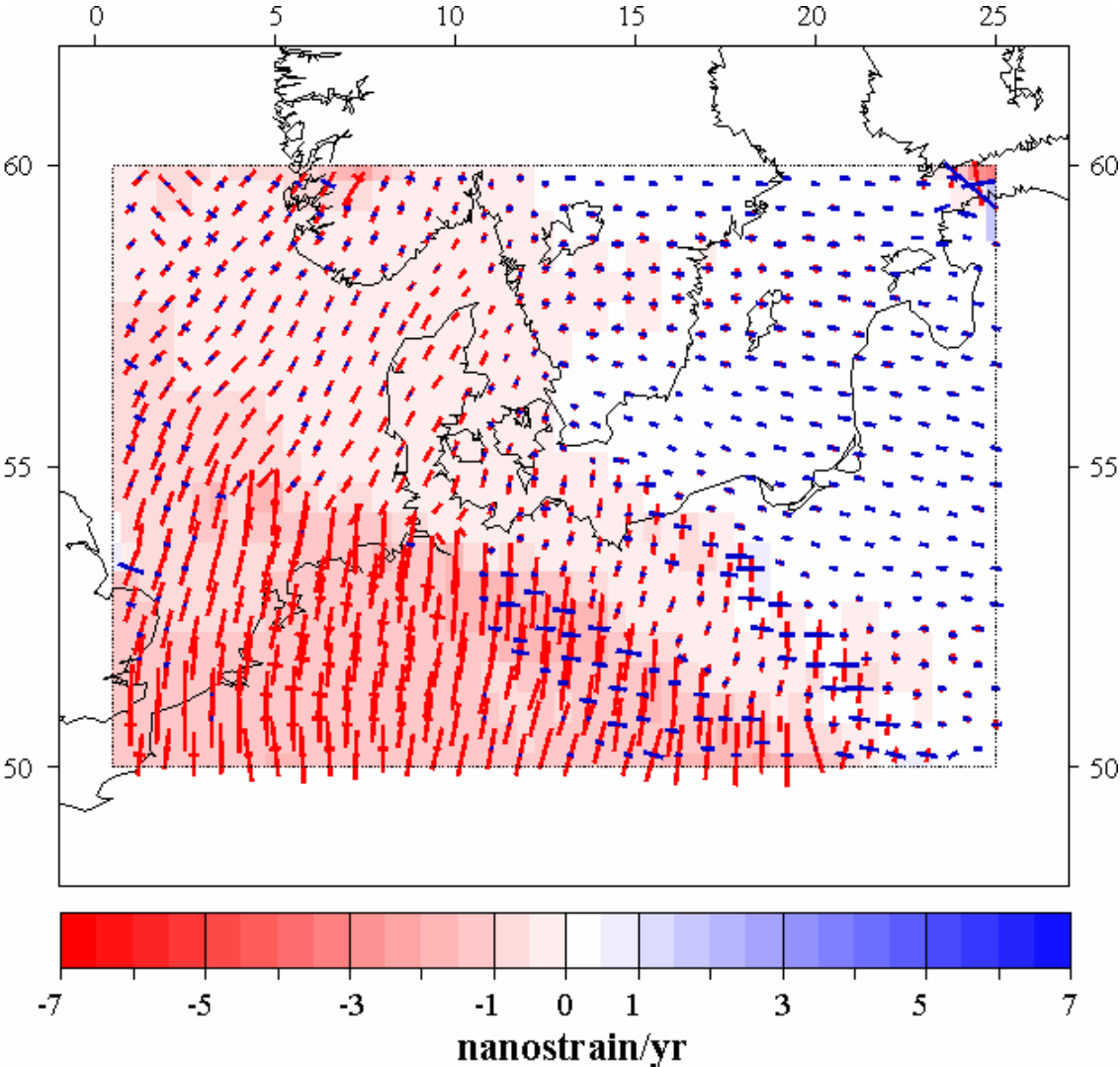


Figure 53. Horizontal strain rate eigenvalues (background colour map) and eigenvectors (hyphens) obtained from modelling the observed lateral rheological lower crustal heterogeneities as shown in Figure 51.

The deformation style correlates with the distribution of lower crustal properties. Indeed, the main feature is a southward shift of the zone of strain localization, compare Figure 49 with Figure 53. Now, the area with highest deformations is found along the Elbe Fault System, while minor compression is still visible along the Teisseyre-Tornquist Zone. This change in horizontal deformation may indicate that the high density and stronger lower crust north of the Elbe Line reduces the amount of deformation when the lithosphere is subjected to intraplate deviatoric stresses. Moreover, the strong rheological contrast between the regions south and north of the Elbe Line results in strong strength gradients. These gradients result in less efficient strain transfer within the weakest part (i.e. Elbe Fault System) explaining the lack of intraplate deformation under the North East German Basin. On the contrary, the mechanically weak lower crust under the Elbe Fault System induces the observed strain localization. N-S to NNE-SSW-oriented compression is stronger in the weaker crust below the EFS compared to the northern part where the predicted strain rate pattern indicates low deformation rates. The modelled kinematic setting suggests the presence of a stiff and rather undeformable crustal domain in the north-easternmost part of the North German Basin. The presence of a stronger crustal body beneath the basin is a feature that has been already demonstrated by previous rheological models (e.g. Marotta et al., 2002). At the same time, it may explain the observed a-seismicity of the area (e.g. Cloetingh et al., 2006).

Under the Polish Trough a southward shift in the location of strain localization occurred with respect to the previous case. Now deformation is mainly localized south to the NW-SE-trending axis of the Permian basin whereas minor compressional deformation occurs along the Tornquist Zone. This feature results in less activity under the already stabilized basin in consistence with the present-day setting.

Following the results of Figure 53, strong strain localization may occur in the continental lithosphere without considering external artificial model devices in the numerical formulation (e.g. predefined faults and long shear viscous zones). In contrasts, continental deformation is strongly localized by the presence of thermal, mechanical and compositional heterogeneities at different depth levels in the lithosphere. The present-day lateral rheological variations in the lithospheric configuration constrained by geophysical data, may drive continental deformation and explain processes including strain localization. This can finally lead to failure and possible formations of major fault zones. Consequently, at large scales, faults should be considered more likely as structural consequences of the heterogeneous composition of the lithosphere thus playing a secondary role in the evolution of complex basins with respect to pre-existing structural and thermal contrasts.

To better constrain the model outcomes the predicted orientation of the principal horizontal compressive stress is shown in Figure 54.

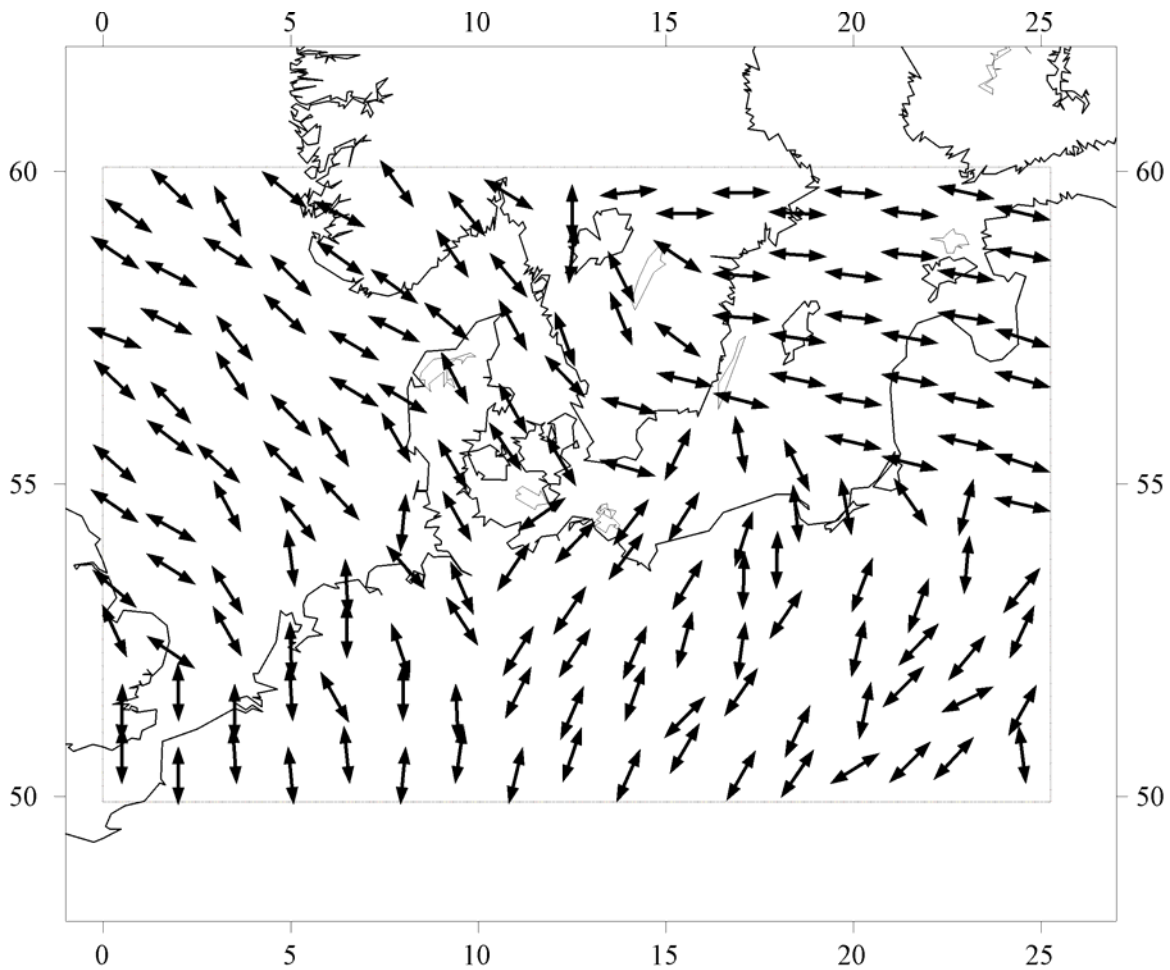


Figure 54.  $S_{Hmax}$  direction obtained from the strain rate eigenvalues of Figure 53.

The modelled stress field is in agreement with the present-day stress pattern observed in North and Central Europe (Zoback 1992; Reinecker et al. 2005). In contrast with previous modelling studies (e.g. Golke & Coblenz, 1996), the results of Figure 54 demonstrate that the direction of the principal stress axes is not totally independent of the adopted rheology of the lithosphere. Stress rotations up to  $45^\circ$  occur along the boundaries between the domains with different rheologies thus resembling the observed local bending in the direction of the largest horizontal stress component. The consistent NW-SE-orientated compression gradually bends to a N-S- to NE-SW-directed  $S_{Hmax}$  under northeastern Germany and Poland. This anomalous stress pattern is due to the interplay of lateral variations in the thermal field and the thickness of the different structural layers together with the presence of lateral rheological contrasts in

the lithosphere. The presence of different structural domains at both crustal and shallow mantle level is responsible for the observed local variations in the direction of the regional stress field. Accordingly, more drastic stress deflections are visible inside and across the boundaries of the weak crustal domain associated with the Elbe Fault System. This effect arises from the contrasting rheologies modelled between the Elbe Fault System and the surrounding areas.

### **2.3 Geodynamic modelling of the Mesozoic evolution of the CEBS**

The remaining of the chapter attempts a reconstruction of the first-order kinematic and dynamic history of the basin system since its formation in Late Carboniferous-Early Permian.

The main goals are:

- i. To elucidate and quantify the relevance of pre-existing inherited structures within the lithosphere in controlling continental deformation patterns during different tectonic pulses.
- ii. To understand to which extent variations, even small, in the regional stress regime and/or direction can interact with the observed variations in the lithospheric structure and to which degree these interactions can affect the character of basin development.

The results obtained for the present-day tectonic state (Part 2.2) have demonstrated the importance of inherited crustal and deeper shallow mantle structures in controlling the stress and strain state for the basin system including processes like strain localization and stress bending. Based on these results, in the present part of the study the evolution of major subsidence centres and adjacent areas of uplift through time is reconstructed in relation to small changes in the effective stress boundary conditions together with regional variations in the lithospheric structure. All boundary conditions are adopted to fit the observed regional deformation patterns and as far as possible the general knowledge about the (palaeo)stress fields. The main sources we relied on are: (a) the tectonic models developed in Stampfli et al. (2001), Ziegler & Stampfli (2001), and Ziegler et al. (2001) for the tectonic evolution of the western Tethys and PeryTethyan domains, (b) the plate-tectonic reconstructions made by Mosar et al. (2002) and Torsvik et al. (2001) for the North-Atlantic area, (c) the studies of Nikishin et al. (1996) for the evolution of the East European Craton and (d) Scheck-Wenderoth et al. (in press) for the Permian to Cretaceous evolution of Central Europe.

Horizontal deformation velocities and intra-plate stresses as obtained along the natural plate boundaries are then scaled to match the geometry of the integral mesh used for numerical simulations. A trial-and-error approach is adopted to select those boundary conditions which guarantee an acceptable tectonic scenario and a best fit with the observed deformations and stress fields. The main question the models address is to gain insights in the relationship between first order features characterizing the kinematic setting of the CEBS throughout its tectonic evolution and the observed changes of geodynamic forces along the natural boundaries of the European plate. In this regard, the models do not provide an exhaustive survey of the evolution through time of sedimentary and crustal distributions and present some unavoidable limitations regarding thermal and structural palaeoconditions. This is mainly due to the lack of suitable geological databases for the entire basin system. Indeed, the models are intended to study and demonstrate a number of more generic aspects in the large-scale kinematics and dynamics which may have been relevant, if not prominent, during the long and multiphase tectonic evolution of the CEBS.

### **Late Carboniferous-Permian**

The destabilized palaeotectonic setting of the CEBS prior to the subsidence initiation in late Early Permian was marked by the development of a mega-shear fault system that developed as an intra-continental diffuse plate boundary between the African-western PalaeoTethys segment of Gondwana and Europe (Ziegler, 1990). This shear-fault system is thought to have controlled the subsidence history during Permian times in the basin system. The major element of this shear fault system within the domain of the CEBS is represented by the continental-scale dextral shear Teisseyre-Sorgenfrei Tornquist Zone.

Figure 55 illustrates the boundary conditions adopted to investigate the relationship between the post Variscan Permo-Carboniferous wrench tectonics and the subsequent 'syn-rift' subsidence observed in the CEBS. Displacement boundary conditions along the western border of the study area agree with dextral strike-slip movements observed along the elements of the Great Glan fault in western Britain as well as across the elements of the Tornquist Fan (e.g. Ziegler, 1990; Thybo, 1997). The relative NE-directed velocity components on the northern boundary are related to contemporaneous reactivation of the Permo-Carboniferous Artic-North Atlantic Rift System and its southward propagation in the north-easternmost part of the North Sea domain. *SW-oriented velocity* vectors along the southern border reflect the development of the new Tethys Rift System along the southern border of the basin system.

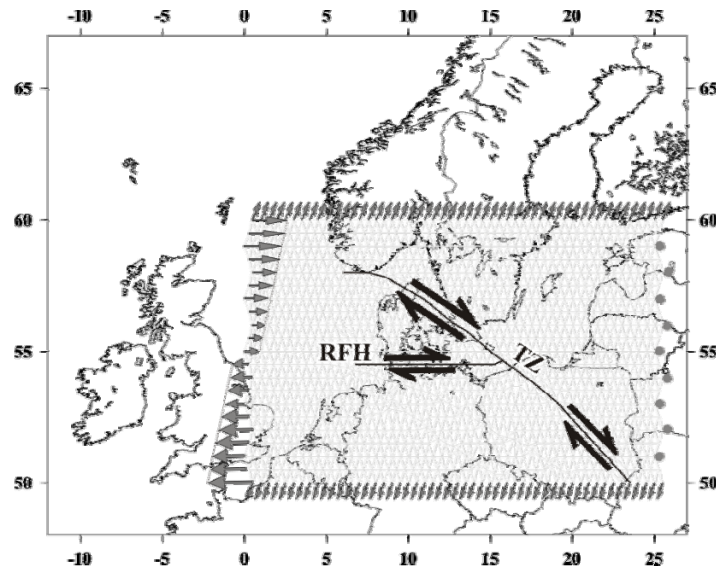


Figure 55. Adopted boundary conditions (thin grey arrows) to model the Permo-Carboniferous evolutionary phase of the CEBS. The adopted boundary conditions are chosen to impose dextral transtensional movements along the elements of the Tornquist Fan (i.e. Teisseyre-Tornquist Zone=**TZ** and the Ringkøbing Fyn High=**RFH**) as depicted by the thick black arrows.

To account for ongoing subduction in the Urals (e.g. Scheck et al., in press), a fixed, i.e. shear stress free, surface boundary condition is adopted along the eastern border as shown by the light grey dots of Figure 55.

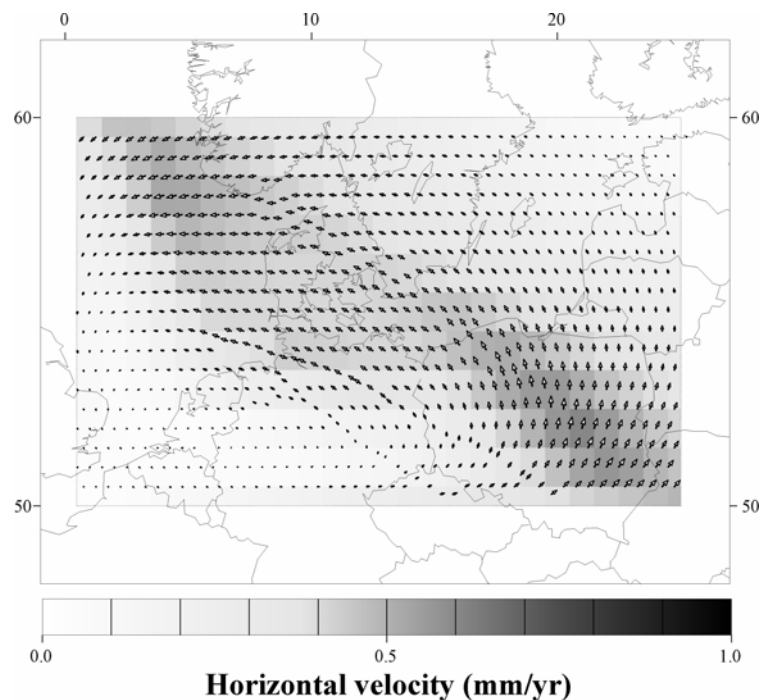


Figure 56. Horizontal deformation velocity field obtained for the Early-to-Late Permian evolutionary phase of the CEBS.

Driven by the adopted boundary conditions of Figure 55, the horizontal deformation velocity field of Figure 56, shows a concentration of tectonic activity within the area extending between the Ringkøbing-Fyn-High in the south and the Sorgenfrei-Tornquist Zone in the north. Velocity vectors orientate in a consistent way to impose dextral transtensional movements along the elements of the ‘Tornquist Fan’, e.g. Thybo (1997). Local increase in magnitudes of horizontal velocity vectors are found across the southward lineament of the Tornquist Zone in Poland. The modelled velocity field is in agreement with the observed local differential subsidence of the permian basin (e.g. Dadlez et al., 1995).

In Figure 57 the results in terms of horizontal strain rate eigenvectors and eigenvalues are shown.

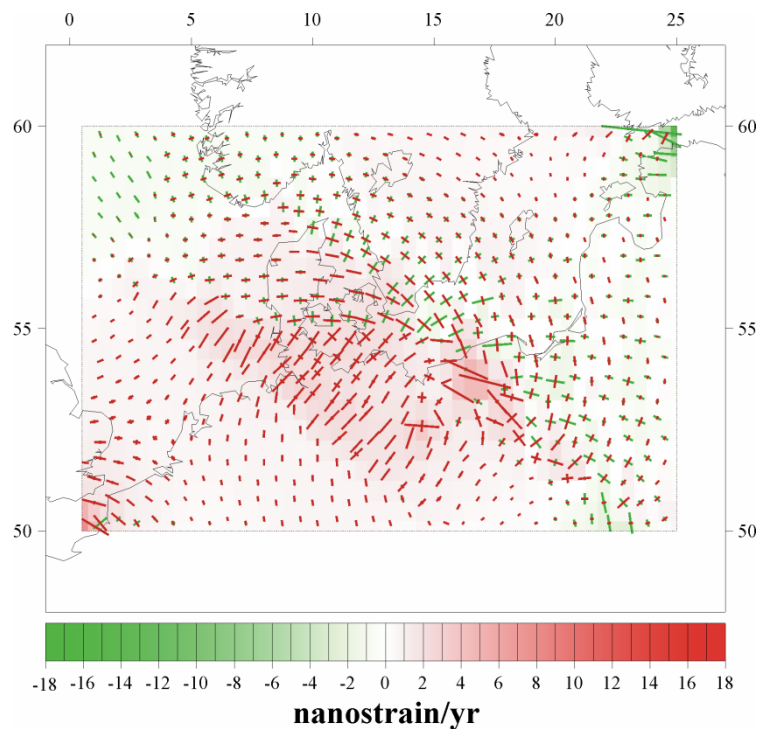


Figure 57. Horizontal strain rate eigenvectors (hyphens) and eigenvalues (background colour map) as obtained from the velocity results of Figure 56. Green colours refer to horizontal compression and red colours to horizontal extension.

The kinematic setting depicted is in consistence with the horizontal deformation velocity results of Figure 56. A concentration of horizontal deformation (mainly extension) occurs under the area of increased values of the deformation velocity field. Extension (red colours) occurs along the Teisseyre branch of the Tornquist Zone in Poland where the strain rate vectors follow the NW-SE-striking geometry of the geological structure. A gradual anticlockwise bending in the orientation of the horizontal strain rate vectors occurs along the

northern branch of the Tornquist Zone, under Denmark and in the easternmost North Sea. The observed deviation reflects a gradual change in the deformation style. N-S-oriented compression (green coloured arrows) gradually becomes comparable to E-W extension (red coloured arrows). Additional areas of localized extensional deformation are visible more to the south of the Ringkøbing-Fyn-High across the westernmost part of the North German Basin, onshore and offshore northern Germany, as well as under the Elbe Fault System domain. A change in the orientation of strain rate vectors pointing ENE-WSW to EN-WS is also visible under these domains.

In Figure 58 the results in terms of the orientation of the maximum horizontal stress component  $S_{Hmax}$  and the related fault regime (different colours) are shown.

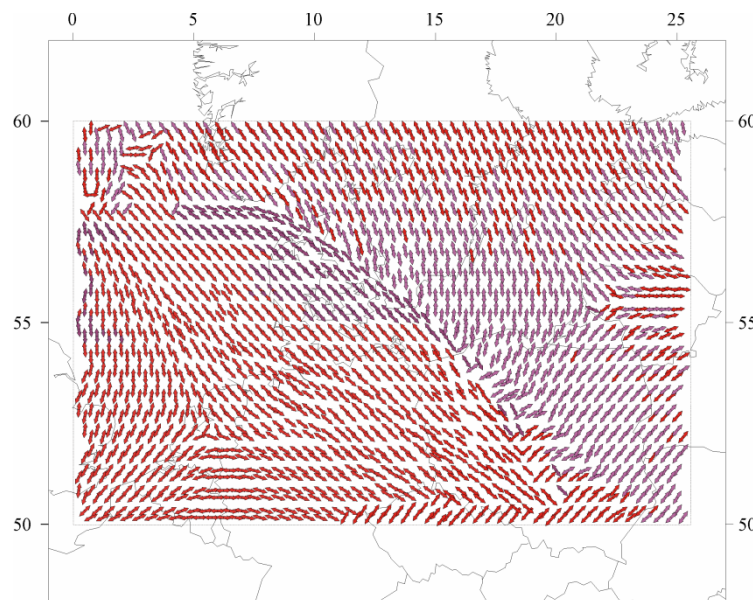


Figure 58.  $S_{Hmax}$  orientation (arrows direction) and associated stress regime (arrows colour). Red coloured arrows indicate an extensional stress regime while purple coloured arrows indicate a transtensional stress regime.

NW-SE-oriented extension dominates the southern domain of the study area. A change in the  $S_{Hmax}$  orientation is visible along the Tornquist Zone where large stress rotations (up to  $45^\circ$ ) indicate a classical strike-slip fault pattern which is consistent with a transtensional rejuvenation of the same structure. Accordingly, purple coloured arrows standing for transtensional stresses confirm a change in the stress regime across the Tornquist Zone.

Figure 59 shows the observed subsidence pattern for the Early- to Late Permian times in the area of the CEBS. The main depocentres of subsidence were restricted to the WNW-ESE-trending Southern Permian Basin and Northern Permian Basin. Direct connection between the two basins was impeded at that time by the presence of the Ringkøbing Fyn High trends of

highs. Post-rift thermal subsidence commenced earlier (late Early Permian) and was more intensive in the Southern Permian Basin than in the Northern Permian Basin where the late Early Permian cover is thinner and considerable post-rift subsidence was observed in Zechstein times (e.g. Vejbaek, 1997).

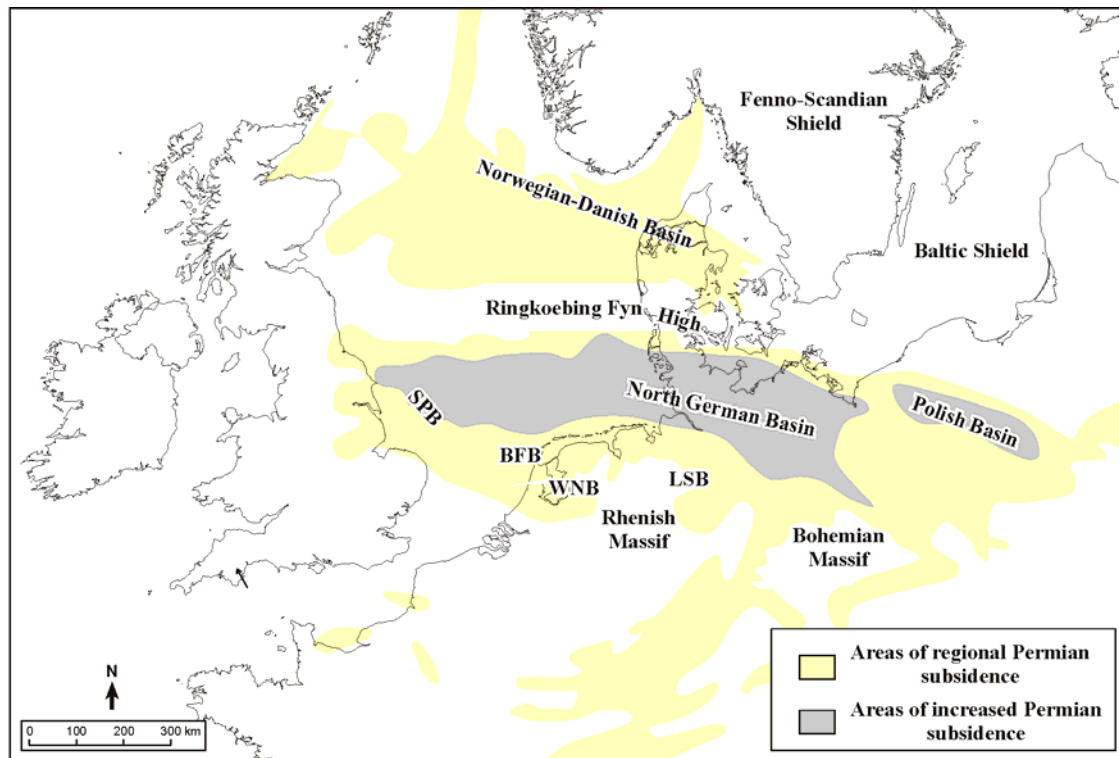


Figure 59. Observed subsidence pattern for the Permo-Carboniferous evolutionary phase of the CEBS, modified after Evans et al. (2003); Lokhorst (1998). Light yellow colours frame the areas which underwent regional subsidence. Grey areas enlighten the main depocentres of subsidence. Abbreviations: **BFB**=Broad Fourteen Basin; **LSB**=Lower Saxony Basin; **WNB**=West Netherlands Basin.

In Figure 60 the model results in terms of effective strain rates (i.e. rate of crustal thinning/thickening) are presented. The broad pattern of vertical deformation is resembled. Subsidence, blue coloured areas, occurs along the Southern and Northern Permian basins with the former showing higher amounts of vertical displacement. These two subsiding areas are clearly detached by the presence of a domain (i.e. Ringkøbing-Fyn-High) of no vertical deformation.

Moving to the North German-Southern North Sea Permian Basin, the results well image the local geometry of the observed subsidence. The modelled subsidence pattern resembles the observed asymmetrical geometrical configuration consisting of a broad WNW-ESE-trending sag-like domain characterized by a steeper flank in the north-northwest part of the basin and a

gentler one along the southeastern flank (e.g. Bachmann & Hoffmann, 1997; Scheck-Wenderoth & Bayer, 1999). Most of the Permian subsidence is oriented NW-SE presenting a typical bull-head structure with its depocentre in the northwestern part (e.g. Scheck-Wenderoth & Bayer, 1999).

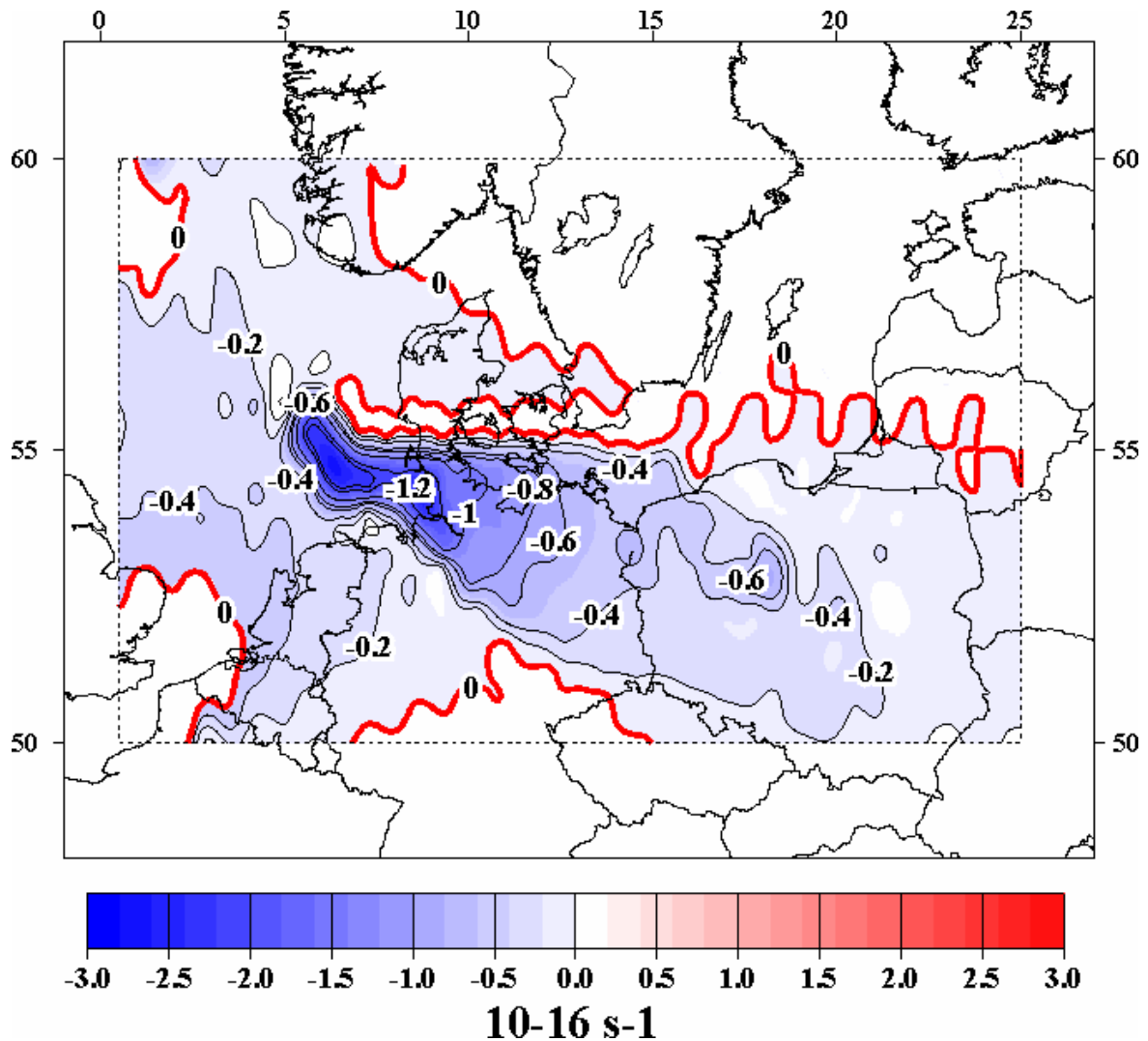


Figure 60. Effective strain rate (=crustal thinning/thickening rates) results for the Early-to-Late Permian evolution of the CEBS. Blue colours-negative values indicate subsidence. Thick red isolines border the region of no vertical deformation.

The modelled subsidence under the Polish Trough presents a more linear NW-SE-striking structure which is superimposed on the Teisseyre-Tornquist Zone (e.g. Dadlez, 1989; Lockhorst, 1998; Scheck-Wenderoth & Lamarche, 2005). The stress results of Figure 58 confirm the presence of localized extensional/transensional stresses along the south-western border of the East European Craton. This feature is in agreement with previous models (e.g. Stephenson et al., 2003; Dadlez et al., 1995) and structural studies (e.g. Van Wees et al.,

2000; Lamarche et al., 2003). The modelled stress concentration along the weak domain of the Teisseyre-Tornquist Zone can explain the initial subsidence stage of the basin.

### Early Triassic to Early Jurassic

The global tectonic setting which characterized the Triassic-to-Early Jurassic evolutionary phase of the CEBS led to the development of a complex and multidirectional rift system which interacted with the continuously subsiding Northern and Southern Permian Basins. The major elements of this rift system comprise: the Norwegian-Danish Basin and the Mid North Sea Central Graben in the area of the North Sea domain, and the North German Basin and the Polish trough in the southern part of the CEBS.

Figure 61 shows the adopted boundary condition to model the observed tectonics.

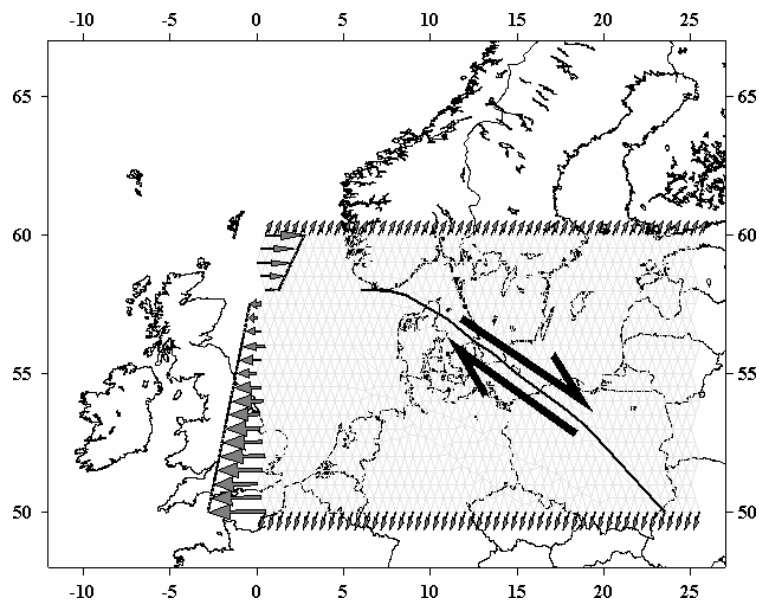


Figure 61. Adopted boundary conditions for the Triassic-Early Jurassic evolutionary phase of the CEBS. See text for explanation.

Velocity vectors along the northern model boundaries reflect the observed ongoing subsidence of the Arctic-North Atlantic as well as rifting in the East Greenland-Norwegian Sea Rift System in the domain of the north and central North Sea. The boundary condition along the western border of the study domain accounts for the observed westward propagation of NeoTethys sea-floor spreading axis and accelerated crustal extension in the Central Atlantic (Stampfli & Borel, 2002). Continuous northward subduction of the PalaeoTethys is modelled by SW-orientated velocity vectors along the southern model boundary grading towards the east into a free surface boundary condition along the eastern margin.

In Figure 62 the modelled deformation horizontal velocity field is shown. The kinematic setting of Figure 62 supports southeast-to-northwest movements along the Tornquist Zone. In contrast to the Permian stage, displacements vectors are fully accommodated along the two branches of the Sorgenfrei- and Teisseyre-Tornquist Zone in a single fault zone with no dispersion over a broader area.

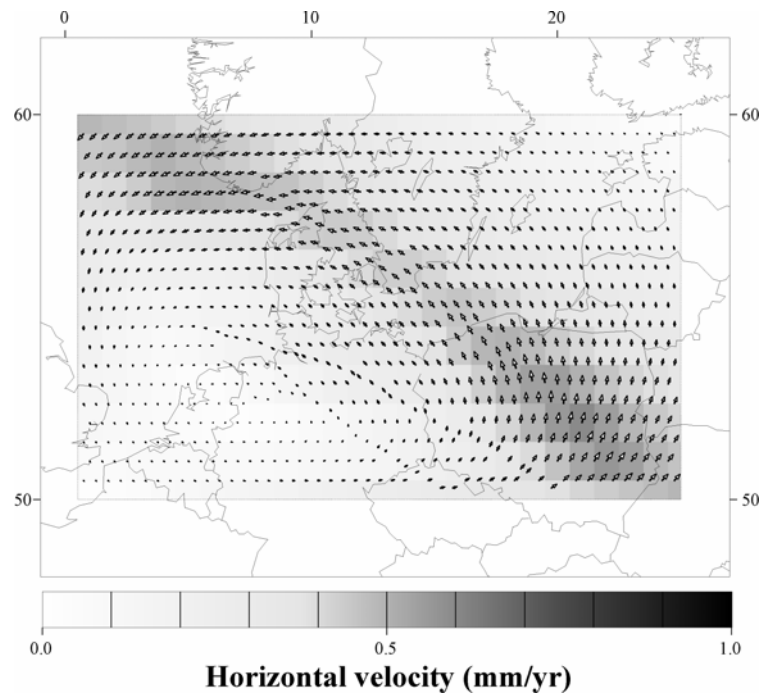


Figure 62. Horizontal deformation velocity field as obtained from the boundary conditions illustrated in Figure 61.

Figure 63 illustrates the calculated horizontal strain rate eigenvectors and eigenvalues. In consistence with the deformation velocity field of Figure 62, horizontal deformation (extension) is localized along the structural lineament of the Tornquist Zone. The local increase in the magnitudes of the horizontal strain rate tensor along the Polish branch of this structure indicates a concentration of tectonic activity beneath this area. This feature well correlates with the observed accelerated subsidence under the NW-SE-oriented axes of the Polish Trough (e.g. Dadlez et al., 1998; Dadlez, 2003).

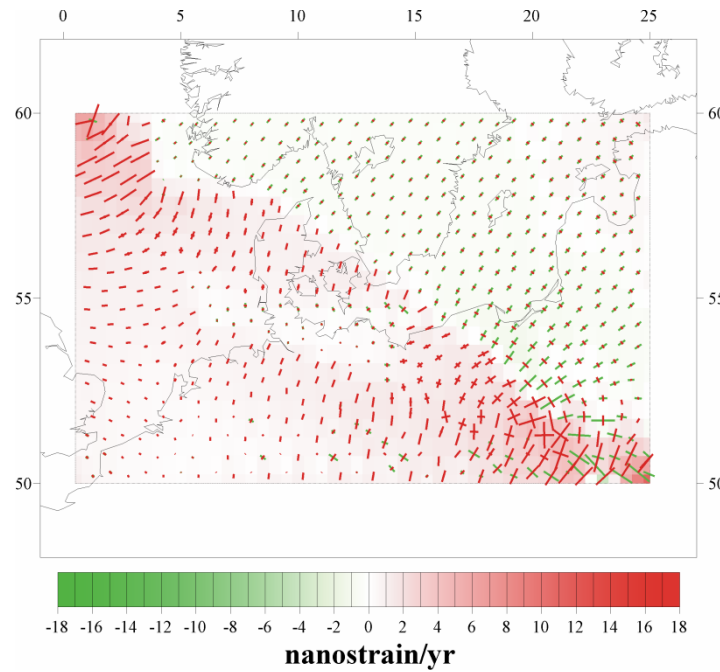


Figure 63. Horizontal strain rate eigenvectors (coloured hyphens) and eigenvalues (background colour map) calculated from the velocity results of Figure 62. Red colours indicate extension and green colours compression.

In Figure 64 the stress field results are shown.

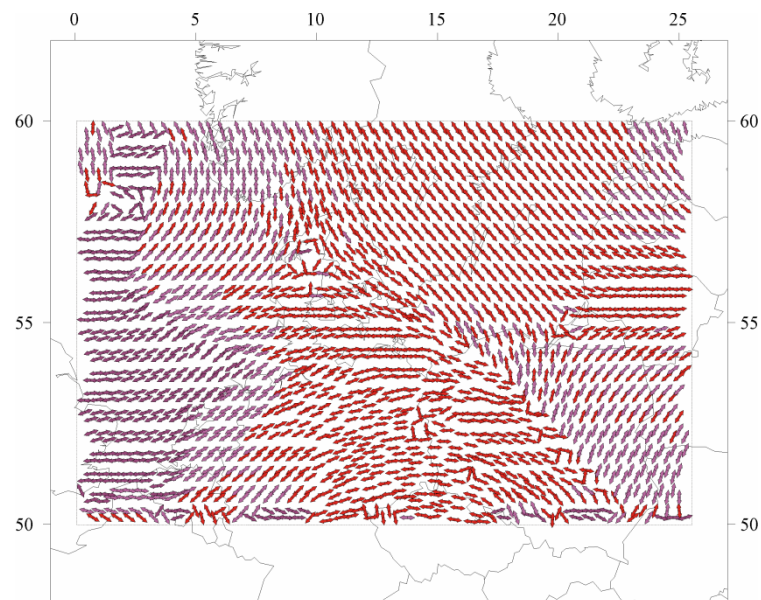


Figure 64.  $S_{Hmax}$  orientation and associated stress regime as derived from the velocity vectors of Figure 62. Red coloured arrows indicate thrust fault regime, and purple coloured arrows strike-slip (transtensional) regime.

A region of E-W-oriented extension marks the area of the North German Basin and Danish Basin. The modelled stress field is in agreement with paleaostress reconstruction stating E-W-oriented extension in the Early-to-Late Triassic suggested by the development of N-S-

trending graben structures dissecting the Ringkøbing-Fyn High (i.e. Central, Horn and Glückstadt grabens). Far to the east, an anticlockwise stress bending up to 45° occurs along the Tornquist Zone. Here, NW-SE stresses indicate southeast-northwest transtensional movements. The active regional stress regime supports tensional reactivations of the Permo-Carboniferous structures as represented by the Teisseyre-Tornquist Zone in Poland and by its northern prolongation in the area of the Danish Basin, i.e. Sorgenfrei-Tornquist Zone.

Figure 65 illustrates the thickness distribution of preserved deposits in the basin system (modified after Maystrenko et al., 2006). Triassic-Early Jurassic subsidence follows the regional pattern already established in the Permian with a gradual overstepping with time of the previous basin margins. The regional E-W-oriented extensional stress regime causes the observed locally increased thickness of Triassic deposits in N-S-oriented grabens and troughs (e.g. Central Graben, Horn Graben, Glückstadt Graben, Rheinsberg Trough). Extensional reactivation of the Teisseyre-Tornquist Zone is reflected by the persisting NW-SE-trending subsidence axis of the Polish Basin in Figure 65.

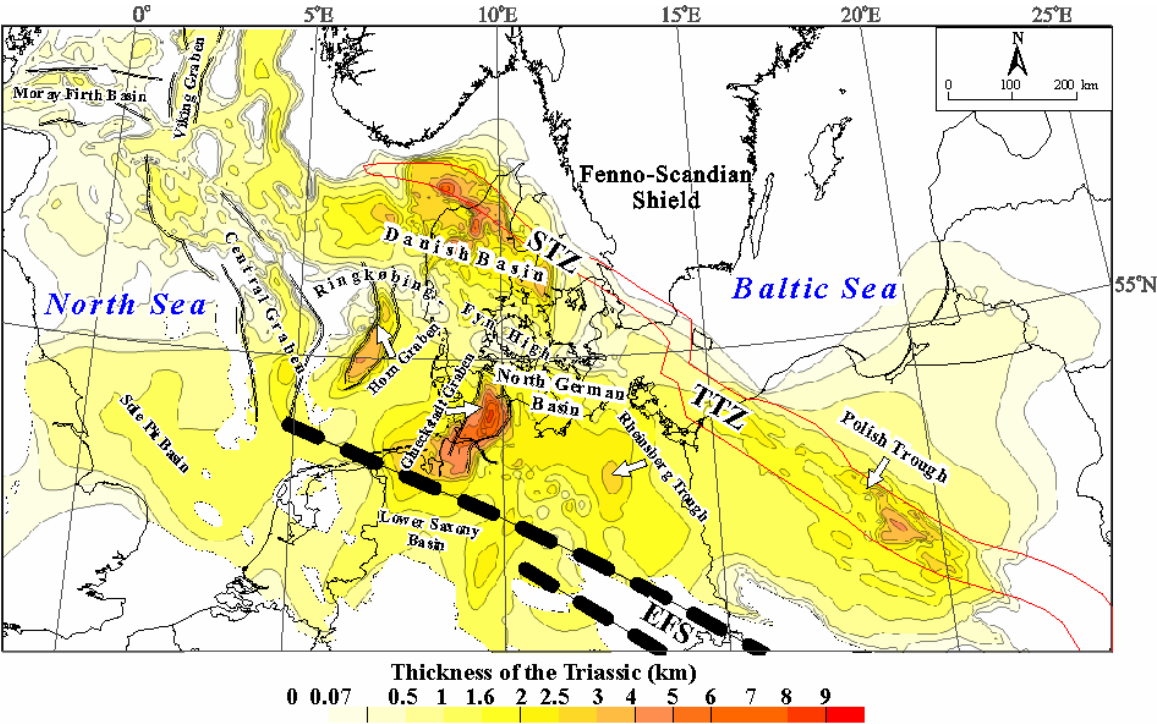


Figure 65. Thickness map of the Triassic deposits in the CEBS, modified after Maystrenko et al. (2006). Increased thickness is found mainly under N-S-oriented grabens and troughs as well as under the NW-SE-trending axes of the Polish Trough. Abbreviations: EFS=Elbe Fault System; TTZ=Teisseyre-Tornquist Zone; STZ=Sorgenfrei-Tornquist Zone.

In Figure 66 the results in terms of effective strain rates are shown.

The overall scenario of uninterrupted subsidence in the area of the main Permian basins is imaged. Subsidence occurred over a wider area with respect to the previous phase, compare Figure 60 and Figure 66. At the same time a progressive overstepping of the basin margins established in the Late Permian is also reproduced. This feature is reflected by the achievement of a full connection between the Northern and Southern Permian basins and the consequent formation of a domain of regional subsidence which extends from southern Poland to the northern North Sea (e.g. Ziegler, 1990).

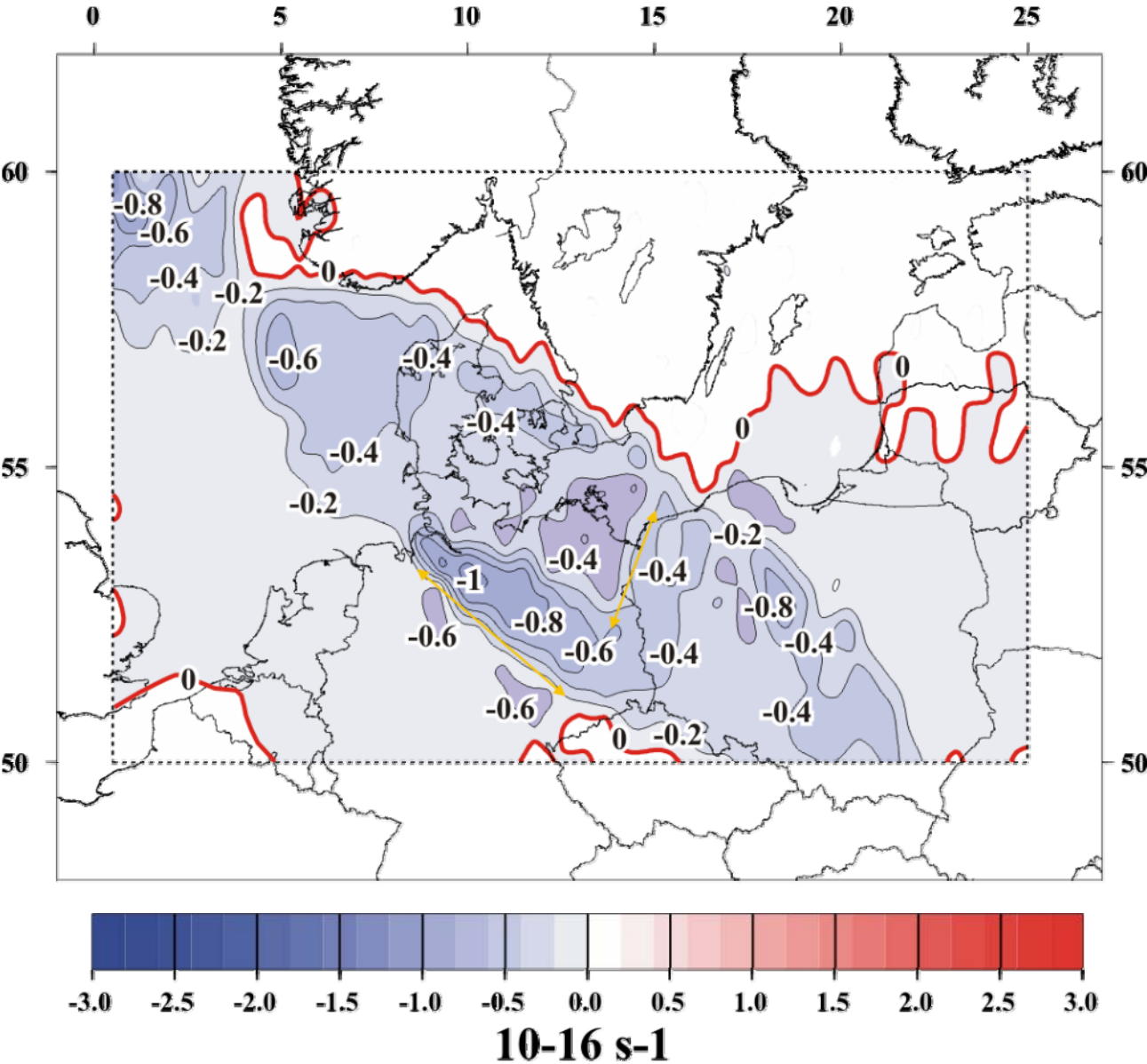


Figure 66. Effective strain rate results for the Early Triassic-to-Early Jurassic stage. Blue colours-negative values indicate crustal thinning (subsidence).

Ongoing subsidence is reported from the North German Basin where sedimentation was continuous since Early Triassic to late Middle-early Late Triassic (e.g. Scheck-Wenderoth & Bayer, 1999; Kossow & Krawczyk, 2002; Scheck-Wenderoth et al., 2003; Maystrenko et al., 2006), from the Polish Trough with maxima rates of sedimentation during the Early Triassic (e.g. Dadlez, 1989, 2003; Krzywiec, 2002, 2006), as well as in the Norwegian-Danish Basin where thermal regional subsidence was interrupted by periods of rapid rift-induced subsidence (e.g. Thybo, 1997; Vejbaek, 1997; Clausen & Pedersen, 1999). Accelerated localized subsidence during the Early-to-Middle Triassic is also reported under newly formed N-S-striking structures, i.e. the Mid North Sea Central Graben, and the Glückstadt Graben, where syn-depositional faulting was triggered by salt mobilization (e.g. Michelsen, 1982; Clausen & Pedersen, 1999; Maystrenko et al., 2006).

*North German Basin.* In the North German Basin, the results of Figure 66 show a change in basin configuration with respect the subsidence pattern of Figure 60. New depocentres now evolve as enlightened by the yellow arrows of Figure 66. The first depocentre shows a NW-SE-oriented axis along the southern margin of the basin. It runs parallel the Elbe Line and shows a linear gradient of accelerated crustal thinning toward the northwestern part of the basin. The second and minor depocentre is located in the eastern domain of the basin aligned along a NNE-SSW-oriented axis. The localization and geometry of the two depocentres result from the interplay of the effective stress field driven by the imposed boundary conditions and the heterogeneous lithospheric structure under the area. The modelled boundary conditions of Figure 61 are consistent with the presence of an (almost) uniform WNW-ESE- to E-W oriented stress regime as shown in Figure 64. This stress field together with the modelled rheological heterogeneities provides sufficient conditions to explain the occurrence of repeated localization of extensional deformation under the stress sensitive weak domain considered under the Elbe Fault System. Accordingly, increased tectonic activity and associated localized deformation are found under this domain thus explaining the observed basin differentiation shown in Figure 66.

*Polish Trough.* The results of Figure 66 image a moderate increase in tectonic activity for the Polish Trough, (e.g. Dadlez et al., 1995; Lamarche & Scheck-Wenderoth, 2005). Based on analysis on the Mesozoic stratigraphic thickness, Dadlez (2003) concluded that the most complete sedimentation under the Polish basin occurred during Early Triassic (Bunter clastics) and Late Triassic (Keuper formation). Accordingly, in Figure 66 the shape of the basin is already delineated with its narrow NW-SE-striking elongated axis, the Mid Polish

Trough. In contrast with the area of the North German Basin where subsidence occurs over a wider area, the modelled subsidence below the Polish Trough shows a more linear, NW-SE-directed, pattern with a local maximum in the middle part of the axis (e.g. Dadlez 2003). A longitudinal propagation of the south-eastern segment of the basin towards south-east is also imaged, e.g. Hakenberg & Swidrowska (1997). A local increase in vertical movement occurs in the central segment of the Basin (e.g. Dadlez et al. 1995).

*Norwegian-Danish Basin.* The tectonic scenario depicted by Figure 64 and Figure 66 is in agreement with previous studies (e.g. Sorensen, 1986; Frederiksen et al., 2001a,b) that have related the observed crustal extension and associated subsidence under the Norwegian-Danish Basin with Triassic to Early Jurassic transtensional movements along the fault systems of the Sorgenfrei-Tornquist Zone. Accordingly, the stress results of Figure 64 indicate mild Triassic lithospheric extension in the area of the Norwegian-Danish Basin. This dynamic setting may have controlled the Triassic subsidence under the Permian basin. The occurrence of areas of differential subsidence in the area of the Fennoscandian Border Zone may be related to the presence of the Sorgenfrei-Tornquist Zone. Due to its location, the Sorgenfrei-Tornquist Zone may be regarded as a natural lithospheric boundary between the relatively cold and stable Baltic domain to the north-east and the more mobile crustal units to the southwest. Under the regional (transtensional) stress field as shown in Figure 64, the Sorgenfrei-Tornquist Zone acts as a 'buffer' between these two domains. This would prevent a release of stresses under the area to the northeast resulting in a concentration of stresses under the weaker domain to the southwest. The described dynamics may explain the rapid differential subsidence modelled in the Fennoscandian Border Zone and offshore Denmark.

### **Middle Jurassic to Early Cretaceous**

Triassic-Early Jurassic subsidence was interrupted during Middle Jurassic by a deep-seated thermal dome below the Mid North Sea High which was centred at the triple junction in the Central North Sea Rift System, i.e. Viking Graben, Moray Firth Basin, and Central Graben. This dome caused in regional uplift of the area of the Central North Sea domain ('Mid Cimmerian unconformity').

Figure 67 summarizes the geometry of the observed deformation. Middle Jurassic uplift was not limited to the North Sea area but extended also across Denmark and to north-western Germany including the Mid North Sea Ringkøbing-Fyn-High, the southern part of the Danish

Basin (e.g. Vejbaek, 1997) and the north-western portion of the North German Basin, i.e. the Pompeckij Block (Jaritz, 1987).

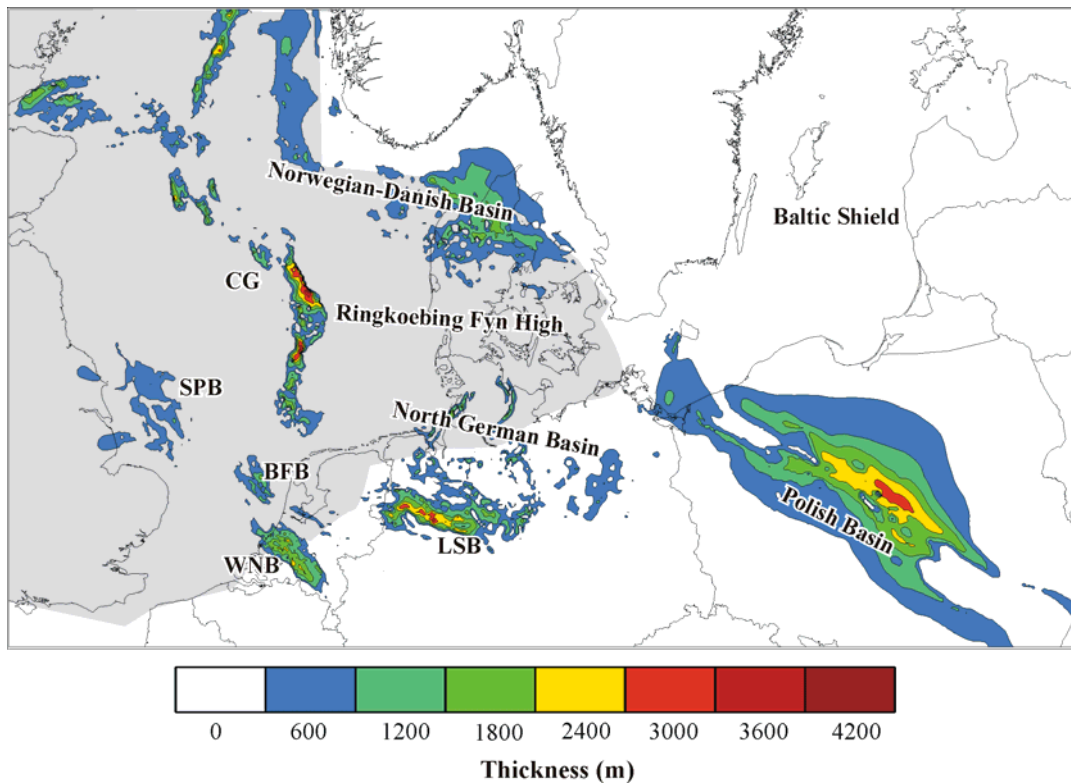


Figure 67. Thickness map (m) for the Middle Jurassic-Early Cretaceous deposits. Modified after Ziegler (1990); Baldschuhn et al. (2001); Maystrenko et al. (2006). Light grey areas border the extension of the documented (thermal) dome in the Mid North Sea domain. Abbreviations: **CG**=Central Graben; **LSB**=Lower Saxony Basin; **WNB**=West Netherlands Basin; **BFB**=Broad Fourteens Basin; **SPB**=Sole Pit Basin.

Figure 68 illustrates the modelled boundary conditions imposed in order to resemble the above described tectonic setting.

Displacement velocity vectors along the southern model boundary are chosen to resemble the observed kinematics of the Tethys sea-floor spreading system. Different magnitudes of velocity vectors (as reflected by the sizes of the arrows) are in agreement with a concentration of tectonic activity along the western portion of the spreading system, e.g. Ziegler (1999). The boundary conditions applied along the northern boundary of the study area are in consistence with Mid- to Late Jurassic rapid opening of the Central Atlantic and its propagation into the North Atlantic-Labrador Sea domain. The western and eastern boundary conditions are modelled to impose a sinistral translation within the study area as driven by counterclockwise rotation and northward drift of Africa-Arabia (e.g. Ziegler, 1999).

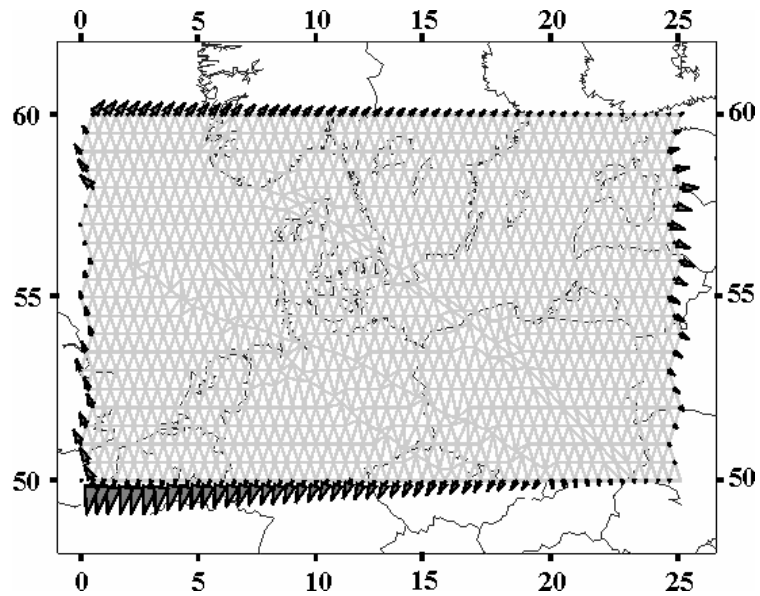


Figure 68. Adopted boundary conditions for the Middle-to-Late Jurassic.

Figure 69 illustrates the resulting pattern of horizontal deformation.

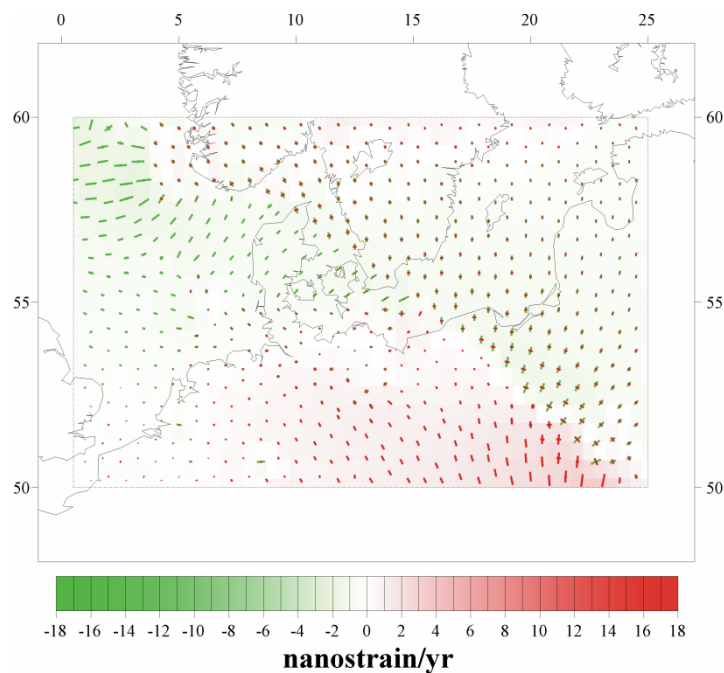


Figure 69. Horizontal strain rate eigenvectors (hyphens) and eigenvalues (background colour map) calculated modelling the Middle Jurassic evolutionary phase of the CEBS. Green colours indicate compressional deformation and red colours extensional deformation.

In agreement with more recent palaeotectonic reconstruction of Central and Western Europe (e.g. Ziegler, 1990, 2001; Stampfli et al., 2001), the results of Figure 69 suggest a change in the kinematic regime during Mid Jurassic. A domain of minor horizontal extension (red

colours) is still visible along the south-eastern border of the basin system. Within this area of mild horizontal extension, magnitudes of strain rates increase moving toward the east and reach their maxima under the southern segment of the Polish Trough. On the other hand, regional compression marks the Mid North Sea domain as well as the westernmost part of both the Danish and the North German basins. Kinematic activity decreases moving away from the western model boundary.

In Figure 70 the modelled effective strain rates are shown. The geometry of vertical movements parallels the pattern of horizontal deformation. The broad-scale pattern of relative vertical movements delineates two major domains in terms of vertical displacement. A zone of moderate subsidence is still visible in the southern part of the study area (blue colours in Figure 70).

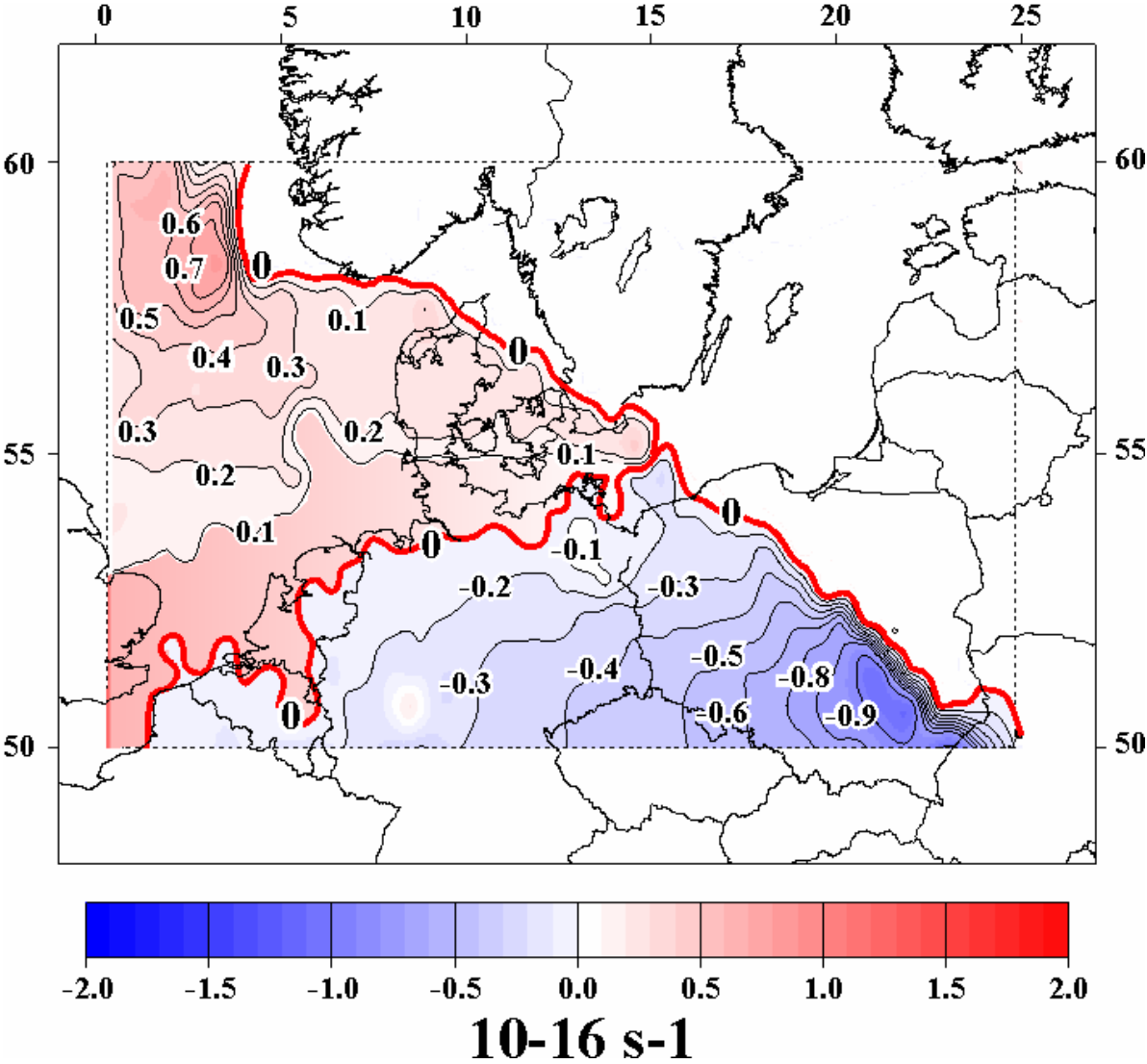


Figure 70. Effective strain rate (=rate of crustal thinning/thickening) results for the Middle-to-Late Jurassic times. Negative values-blue colours (positive values-red colours) stand for subsidence (uplift)

Major subsidence is found under the Mid Polish Trough which still forms a distinct feature. A linear gradient of increasing vertical subsidence towards the south-east segment of the trough axis is also modelled (e.g. Dadlez, 2003). In contrast, the north-western domain of the study area is characterized by uplift, red colours of Figure 70. Of course, details of the dimension and geometry of the Middle Jurassic Central North Sea Dome are not reproduced by the results of Figure 70 since its major structures are outside the model area. Nevertheless, the regional-scale extension of the dome is imaged. The area characterized by uplift ranges from the Viking Graben in the north to the southern North Sea (offshore Netherlands) in a north-south direction and from the eastern part of England through Denmark and northern Germany to the easternmost Baltic Sea in an east-west direction (Ziegler, 1990; Underhill & Partington, 1993).

Since the model do not consider any additional thermal-induced stress and/or disturbances, the occurrence of a thermal dome and its effective role in the observed uplift cannot be estimated. Nevertheless, the results of Figure 70 suggest a causal relationship between the model boundary conditions and the resulting subsidence/uplift deformation of Figure 70. From the results of Figure 70, it is likely that additional plate-boundary processes (i.e. rifting and final break-up of the Alpine-Tethys, subduction of the oceanic domains and oceanic spreading in the Central Atlantic and Arctic-North Atlantic) may have played an active role in determining Middle Jurassic tectonics (Ziegler, 1990; Stampfli & Borel, 2002). In this context, the results of Figure 70 confirms conclusions of previous studies (e.g. White & Latin, 1993) suggesting Middle Jurassic uplift movements in the area of the North Sea domain as invariably linked to and triggered by effective intra-plate compressional stresses related to rifting activity across the Arctic-North Atlantic domain.

### **Inversion phases**

The Permian sedimentary basins, Mesozoic grabens and wrench-induced troughs of the CEBS, evolved under a regional tensional regime that was related to the rifting phases which preceded the opening of the North Atlantic, the Norwegian-East Greenland Sea and the Tethys Ocean. During the Alpine orogenic cycle(s) some of these basins were inverted to varying degrees and some intervening highs were uplifted in response to wrench-faulting and/or upthrusting. The structural style of the inverted basins and basement uplifts (e.g. Krzyzwick, 2002) suggests that the basins have been inverted due to transmission of long wavelength compressional stresses and reactivation of old inherited structures.

The major reverse or transpressive structures accommodating uplift were located along the Elbe Fault System (e.g. Otto, 2003; Scheck-Wenderoth & Lamarche, 2005), along the Teisseyre-Tornquist Zone (e.g. Krzywiec, 2002), under the Polish Trough (e.g. Lamarche et al., 2003) and along the Sorgenfrei-Tornquist Zone (e.g. Vejbaek, 1990). The only non-inverted rifts were the Horn Graben, the Glückstadt Graben and the Oslo Graben (e.g. Ziegler, 1990; Maystrenko et al., 2006).

Two regional tectonic processes are thought to be responsible for foreland deformations and inversion of the sedimentary basins of the CEBS: (1) extensional tectonics across the Atlantic domain and (2) Alpine-Carpathian collision (Ziegler, 1990; Krzywiec, 2002; Cloetingh et al., 2006).

Within the structural Late Cretaceous-Early Tertiary regional inversion several pulses of accelerated tectonics can be identified. These distinct tectonic pulses may be related to the geometry of Alpine dynamics and the induced observed foreland deformation patterns (e.g. Ziegler, 1990; Mazur & Scheck-Wenderoth, 2005; Cloetingh et al., 2006). There are notable differences in the way these inversion phases affected the basins within the CEBS, with respect to timing, magnitude of vertical displacement and structural style. Here I follow the distinction widely accepted in literature which subdivides Late Cretaceous-Early Tertiary inversion tectonics within Western and Central Europe into three main pulses (e.g. Ziegler, 1990; Mazur & Scheck-Wenderoth, 2005; de Jager, 2003).

The first is namely referred to as the 'Sub-Hercynian' inversion phase. It started during Late Turonian-Early Senonian and culminated in Santonian to Campanian. It was followed by a second pulse of inversion during the Maastrichtian which persisted throughout the Early Paleocene, 'Laramide' inversion phase after Ziegler (1990). The more recent inversion phase occurred around the Eocene-Oligocene boundary and coincides with the so-called 'Pyrenean' tectonism.

### **First inversion phase**

In Figure 71 the adopted boundary conditions.

The lower boundary is model in order to resemble the Alpine front. It is forced to advance rigidly towards the north and to deform the surrounding areas in the form of a Gaussian function. The use of a rigid indenter rather than a deformable one to model the Alpine Front is not crucial since the analysis does not take the Alpine deformation as a part of the study. A symmetrical distribution of velocity vectors around the centre ( $\mu$ ) of the continuum

distribution is simulated to reproduce the observed lateral propagation of intra-plate compressional stresses from the indenting body. The observed A-subduction zone within the Austro-Alpine segment (Ziegler, 1990; Schmid et al., 2004) is modelled setting the centre of the distribution ( $\mu$ ) at the node located at 19.5° east longitude as indicates by the grey dot of Figure 71. Maximum imposed value for the advancing velocity is 2 mm/yr (Schmid et al., 1996; Bonini et al., 1999; Marotta et al., 2002). The variance ( $\sigma$ =semi-amplitude) of the distribution is kept equal to half the semi-longitudinal length of the entire mesh, e.g. 6.5°~600/700 km, so that to resemble the lateral extension of the area which underwent “Sub-Hercynian” compressional deformation.

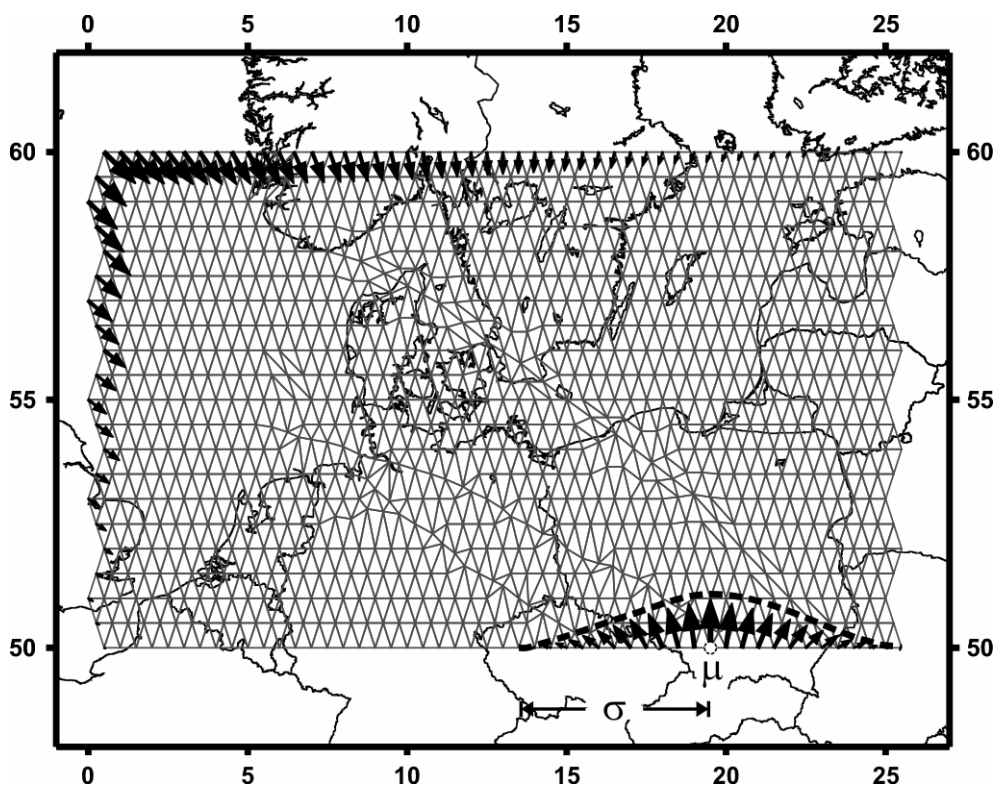


Figure 71. Adopted boundary conditions to model the ‘Sub-Hercynian’ phase of inversion. Velocity vectors (black arrows) along the northern and western boundaries reflect early extension tectonics across the Mid Atlantic while the black arrows along the southeastern boundary resemble the Alpine collision Front.

Proto-Atlantic extensional activity is reproduced imposing fixed velocities along the western and the northern boundaries of the study area, black arrows of Figure 71.

The bulk of late Cretaceous extensional tectonic activity in the Atlantic system was located in the domain between Laurentia and Baltica in the north and in the area of the Bay of Biscay more to the south (Ziegler, 1990; Lundin & Dorè, 1997). However, previous studies on the Betic Margin and the other basins of Iberia (e.g. Martín-Chivelet, 1997) have demonstrated a

major change in the Africa to Europe relative motion that occurred by Late Santonian-Early Campanian times. Following these studies, the onset of convergence of Africa with Europe induced a major reorganization at the Iberia-Europe and Iberia-Africa boundaries. The main event was the termination of tectonic extensional activity in the Bay of Biscay. In order to model the observed extensional dynamics across the North Atlantic domain, fixed horizontal deformation velocities are imposed along the northern and western boundaries of the study area. Magnitudes and vector orientations of the imposed velocity boundary conditions are adopted to fit the observed kinematic and dynamic setting as well as information from previous studies concerning the northern North Sea and the Mid Norwegian margins (e.g. Pascal & Gabrielsen, 2001).

The eastern boundary is kept fixed, i.e. shear stress free boundary. As already suggested by previous studies, (e.g. Golke & Coblenz, 1996; Marotta et al., 2004), this assumption reflects a decoupling between the western and eastern parts of the Eurasian plate. Here it is adopted to focus the entire volume of intra-plate deformation within the study domain and to avoid edge effects related to artificial stress accumulation along this boundary.

In Figure 72 the modelled horizontal deformation field is shown.

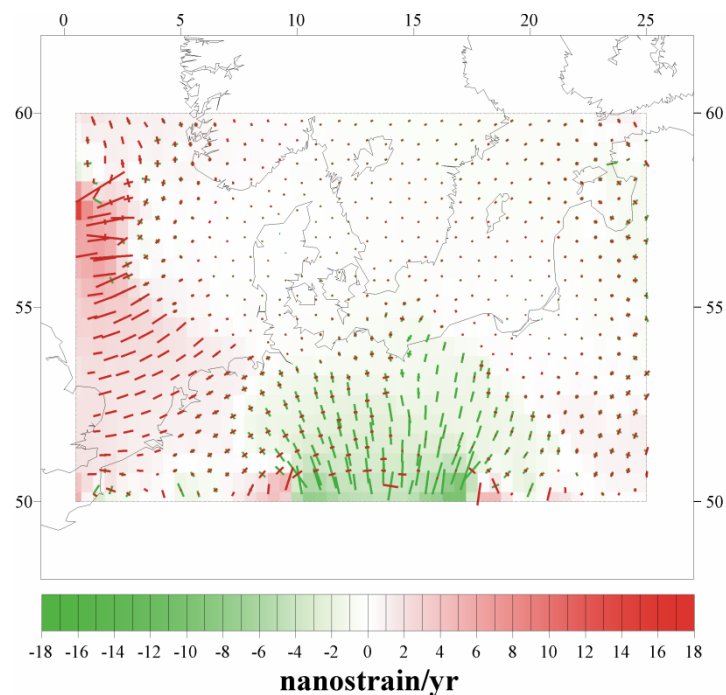


Figure 72. Horizontal strain rate eigenvectors (arrows) and eigenvalues (background colour map) for the 'Subhercynian' inversion phase. Green colours indicate compression, and red colours extension.

Due to the adopted boundary condition along the southern border, increased strain rate values are found under the Elbe Fault System. The structural contrast modelled in the lower crust along the Elbe Line results in a gradual decrease of strain rate magnitudes under the relative strong North German Basin more to the north. Compressional deformation also marks the domain of the Polish basin. The area of increased kinematics is bordered by the Teisseyre lineament to the north-east resulting in a sudden decrease of strain rate values in the stiff Baltic domain.

Figure 73 illustrates the observed intra-plate deformation pattern, after Ziegler (1986).

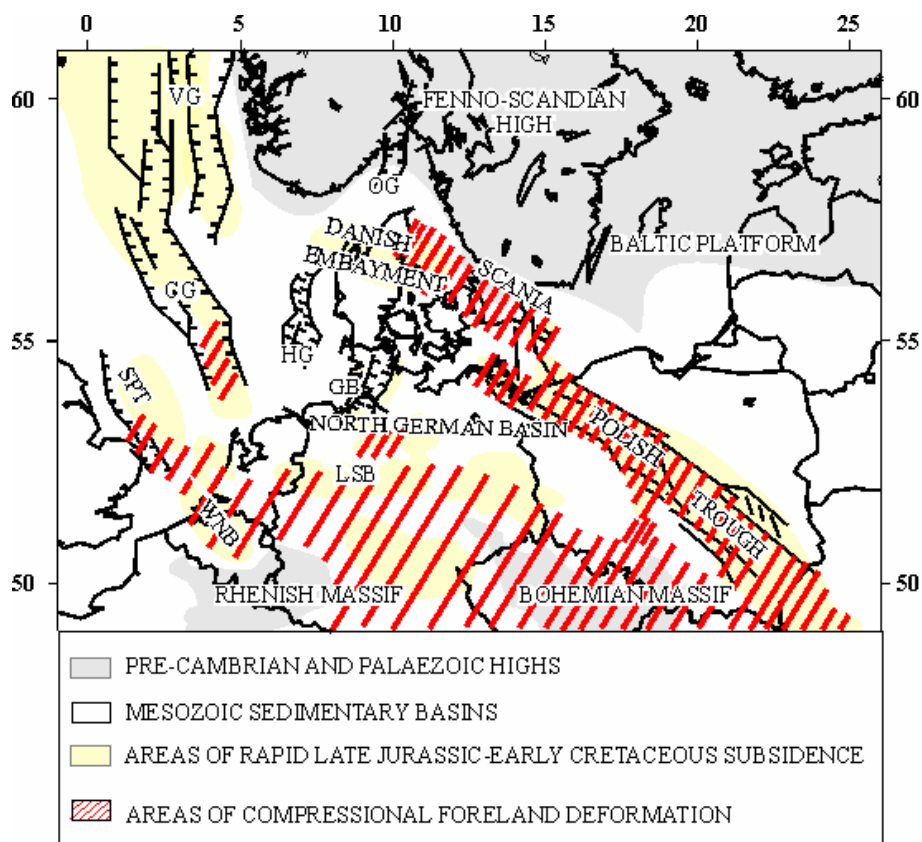


Figure 73. Structural map of Alpine deformation pattern for the 'Sub-Hercynian' inversion phase, modified after Ziegler (1986). Abbreviations: VG=Viking Graben; CG=Central Graben; OG=Oslo Graben; HG=Horn Graben; GG=Glückstadt Graben; SPT=Sole Pit Basin; WNB=West Netherlands Basin; LSB=Lower Saxony Basin.

Deformations of this age are restricted to areas located along the southern margin of the basin system extending from the Polish Trough in the east (Dadlèz et al., 1995; Krzywiec, 2002, 2006; Lamarche et al., 2003; Mazur & Schek-Wenderoth, 2005; Mazur et al., 2005), through the West Netherlands, Broad Fourteens Basins (Nalpas et al., 1995; De Lugt et al., 2003; de Jager, 2003) and the Lower Saxony Basin (Betz et al., 1987; de Jager, 2003), to the Sole Pit Basin in the west (Van Horn, 1987). Minor intraplate compressional deformations are also

recognized along the Fennoscandian Border Zone, mainly limited to Scania (Norling & Bergström, 1987), and in the Dutch sector of the North Sea Central Graben (Vejbæk & Andersen, 1987; Liboriussen et al., 1987; Van Wijhe, 1987).

In Figure 74 the obtained results are shown in terms of effective strain rate (Figure 74a) and in terms of the direction of the largest horizontal component of the stress tensor,  $S_{Hmax}$ , superimposed on the associated stress regime (Figure 74b).

The observed kinematic trend is well imaged. The areas affected by inversion (red coloured regions of Figure 74a) are located along the southern margin of the domain.

*Sole Pit Basin.* The Sole Pit Basin underwent a first phase of mild inversion since Late Turonian times which reached its peak during the Campanian (Ziegler, 1990). Accordingly, the results of Figure 74a show an area of moderate uplift under the Sole Pit Basin. At the same time, the modelled (transpressive) stress regime with a NNE-SSW to N-S orientation (Figure 74b) is in agreement with previous palaeo-stresses analyses performed in Great Britain, (Hibsch et al., 1995), and with results from seismic experiments (e.g. Van Hoorn, 1987).

*Netherlands basins (Dutch Central Graben, Broad Fourteens Basin, West Netherlands Basin, Central Netherlands Basin):* During Turonian-Early Senonian all Dutch rift basins were inverted to various degrees. The bulk of positive vertical displacement is found under the Broad Fourteens Basin and the West Netherlands Basin whereas only relative minor inversion affected the Dutch Central Graben (de Jager, 2003). The observed style of compressional deformation, with decreasing intensity moving towards northwest, is resembled by the effective strain rate results. Figure 74a joins a region of greater amount of uplift in the eastern Netherlands with a domain of reduced volume of vertical displacement offshore the Netherlands, in the southern part of the North Sea Central Graben. Previous studies, e.g. Van Wijhe (1987), have related the observed deformation pattern to the presence of a NNE-SSW-oriented transpressional stress regime bending toward N-S entering north-west Germany. Accordingly, the modelled stress field (Figure 74b) depicts a NE-SW to N-S orientation of  $S_{Hmax}$  associated with a transpressive regime as indicated by the blue coloured arrows.

*Lower Saxony Basin:* Previous published studies, (Betz et al., 1987; de Jager, 2003), have suggested a heterogeneous style of compressional deformation for the Lower Saxony Basin. Minor deformations within its Dutch sector were counteracted by highly inverted structures under its central part in northern Germany. The amount of modelled vertical deformation rate (Figure 74a) increases moving eastward and reach its maximum values below the south-easternmost part of the basin in agreement with the observed variable deformation style.

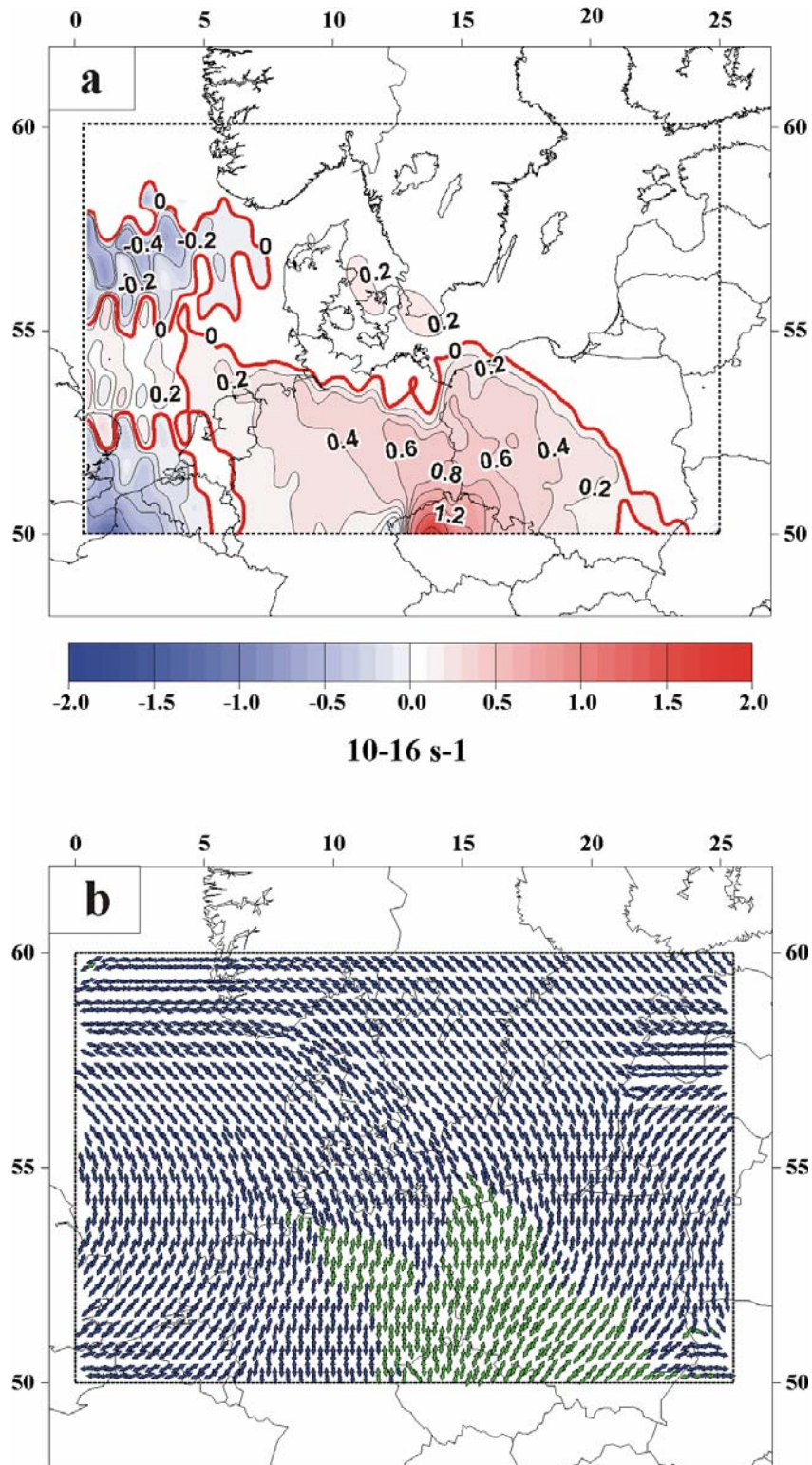


Figure 74. Obtained results for the first phase of compressional deformation ('Sub-Hercynian'). (a) Effective strain rate (=rate of crustal thinning/thickening): positive values-red colours (negative values-blue colours) stand for subsidence (uplift). Thick red isolines indicate no vertical deformation. (b) Maximum horizontal stress component ( $S_{Hmax}$ ) orientation (arrows) and associated stress regime (colours): different coloured arrows are used to represent the stress regime as calculated from direct comparison of the three components of principal stresses ( $\sigma_1, \sigma_2, \sigma_3$ ). Green coloured arrows indicate thrust faulting, and blue coloured arrows strike-slip (transpressive) fault regime.

The results of Figure 74b suggest that compressional structures within this area could be associated with a N-S-oriented transpressive/compressive stress field related to the first phases of Alpine orogeny as supported by analyses of different reflection seismic lines, (e.g. Mazur & Scheck-Wenderoth, 2005).

*North German Basin.* Within the North German Basin the most intense inversion-related uplift was observed under the WNW-ESE-striking Elbe Fault System along the southern margin of the basin (e.g. Scheck-Wenderoth et al., 2002; Otto, 2003). Almost no inversion occurred either under the central part of the basin or below the N-S-oriented Mesozoic Horn and Glückstadt grabens (Mazur et al., 2005; Maystrenko et al., 2006). In agreement with these observations, Figure 74a images an area of almost no vertical deformation under the centre of the basin flanked by a region of increased crustal thickening along the southern basin margin. Moving from the southern boundary of the model towards the basin, a change in the orientation of the inverted structures is also visible (e.g. Mazur & Scheck-Wenderoth, 2005). Approaching the southern margin of the basin the isolines of vertical displacement orientate preferentially along a WNW-ESE direction. The geometry of the deformation pattern of Figure 74a is related to the structural setting of the region. Specifically, the increased crustal strength below the North German Basin prevents crustal failure under the basin thus favouring strain concentration along its margins where domains of weakness (i.e. Elbe Fault System) are more prone to be reactivated under the effective stress regime of Figure 74b. Consequently, deformation is focused along and runs parallel to the modelled structural contrast. On the other hand, in the absence of structural contrasts, stress and therefore strain vectors follow the geometry of the boundary conditions. The presence of lateral rheological contrasts also affects the stress field of Figure 74b. The weak lower crustal domain modelled under the Elbe Fault System divides the basin domain into two different “*stress provinces*”. The presence of N-S-oriented stresses along the southern basin margin is counteracted by N-S- to NNW-SSE-oriented stresses under the basin centre. Bending in  $S_{Hmax}$  orientation is accompanied by a change in stress regime as enlightened by the different colours of the arrows. The change in stress regime and  $S_{Hmax}$  orientation is related to the contrasting mechanical weakness of the Elbe Fault System with respect to the surrounding areas. The Elbe Fault System concentrates compressional intra-plate stresses thus ‘shielding’ the central part of the basin in the north from the compressive far-field stresses released by the Alpine front.

*Polish Trough.* Late Turonian-Early Senonian inversion of the Polish Trough resulted in the uplift of a central NW-SE-elongated horst along the former basin axis, i.e. the Mid Polish Swell, and two bordering marginal troughs (e.g. Krzywiec, 2002, 2006; Mazur et al., 2005).

Analyses of seismic data as well as results from structural models (e.g. Lamarche et al., 2003; Dadlez, 2003), have considered the observed linear inverted structures as first-order, continental-scale phenomena induced by the geometry of the Teisseyre-Tornquist Zone. In general agreement with observations, the results of Figure 74a depict linear, NW-SE-striking, compressional deformed structures under the basin area. The Teisseyre-Tornquist Zone is modelled in order to represent a boundary between the south-western edge of the stronger and stable East European Craton and the relative weaker Variscan crust more to the south. Consequently, it prevents a release of compressional intra-plate stresses and related (compressive) strains to the north, thus inducing a concentration of deformation under the basin. In absence of internal structural heterogeneities, compressional intra-plate deformation is primarily driven by the applied boundary conditions. At the same time, the presence of lateral rheological contrasts exerts the major control on the geometry and localization of intra-plate deformation explaining local variations in the kinematics and dynamics.

In consistency with results from recent palaeo-stress studies (e.g. Lamarche et al., 2002), the modelled stress field of Figure 74b images a dominantly NE-SW-oriented compressive regime under the basin, green arrows limited by the Teisseyre-Tornquist Zone to the north. Entering the East European Craton a change from a thrust fault regime to a strike-slip regime occurs which is accompanied by a bending of almost 45° in the direction of the largest horizontal stress component ( $S_{Hmax}$ ). Stress rotation becomes more pronounced in the northeastern flank of the basin axes where the structural boundary considered is orientated obliquely to the modelled boundary conditions. Again, major deviations of stress directions as well as permutations in the stress regime are associated with the presence of structural lithospheric-scale contrasts. Hence, the results of Figure 74a and Figure 74b show that the Teisseyre-Tornquist Zone acts as a buttress along which the compressional intra-plate stresses and associated strains are localized.

### **Second inversion phase**

This phase occurred during latest Late Cretaceous (Maastrichtian)-Early Paleocene (Danian) times and was more pervasive than the previous “Sub-Hercynian” phase. The bulk of tectonic activity was concentrated within the Eastern Alpine-Western Carpathians orogenic system (Schmid et al., 2004). The strong “Laramide” deformation of the Alpine and Carpathians foreland indicates a mechanically coupling between the Eastern Alpine-Western Carpathians

nappe system and their foreland (Ziegler, 1986; Vejabaek & Andersen, 1987; Plašienka et al., 1997; Oszcypko, 2006).

Figure 75 shows the imposed boundary conditions.

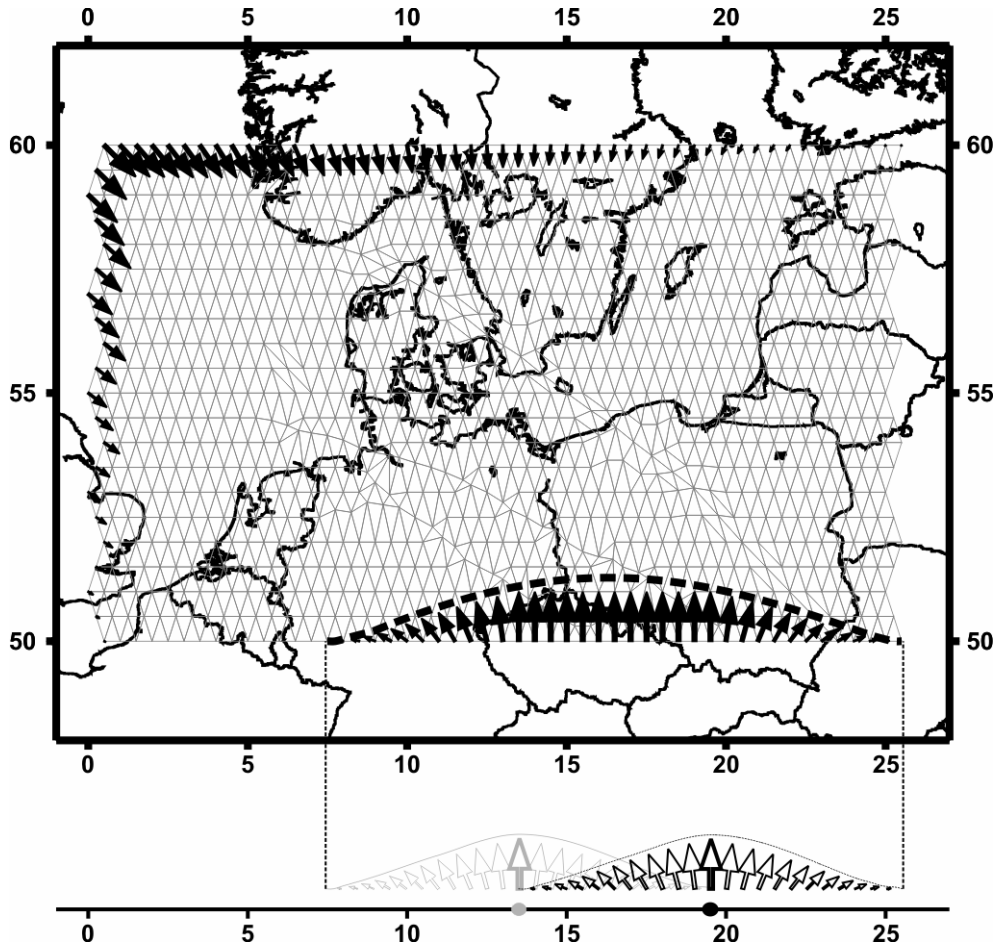


Figure 75. Adopted boundary conditions to model the 'Laramide' inversion phase. Velocity vectors along the western and northern model boundaries resemble extensional tectonic activity across the future Atlantic Ridge System. Black arrows along the southern domain reflect the collisional intraplate forces released by the Alpine-Carpathians thrust front. On the left bottom side of the figure the two starting normal distributions are also shown. Light grey and black dots indicate the centres of their respective centres,  $\mu_1$  and  $\mu_2$ .

The western, eastern and northern boundaries are the same as described above. Figure 76 illustrates the main points of the followed procedure for generating the new boundary condition along the southern border, i.e. Alpine front.

Two normal distributions,  $N_{(\mu_1, \sigma_1)}(x)$  and  $N_{(\mu_2, \sigma_2)}(x)$ , with same amplitudes, i.e.  $\sigma_1 = \sigma_2$ , are summed (*Case a*). Their respective locations are chosen so that the centre of each function,  $\mu_i$ ,  $i=1,2$ , should match the ending point of the other, i.e.  $\mu_1 = \bar{x}_2$  with  $\bar{x}_2 : N_{(\mu_2, \sigma_2)}(\bar{x}_2) = 0$  and *vice versa*, (*Case b* upper figure). Due to the symmetrical nature of the

distributions, i.e.  $N(x) = N(-x)$ , resulting velocity vectors in the common area point northward (*Case b* lower figure). The imposed symmetry in the mutual location adopted requires that magnitudes of velocity vectors in the common areas are equal to the arithmetic mean of the maxima of the two starting functions, i.e.  $\frac{(N_{(\mu_1, \sigma_1)}(x = \mu_1) + N_{(\mu_2, \sigma_2)}(x = \mu_2))}{2}$ . The condition of equal amplitude, i.e.  $\sigma_1 = \sigma_2$ , leads to  $\frac{(N_{(\mu_1, \sigma_1)}(x = \mu_1) + N_{(\mu_2, \sigma_2)}(x = \mu_2))}{2} = N_{(\mu_1, \sigma_1)}(x = \mu_1) = N_{(\mu_2, \sigma_2)}(x = \mu_2)$ . The resulting function is again a normal distribution,  $N_{(\mu, \sigma)}(x)$ , with amplitude  $\sigma = \sigma_1 + \sigma_2$  and mean  $\mu = \frac{|\mu_1 + \mu_2|}{2}$  (*Case c*).

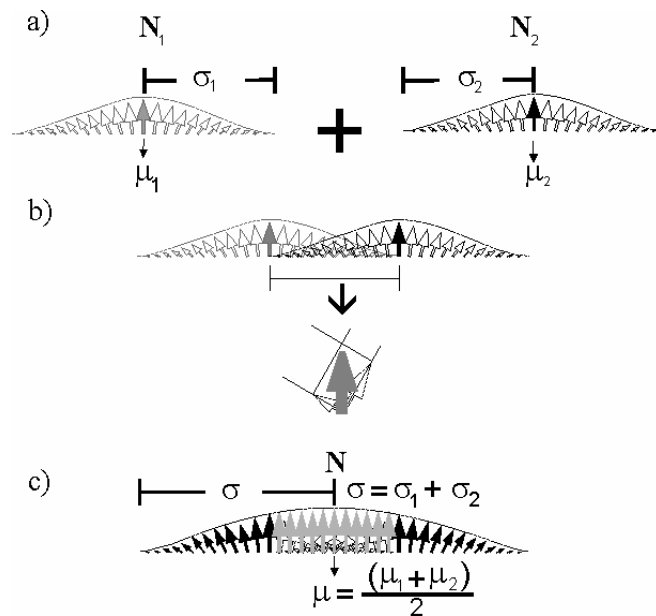


Figure 76. Scheme representing the procedure followed to generate the boundary condition resembling the Alpine Front for both the ‘Laramide’ and the ‘Eocene-Oligocene’ inversion phases.

To resemble the observed concentration of tectonic activity within the Eastern Alpine-West Carpathians thrust front during ‘Laramide’ inversion phase, (Schmid et al., 2004), the first distribution, modelled in order to resemble the Carpathians orogenic wedge, is centred at the node with  $\mu_1=19.5^\circ\text{E}$  longitude, black dot of Figure 75. The second distribution is centred at the node with  $\mu=13^\circ$  east longitude in order to model the Eastern Alpine thrust front, grey dot of Figure 75.

In Figure 77 the main observed inverted structures are shown.

The “Laramide” tectonic phase provided the main inversion of the Polish Trough (Dadlèz et al., 1995; Krzywiec, 2002, 2006; Lamarche et al., 2003; Mazur & Scheck-Wenderoth, 2005; Mazur et al., 2005) and of the Elbe Fault System along the southeastern margin of the North German Basin (e.g. Scheck-Wenderoth et al., 2002; Otto, 2003). At the same time, vertical displacement occurred under the main troughs along the southern margin of the CEBS, (Nalpas et al., 1995; De Lugt et al., 2003; de Jager, 2003), as well as in the Fennoscandian Border Zone (Vejbæk & Andersen, 1987; Liboriussen et al., 1987). A coeval northward propagation of compressional deformed structures occurred, as indicated by inversion movements below the onshore part of the Danish Basin (Vejbæk, 1990) and in the offshore area of southern Norway (Pegrum, 1984).

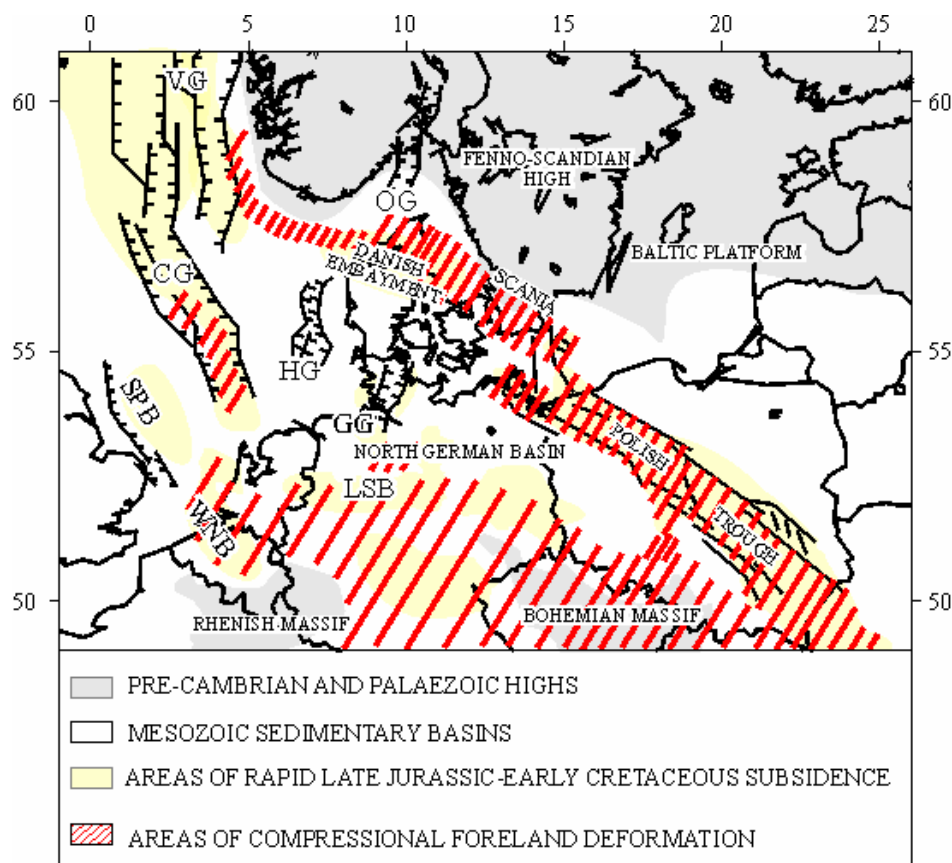


Figure 77. Structural map of Alpine foreland deformation for the ‘Laramide’ inversion phase, modified after Ziegler (1986). See Figure 73 for abbreviations.

Figure 78 illustrates the horizontal strain rate results. With respect to the previous phase, see Figure 72, now compressional deformation occurs under a widespread area. Domains of increased kinematic activity still characterize the Polish Basin and the Elbe Fault System along the south and southeast border of the basin system. At the same time, increased

magnitudes of strain rate eigenvectors are found under western northern Germany and in the Netherlands. In addition, a northward propagation of horizontal compression occurs. In agreement with observations, compressional deformation is found under Denmark as well as in the easternmost part of the Mid North Sea.

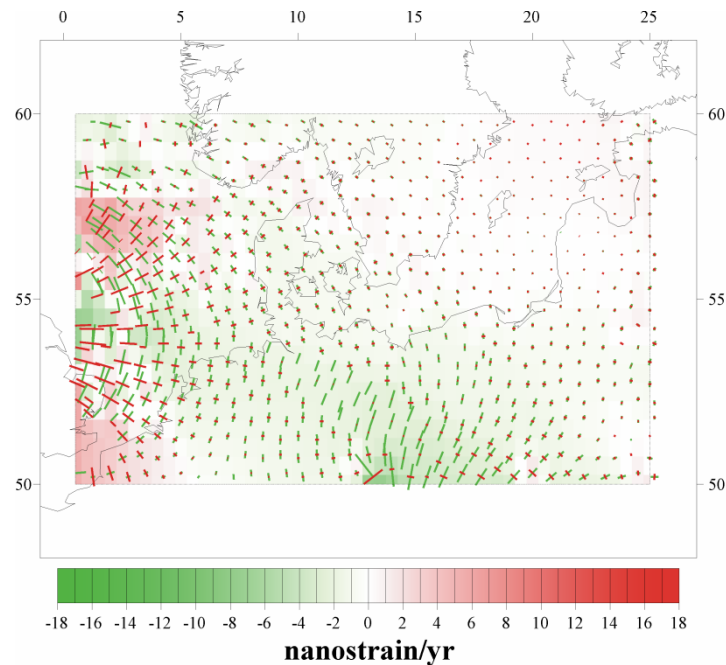


Figure 78. Horizontal strain rate eigenvectors (hyphens) and eigenvalues (background colour map) for the 'Laramide' phase of inversion.

Figure 79a illustrates the modelled vertical effective strain rates, while in Figure 79b the orientation of the maximum horizontal stress component,  $S_{Hmax}$ , and the associated stress regime are shown. In agreement with the horizontal deformation field of Figure 78, stronger vertical deformation marks the southern domain of the study area compared to the "Sub Hercynian" phase. The main inverted structures are located beneath the southern margin of the North German Basin, showing a WNW-ESE orientation, and along a NW-SE-trending axes in the Mid Polish Trough. At the same time, uplift also affects the area of the Fennoscandian Border Zone, Denmark and the Danish part of the Central North Sea Graben. *Sole Pit Basin*: Previous studies (e.g. Van Hoorn 1987; Ziegler, 1990), have suggested the absence of 'Laramide' inversion tectonics under the Lower Saxony basin. In general agreement with observations, almost no vertical deformation affects the south-western part of the study domain (Figure 79a).

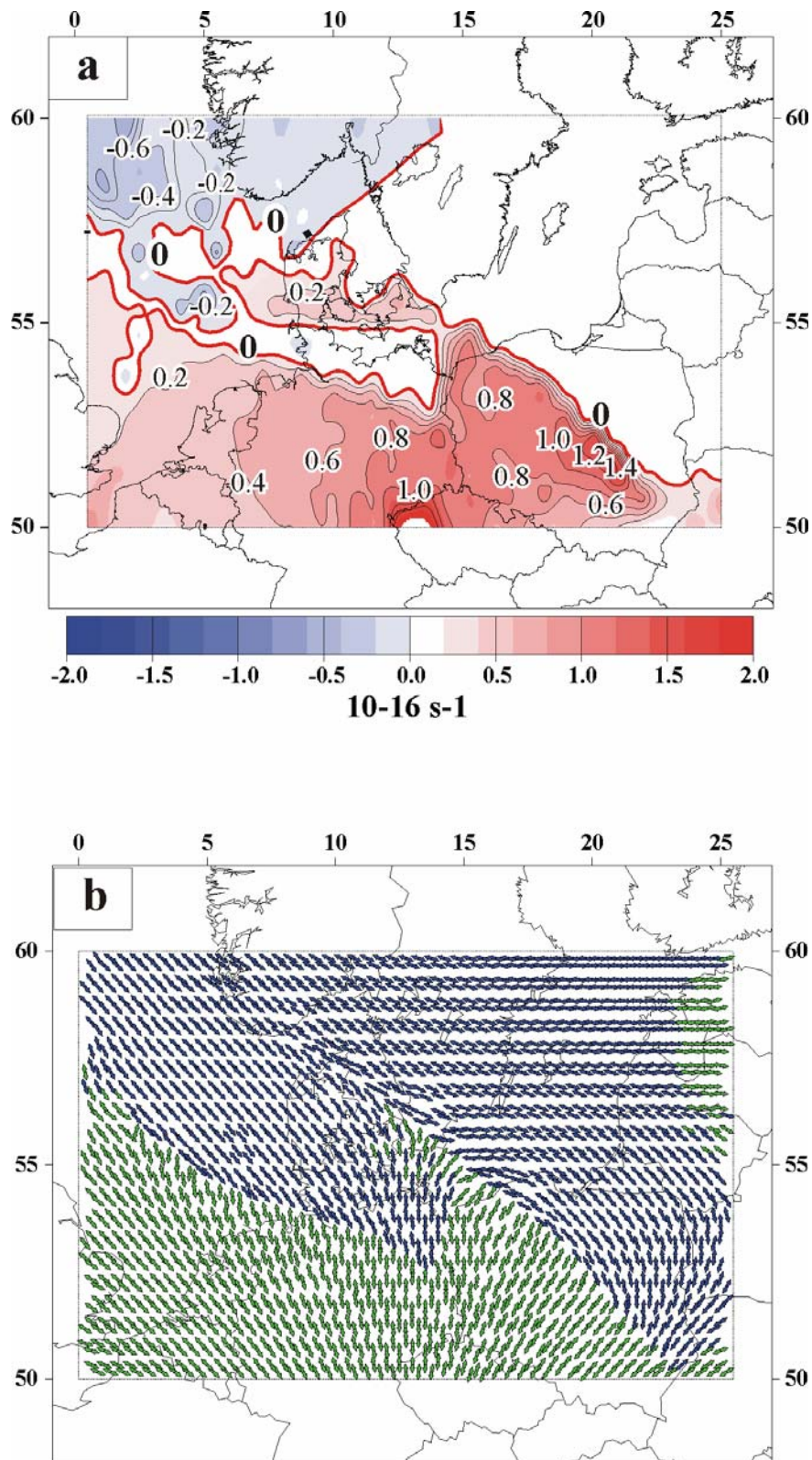


Figure 79. Modelling results for the 'Laramide' phase of compressional deformation. (a) Effective strain rates (=rate of crustal thinning/thickening): positive values-red colours (negative values-blue colours) stand for uplift (subsidence). Thick red isolines indicate the boundary of the areas of no vertical deformation. (b)  $S_{Hmax}$  orientation (arrows) and stress regime (colours): Different coloured arrows are used to represent the different stress regimes obtained: green colours indicate thrust faulting, and blue colours strike-slip (transpressive) fault regime.

*Danish Basin:* “Laramide” inverted structures are localized in the south-western part of the Danish Basin, and are associated to N-S- to NNW-SSE-directed transpressional stresses (Vejbæk & Andersen, 1987).

Figure 79a shows compressional-related uplift in the southern continental part of the Danish Embayment as well as under its offshore prolongation more westward associated with a NNW-SSE transpressional regime (Figure 79b).

*Lower Saxony Basin:* “Laramide” inversion of the Lower Saxony Basin reached its climax during Mid Paleocene with the main inverted structures located in its German sector (de Jager, 2003). The southern parts of the eastern sector of the basin were in general more uplifted than the northern ones. This differential deformation is reflected by major upward deformation in the south-eastern sector of the basin and a gradual decrease in volume of vertical displacement moving north-westward.

*North German Basin:* Turning to the North German Basin, Figure 79a shows the observed heterogeneous intra-plate deformation (e.g. Scheck-Wenderoth et al., 2002; Otto, 2003). Inversion is in fact localized in restricted areas interrupted by undeformed domains between them. Inversion occurs along the southern margin of the basin, under the Elbe Fault System, but not in its central part.

The modelled stress field of Figure 79b displays a N-S-oriented  $S_{Hmax}$  associated with a thrust fault regime in the central part of the Elbe Fault System, (green arrows). This feature correlates with observations pointing to a reactivation of the individual faults of the Elbe Fault System as thrust or transpressional faults (e.g. Scheck-Wenderoth et al., 2002; Otto, 2003).

Approaching the southern margin of the North German Basin a change from a purely compressive to a transpressive stress regime superposed on a deviation in the direction of the largest horizontal stress component towards NW-SE is visible. The observed deviation of stress vectors occurs along the rheological contrast across the southern margin of the basin and indicates a strong component of horizontal movements in the northwestern part of the Elbe Fault System. A further local deviation in the direction of maximum compression toward NNE-SSW is also modelled along the eastern part of the basin. The local rotation in the direction of the maximum horizontal compression toward the external part of the basin is induced by the stiff (lower) crust modelled under the basin which acts as a ‘barrier’ for the transmission of intraplate stresses in the central part of the basin.

*Polish Trough:* Moving toward the Polish Trough, the main structural trend of inversion in Figure 79a is still the NW-SE-elongated horst of the Mid Polish Swell. This feature is in agreement with the observed shape of inversion which was characterized by a reverse

reactivation of previous Mesozoic extensional faults along the axial part of the basin (Ziegler 1990; Dadlez et al. 1995; Stephenson et al. 2003; Mazur et al. 2005). The horst structure is observed along the whole length of basin. The modelled geometry of inverted structures is most likely the result from a large-scale, lithospheric (?), effect. As demonstrated by previous thermo-mechanical models of inversion mechanisms, the localization of inversion zones is related to differential shortening of the rheology of the lithosphere (Hansen et al., 2000; Nielsen & Hansen, 2000; Gemmer et al., 2002). Zones of crustal weakness suffer from greater shortening relatively to the neighbouring stronger crust. In this framework, the Teisseyre-Tornquist Zone above which the Mid Polish trough developed represents such a weakness zone. Consequently, the modelled geometry of deformation is the surface expression of the tectonic ‘squeezing’ of the Teisseyre-Tornquist Zone induced by the advancing Alpine-Carpathians front superimposed on the ‘buttressing’ effect of the relative mechanical stronger southern edge of the East European Craton. The stress results of Figure 79b display an effective horizontal compressional regime NE-SW-oriented in the area of the Polish basin. This dynamic setting may have induced the (reverse) reactivation of former (normal) longitudinal and transversal faults (e.g. Swidrowska & Hakenberg, 2000). Our results suggest that the linear horst structure is more likely the result of ongoing intracontinental compression of a weak lithosphere, i.e. the Teisseyre-Tornquist Zone, rather than the consequence of a relaxation of compressional stresses during ‘Laramide’ tectonics.

### **Third inversion phase**

In Eocene-Oligocene times a westward shift of inverted structures occurred. By the end of Paleocene, relaxation of compressional foreland stresses started in the Eastern Alpine-Western Carpathians orogenic front (Schmid et al., 2004; Oszcypko, 2006). This reflects the termination of inversion movements in Poland as well as across the Outer Carpathian Foreland Basins (Krzywiec, 2002, 2006; Mazur et al., 2005). In contrast, Middle Eocene-Early Oligocene saw the inception of newly formed true A-subduction zones in the Western Alps which were kinematically linked to the WNW-ESE-moving Adriatic indenter (Ziegler, 1990; Schmid et al., 2004).

Eocene-Oligocene intra-plate compressional deformation patterns are also structurally linked to the beginning of sea-floor spreading rates in the different segments of the North Atlantic-Iceland Sea and to a continued intra-Oligocene reorganization of sea-floor spreading axes in

the Norwegian-East Greenland Sea and Labrador Sea (Lake & Karner, 1987; Bukovics et al. 1984; Ziegler, 1990; Cloetingh et al., 1990).

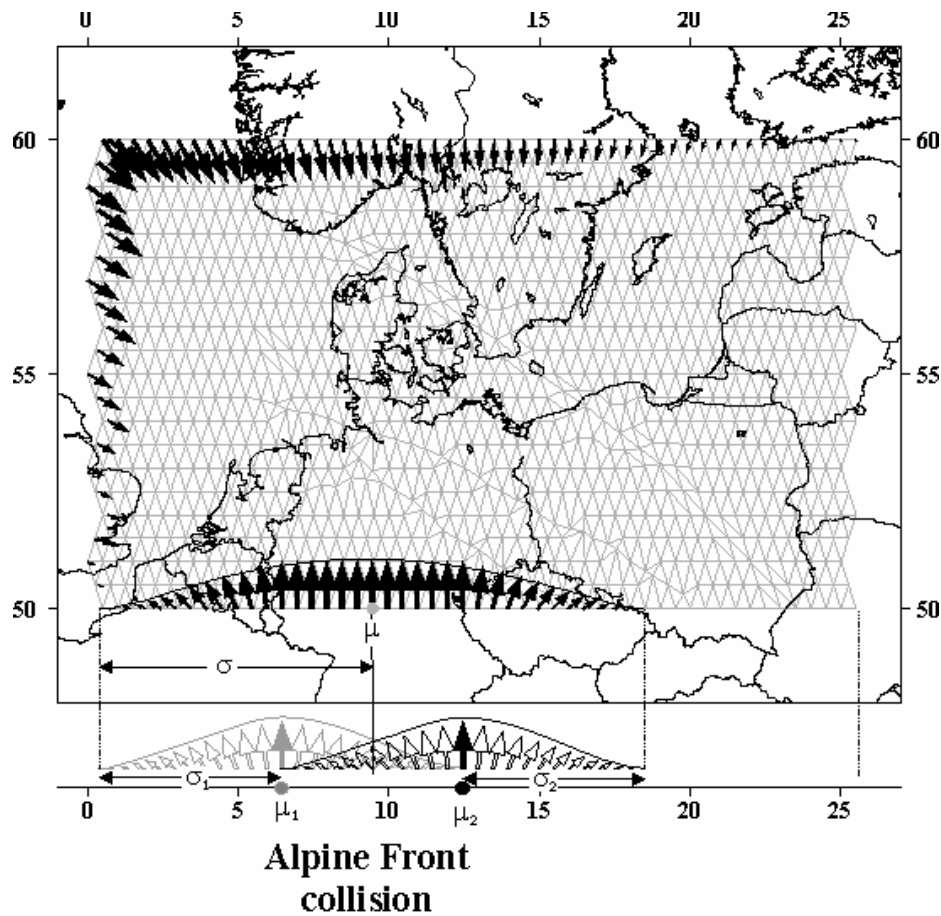


Figure 80. Velocity boundary conditions for the last phase of inversion.

Figure 80 shows the adopted boundary conditions. Along the eastern boundary a shear stress free condition is chosen. To resemble Late Eocene reorganization of sea-floor spreading axis in the North Atlantic domain, increased magnitudes of the velocity vectors along the northern and western boundaries are considered. The maximum value of horizontal deformation velocity ( $\sim 0.5$  mm/yr) may be considered as an upper bound for ridge push forces (Richardson & Reding, 1991).

To resemble the active Alpine thrust front, the procedure explained above (Figure 76) is adopted. The observed westward shift of tectonic activity is reproduced centring the first distribution at  $\mu_1=13^\circ\text{E}$  and the second at  $\mu_2=6.5^\circ$  east longitude.

In Figure 81 the compression-induced deformation pattern for the most recent phase of inversion is presented.

Due to the westward shifting of Alpine tectonic activity as well as to the inception of sea floor spreading activity within the Norwegian-East Greenland domain, the North Sea Central

Graben underwent a phase of increased subsidence (e.g. Van Wees & Cloetingh, 1996). In contrast, uplift continued to affect the southwest border of the CEBS (Ziegler, 1990). Eocene-Oligocene inversions occurred in the Sole Pit Basin (Van Hoorn, 1987), mainly during Late Eocene-Early Oligocene, along the West Netherlands and Broad Fourteens basins (Van Vijhe, 1987; Nalpas et al., 1995; de Jager, 2003) and, though minor, in the Lower Saxony Basin (Betz et al., 1987). Inverted structures were essentially lacking in areas located more to the east.

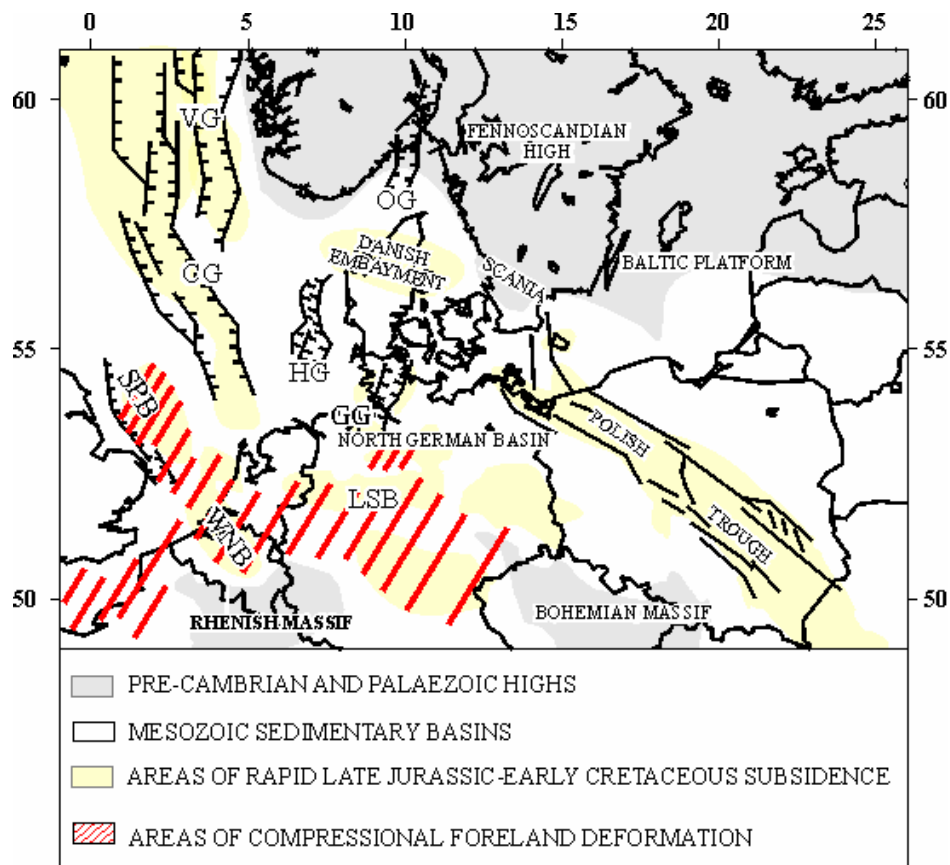


Figure 81. Structural map of Alpine foreland deformation for the last phase of compressional deformation during Late Eocene to Early-to-Middle Oligocene, modified after Ziegler (1986). See Figure 73 for abbreviations.

In Figure 82 the modelled horizontal deformation pattern for the Late Eocene-Oligocene inversion phase is shown. In consistence with the adopted boundary conditions along the southern border, the bulk of horizontal deformation occurs across the southwestern border of the basin system. The eastern boundary of this domain of compressional deformation run across the Elbe Line whereas almost no kinematic activity occurs under the Polish Basin more to the east as well as in the central part of the North German Basin in the north. Increased velocity vectors along the northern and western boundaries result in a change of kinematic activity in the central and northern domain of the basin with respect to its southern margin.

Compression gradually abates and a dominance of compressional deformation starts to dominate at middle to high latitudes.

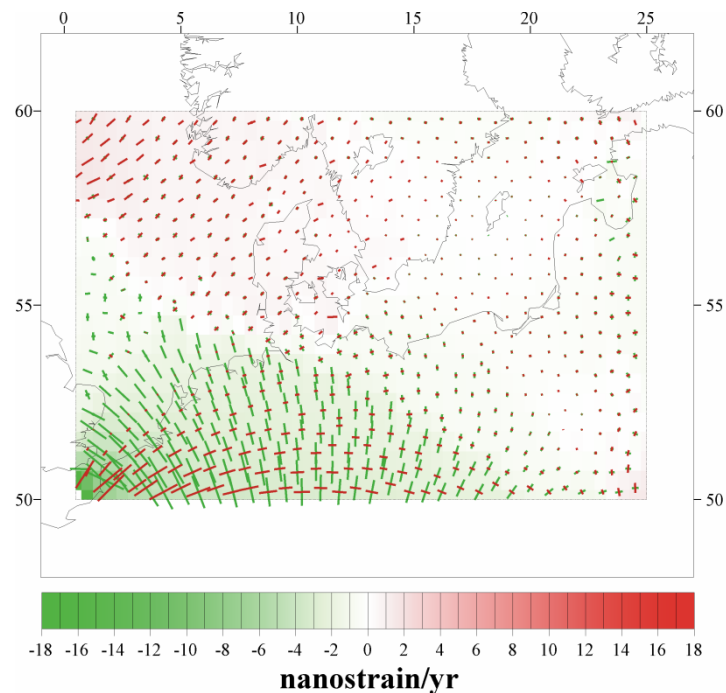


Figure 82. Horizontal strain rate eigenvectors and eigenvalues for the last phase of inversion. Red colours indicate extensional horizontal deformation, and green colours compressional horizontal deformation.

Figure 83 shows the modelled vertical deformation style (Figure 83a) and the  $S_{Hmax}$  orientation (Figure 83b). The results are in agreement with the overall features. No vertical movements occur in the already stabilized Polish Trough, while a relative minor degree of inversion still frames the Elbe Fault System. The main vertical movements are found in the south-westernmost part of the basin system. Adjacent to this region of increased uplift the results of Figure 83a illustrate an opposite trend of vertical deformation (subsidence) within the entire North Sea rift System (e.g. Cloetingh et al., 1990).

*Sole Pit Basin:* A second phase of increased inversion characterized the Sole Pit Basin throughout the Oligocene (Van Hoorn, 1987). Although the amount of crustal shortening associated with the Oligocene inversion of the Sole Pit Basin is difficult to estimate, a heterogeneous deformation pattern appeared to have affected the basin. Minor volume of crustal thinning within its north-east sector (i.e. Silver Pit Basin) mainly associated with salt diapirism was counteracted by high volume of vertical displacement within the south-western part of the basin. Looking at the results of Figure 83a, the isolines indicate an increase in uplift moving south. Palaeostress analysis carried out in south-eastern England (Hibsch et al., 1995), have associated this tectonic event with a NNW-SSE-oriented compressive stress

regime synchronous with the “Pyrenean” compressional stage. In agreement with these observations, the modelled results of Figure 83b image a thrust fault regime associated with a NNW-SSE-directed  $S_{Hmax}$  across this part of the study domain.

*Netherland basins (Dutch Central Graben, Broad Fourteens Basin, West Netherlands Basin, Central Netherlands Basin):* Late Eocene-Early Oligocene inversion pulse did not affect all basins (de Jager, 2003). Renew uplift occurred under the West Netherlands Basin and the Broad Fourteens Basin and with minor vertical displacement below the Central Netherlands Basin. On the contrary, contemporaneous deformations appear to be lacking in the area of the Dutch sector of the Central Graben (Van Wijhe, 1987). The modelled deformation style resembles these features (Figure 83a). The bulk of Oligocene inversion tectonic is modelled along the south-western part of the Broad Fourteens Basin with a rate of positive vertical displacement up to  $0.6 \cdot 10^{-16} \text{ s}^{-1}$  as well as along the southern flank of the West Netherlands Basin, where vertical strain rate reaches maximum values of about  $0.4 \cdot 10^{-16} \text{ s}^{-1}$ . Moving further to the north, the results display a decrease in crustal shortening within the Central Netherlands Basin whereas almost no vertical deformation appears to affect the Dutch North Sea Graben. Moreover, the modelled stress field (Figure 83b) resemble the observed general N-S to NNW-SSE direction of maximum compression under these areas (de Jager, 2003).

*North Sea Central Graben:* Tectonic evolution of the North Sea Basin and adjacent areas was dominated by accelerated subsidence since Oligocene times till Quaternary (Van Wees & Cloetingh, 1996). The main depocentres were found in the northern part of the North Sea as well as across the mid-Norwegian margin (i.e. Møre and Vøring Basins). Only minor subsidence occurred within the central and southern North Sea (Jordt et al., 1995). The modelled vertical strain rate resembles these features. Subsidence centres are modelled in the north-westernmost area up to a maximum of about  $-0.4 \cdot 10^{-16} \text{ s}^{-1}$ . In contrast, in the central North Sea almost no vertical deformation occurs. Moreover, the modelled stress field displays a NW-SE orientation associated with a strike-slip fault regime, transpression, in agreement with previous results from numerical modelling for the Cenozoic stress patterns in the mid-Norwegian margin and in the northern North Sea (e.g. Pascal & Gabrielsen, 2001; Van Wees & Cloetingh, 1996).

The results of Figure 83a and Figure 83b claim at a causal relationship between the observed change in deformation and the regional tectonic reorganization which occurred during Late Eocene-Oligocene (e.g. Ziegler, 1990). The shifting of tectonic activity along the western sector of the Alpine thrust front together with increasing sea-floor spreading in the North Atlantic domain reflects the westward shifting of the centre of active deformation.

Consequently, the bulk of intraplate stresses is absorbed by the deformation of the domains proximal to the effective tectonic boundaries, thus shielding transmissions of significant amount of compressional intra-plate stresses to more distal areas.

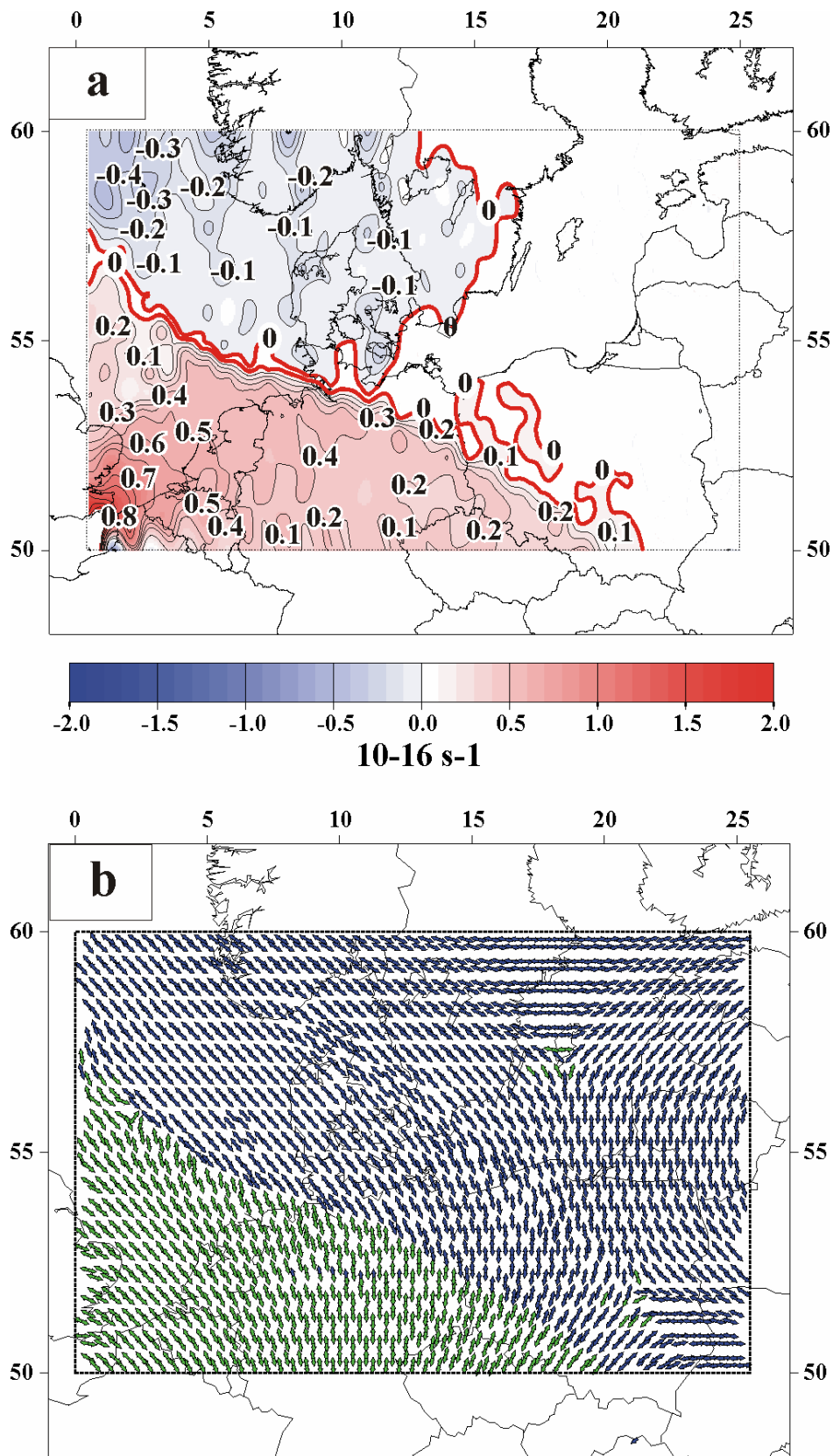


Figure 83. Modelling results for the last phase of compressional deformation. (a) Effective strain rate (=rate of crustal thinning/thickening): positive values-red colours (negative values-blue colours) stand for uplift (subsidence). (b)  $S_{Hmax}$  orientation (arrows) and associated stress regime (colours). Green colours refer to thrust faulting, and blue to strike-slip (transpressive) faulting.

## 2.4 Summary

Part 2 describes the results obtained from numerical models concerning the Post Permian tectonic evolution of the CEBS. The first part of the chapter (cf. Part 2.2) presents an integral study for the deep crustal and shallow mantle structures and their rheologies with regard to the recent stress and strain patterns. The distribution of stresses and strains is investigated through the use of a spherical, finite element, thin sheet model. A preliminary thermo-mechanical study is performed to account for the impact of variations in both compositional and thermal parameters. The feedback between deformation and temperature is investigated by a three dimensional finite-element model generated to solve the steady state heat energy equation plus heat production in three dimension for the entire basin system. To calculate the distribution of stresses with depth, strength profiles are calculated within a rheological model using the obtained geotherms and a set of suitable rheological flow laws. To account for the main deformation mechanisms, the lithosphere is approximated by a finite number of lithological units of uniform structural composition. The main vertical structures are modelled to represent (1) the sedimentary layers, (2) the upper and (3) lower crust, and (4) the lithospheric mantle. Variations in the thickness within these layers are constrained by information from large-scale seismic studies and gravimetric models performed in the study area. For each structural layer the set of possible deformation regimes comprise brittle failure according to Byerlee's law and ductile failure by steady-state power law creep or Dorn's law (for olivine). The consistency of the model results is constrained by direct comparison of modelling results and two independent set of observable data: (1) the present-day regional stress field orientation obtained from the "World Stress Map Project" (Reinecker et al., 2005), and (2) the horizontal deformation pattern as geodetically observed in Europe (Altamini et al., 2002). The observed deformation and stress pattern in the CEBS can be reproduced with reasonable agreement by the models. As already demonstrated by previous studies (Marotta, 2005), lateral rheological contrasts within the lithosphere affect both the magnitude and the direction of the strain rate vectors. Accordingly, continental deformation is localized by thermal, mechanical and compositional heterogeneities within the lithosphere. Strong strain localization develops naturally in response to the presence of structural and thermal contrasts. Consequently, no artificial devices (e.g. deep penetrating faults, shear zones) should be inserted in the model formulation. At the same time, strong lateral contrasts drive the propagation of tectonic deformation and affect the regional stress field. The direction of the principal stress axes is not totally independent from the rheology of the lithosphere. The

presence of different structural domains at crustal and shallow mantle level is responsible for the present-day local variations observed in the direction of the regional stress field.

The second part of the chapter describes an attempt to model the evolution of subsidence centres and areas of uplift through time. In modelling the tectonic evolution of the CEBS two concurring factors are addressed:

- (1) The thermo-mechanical structure of the lithosphere;
- (2) Different imposed stress boundary conditions as derived by large-scale (palaeo)tectonic plate reconstruction.

In order to elucidate the role of pre-existing inherited structures within the lithosphere, the rheological structure of the lithosphere as constrained for the present-day is adopted. At the same time, different sets of suitable boundary conditions are defined based on available plate tectonic studies. The purpose is to understand to which extent variations, even small, in the regional stress regime and/or direction can affect the character of basin development.

The results show the significance of old inherited structures in controlling deformation patterns related to tectonic forces. The different (sub)basins show differential response to the active stress regime which is related to their internal structure with pre-existing internal discontinuities playing a prominent role in controlling deformation patterns. In connection with structural heterogeneities the results demonstrated that slightly different sets of boundary forces are able to determine the regional kinematics even for a complex basin system.